Contributions to late Ediacaran geobiology in South China and southern Namibia

Michael Bruce Meyer

Dissertation submitted to the faculty of the Virginia Polytechnic Institute and State University in partial fulfillment of the requirements for the degree of

Doctor of Philosophy

In

Geosciences

Shuhai Xiao

Michal J. Kowalewski

James D. Schiffbauer

Benjamin Gill

Ken Eriksson

April 29th 2013

Blacksburg, VA

Keywords: Taphonomy, Ediacara, South China, Namibia, Geobiology

Contributions to late Ediacaran geobiology in South China and southern Namibia

Michael Bruce Meyer

ABSTRACT

The Ediacaran, particularly the late Ediacaran-Cambrian (E-Є) boundary (551-541 Ma), has been noted as a major time of biological and biochemical transition, including: the rise of predators, the emergence of skeletons, the radiation of bioturbators, and large fluctuations in oceanic chemical conditions (e.g. anoxia/euxinia/ferruginia) with emerging data suggesting that it is not until the late Ediacaran Period (551-542 Ma) when pervasive oxidation of the deep oceans occurred. In addition, the study of Ediacaran paleobiology involves numerous factors, including but not limited to, restricted amount of outcrops, taphonomic biases, metamorphism, enigmatic phylogenetic affinities, non-actualistic atmospheric and oceanic conditions, and unusual taphonomic windows, making it difficult to assign order to the myriad types of fossils (both body and trace) found during this time . It is with these problems in mind that my dissertation focuses on taphonomic questions in the late Ediacaran. We observe fossil through the taphonomic window and thereby colors all aspects of the study of that organism. By understanding how an organism was preserved we can learn about other factors affecting it, such as their taxonomic affinities, paleoecology, and morphology.

All of these factors were examined through taphonomic investigations and this can be seen in the analytical path through my chapters. In chapter two I examined the preservation of trace fossils in the late Ediacaran. In chapter three I analyzed the taphonomy of an exceptionally preserved Ediacaran fossil to solve its affinity, tubular trace or tubular soft-bodied fossil. In chapter four, understanding the nature of exceptional preservation, I investigated the taphonomy of an Ediacara fossil in coarse grained sediments. In chapter five, I combined the findings of the previous chapters and applied that knowledge to analyze the *in situ* three dimensional morphology of an Ediacara fossil. Each of the projects presented pairs new technologic methodologies (SEM, BSE-Z, EDS, Raman, microCT) with traditional paleontological and petrologic investigations (field work, hand sample, and petrographic thin-section analysis). The result of this union of Old and New are findings that expand our understanding of these earliest multicellular organisms, their modes of life, and their biological affinities.

DEDICATION

I dedicate this work to my family and friends. Without their love and support I could not have accomplished any of this.

ACKNOWLEDGEMENTS

There are too many people to thank for their part in helping me complete this work, both personally and professionally. They are, in no particular order: my parents, Bruce and Susan Meyer, for boundless support and advice, my brothers, Matt and Steve Meyer, for being the best sounding boards, the whole of the Meyer and Lamonte families for always believing in me, the Sliko clan, better in laws I could not have, my friends, from Sundling to Fremd to USF and Virginia Tech, you all inspire me and I look forward to more good times, all of my teachers, Mr. B, Linda Bragg, Peter Konecki, my Masters advisor, Dr. Peter Harries, for showing me how to balance life, my PhD committee for their advice and guidance, my PhD advisor, Shuhai Xiao, who has shown me how to be a better person and scientist, and finally my wonderful wife, whose patience, support, and love has allowed me to achieve my dreams, I love you so much.

ATTRIBUTIONS

Chapter Two is in the final stages of preparation for submission to *Palaeogeography Palaeoclimatology Palaeoecology* as "Meyer, M., Xiao, S., Gill, B.C., Schiffbauer, J.D., Chen, Z., Zhou, C., Yuan, X. Interactions between Ediacaran animals and microbial mats: insights from *Lamonte trevallis*, a new trace fossil from the Dengying Formation of South China". M. Meyer and S. Xiao conceived of the project and collected the material with Z. Chen, C. Zhou, and X. Yuan. M. Meyer collected isotope samples and analyzed them with assistance from B.C. Gill. M. Meyer and J.D. Schiffbauer collected elemental maps and point analyses.

Chapter Three was published as "Meyer, M., Schiffbauer, J.D., Xiao, S., Cai, Y., Hua, H., 2012. Taphonomy of the upper Ediacaran enigmatic ribbon-like fossil Shaanxilithes. *Palaios* 27, 354-372". It is reprinted here with permission from M. Meyer. M. Meyer and S. Xiao conceived of the project and collected the material with Y. Cai and H. Hua. M. Meyer and J.D. Schiffbauer collected elemental maps and point analyses.

Chapter Four is in review at *Journal of Paleontology* as "Meyer, M., Elliott, D.A., Schiffbauer, J.D., Vickers-Rich, P., Xiao, S., Hoffmann, K.H., Hall, M., and Schneider, G., Taphonomy of the Ediacaran fossil Pteridinium simplex preserved three-dimensionally in mass flow deposits in the Nama group of Namibia". It is reprinted here with permission from M. Meyer. M. Meyer, D. Elliott, P. Vickers-Rich, and S. Xiao conceived of the project and collected the material. M. Hall and P. Vickers-Rich provided stratigraphic background. K. H. Hoffman and G. Schneider allowed access to the fossil locality and access to museum specimens. M. Meyer, D. Elliott, and J.D. Schiffbauer made thin section material and collected elemental maps and point analyses.

Chapter five is in the final stages of preparation for submission to *Proceedings of the National Academy of Sciences* as "Meyer, M., Elliott, D.A., Wood, A. D., Polys, N.F., Colbert, M., Maisano, J. A., Hall, M., Hoffmann, K.H., Hall, M., Schneider, G., Vickers-Rich, P., and Xiao, S. Three dimensional microCT analysis of the Ediacara fossil Pteridinium simplex sheds new light on its ecology and phylogenetic affinity". M. Meyer, D. Elliott, P. Vickers-Rich, and S. Xiao conceived of the project and collected the material. M. Hall and P. Vickers-Rich provided stratigraphic background. K. H. Hoffman and G. Schneider allowed access to the fossil locality and access to museum specimens. M. Meyer, D. Elliott, and J.D. Schiffbauer made thin section material and collected elemental maps and point analyses. M. Colbert and J.A. Maisano processed the samples using microCT scans. M. Meyer, A.D. Wood, and N.F. Polys post-processed and segmented the microCT data.

TABLE OF CONTENTS

LIST OF FIGURES

Chapter 2

Chapter 3

LIST OF TABLES

Chapter 2

Chapter 3

Chapter 4

GRANT INFORMATION

Chapter 2

This work was supported by National Science Foundation, Chinese Academy of Sciences, National Natural Science Foundation of China, Chinese Ministry of Science and Technology, Australian Research Council Discovery Grant Program, the Society for Sedimentary Geology (SEPM), and the Virginia Tech Institute for Critical Technology and Applied Science Nanoscale Characterization and Fabrication Laboratory.

Chapter 3

Financial support for this study was provided by National Science Foundation, National Natural Science Foundation of China (40872021, 41030209, 41028002), NASA Exobiology and Evolutionary Biology Program, the Virginia Tech Institute for Critical Technology and Applied Science Nanoscale Characterization and Fabrication Laboratory, and the Paleontology Society.

Chapter 4

Financial support for this study was provided by National Science Foundation, NASA Exobiology and Evolutionary Biology Program, Virginia Tech Institute for Critical Technology and Applied Science Nanoscale Characterization and Fabrication Laboratory, the Paleontological Society, and the Society for Sedimentary Geology (SEPM), UNESCO's International Geosciences Program Projects 493 and 587, the National Geographic Society, and from both the international and national committees of the International Geoscience Programme (IGCP).

Chapter 5

Financial support for this study was provided by the National Science Foundation (EAR-0844235 and EAR-0948842), International Geosciences Program Projects 493 and 587, and National Geographic Society, and both the international and national committees of the International Geoscience Programme (IGCP).

CHAPTER 1

Overview of geobiological investigations into the late Ediacaran of South China and southern Namibia

MIKE MEYER

[1]*Department of Geosciences, Virginia Polytechnic Institute and State University,*

Blacksburg, VA 24061, USA

1.1 Introduction

The Ediacaran, particularly the late Ediacaran-Cambrian (E-Є) boundary (551-541 Ma), has been noted as a major time of biological and biochemical transition, including: the rise of predators (Bengtson and Yue, 1992), the emergence of skeletons (Knoll, 2003), the radiation of bioturbators (Droser et al., 2002), and large fluctuations in oceanic chemical conditions (e.g. anoxia/euxinia/ferruginia)(Canfield et al., 2007; Canfield et al., 2008; Wille et al., 2008) with emerging data suggesting that it is not until the late Ediacaran Period (551-542 Ma) when pervasive oxidation of the deep oceans occurred (Canfield et al., 2007; Canfield et al., 2008; McFadden et al., 2008). In addition, the study of Ediacaran paleobiology involves numerous factors, including but not limited to, restricted amount of outcrops, taphonomic biases, metamorphism, enigmatic phylogenetic affinities, non-actualistic atmospheric and oceanic conditions, and unusual taphonomic windows, making it difficult to assign order to the myriad types of fossils (both body and trace) found during this time (McCall, 2006; Fedonkin et al., 2007a). It is with these problems in mind that my dissertation focuses on taphonomic questions in the late Ediacaran. We observe fossils through the taphonomic window which thereby colors all aspects of the study of that organism. By understanding how an organism was preserved we can learn about other factors affecting it, such as their taxonomic affinities, paleoecology, and morphology. The following chapters are tied together by investigations into the interactions of these three factors; specifically from two well-known late Ediacaran fossil localities, South China and southern Namibia.

1.2 Summary of Research

In Chapter 2 a new ichnogenus and ichnospecies of burrow, *Lamonte trevallis*, is described from Shibantan Member of the late Ediacaran Dengying Formation of South China (Hubei). The burrows are preserved in full relief by carbonate and silica cements as straight to gently curving or looping cylindrical tubes, that branch and may terminate at a node. The burrows may have a ropey appearance, are unlined, lack scratch marks, and are found exclusively within clayey crinkled microlaminae thought to represent microbial mats. Stable $\delta^{18}O_{carb}$ and $\delta^{13}C_{carb}$ isotope data on the calcite cement infill, crinkled microlaminae, and limestone matrix cluster in distinct groups when plotted, indicating slightly different conditions affecting each group. The multi-nodal nature of *Lamonte trevallis* tunnel systems, size, and their placement within microbial mats, suggests that active organisms constructed the tunnels to exploit nutrient and oxygen resources in low-oxygen waters.

In Chapter 3 the enigmatic fossil *Shaanxilithes ningqiangensis* from the late Ediacaran Gaojiashan Member of the Dengying Formation, southern Shaanxi Province, South China is examined through detailed microstructural and microchemical investigations. This taxon has also been reported from Ediacaran successions in North China and possibly in southeastern Siberia, making it a potential index fossil for inter-regional biostratigraphic correlation of upper Ediacaran successions. At Gaojiashan, *Shaanxilithes ningqiangensis* is often preserved along bedding planes of phosphate-rich silty and calcareous shale, with no evidence of vertical intrusion into adjacent beds and containing little to no carbonaceous material. Together with other taphonomic features, such as abruptly bent ribbons, overlapping but not cross-cutting ribbons, and co-occurring discoidal structures

interpreted as disarticulated sections of the original organism, the new data suggest that *Shaanxilithes ningqiangensis* is a body fossil.

In Chapter 4 the nature of three dimensional preservation in coarse grained siliciclastic sediments are investigated. For many Ediacara fossils, the "death mask" model has been invoked as the primary taphonomic pathway. The key to this preservational regime is the replication or sealing of sediments around the degrading organisms by microbially-induced precipitation of authigenic pyrite, leading toward fossil preservation *along* bedding planes. Nama-style preservation, on the other hand, captures Ediacaran organisms as molds and three-dimensional casts *within* coarse-grained mass flow beds, and has been previously regarded as showing little or no evidence of a microbial preservational influence. To further understand these two seemingly distinct taphonomic pathways, we set out to investigate the three-dimensionally preserved Ediacara fossil *Pteridinium simplex* from mass flow deposits of the upper Kliphoek Member (recently renamed as the Aar Member, Hall et al., submitted), Kuibis Subgroup, southern Namibia. Our analysis, using a combination of petrographic and micro-analytical methods, shows that *Pteridinium simplex* vanes are replicated, with minor pyrite, but are most often represented by open voids that can be filled with secondary carbonate material. While many of the same processes as in death mask formation led to *P. simplex*'s three-dimensional preservation; Nama-style preservation continues to stand apart as a taphonomic mode in the Ediacaran.

In Chapter 5 the pattern of Ediacara fossils often exhibiting enigmatic morphologies that defy easy characterization and ready categorization with extant taxa is investigated using *Pteridinium simplex* from the late Ediacaran Aar Member in southern Namibia. While it

is a widely distributed taxon, *P. simplex* in Namibia is typically preserved as three-dimensional casts and molds in coarse grained quartzites, making detailed morphological characterization difficult. In addition, *P. simplex* is often transported, distorted, and embedded in gutter fills or channel deposits, further obscuring its morphologies. By utilizing microfocus X-ray computed tomography (microCT) techniques; we were able to find and trace individual specimens and the vanes of those *P. simplex* specimens and restore the three-dimensional morphology of this enigmatic fossil. While *P. simplex* specimens were found to be very flexible, there is evidence of tearing, the first found in *P. simplex*, in at least one specimen. X-ray microCT offers a new opportunity to investigate the in situ morphologies of Ediacara fossils.

1.3 Geologic Setting

1.3.1 South China

The Ediacaran strata in south China were deposited on the Yangtze platform, which is the northwestern half of the total south China block. The south China block is composed of the Yangtze and Cathaysia cratons which were amalgamated during the formation of Rodinia ~1000-900 Ma. The Yangtze platform formed at ~825 ma (Li et al., 2008; Jiang et al., 2011) during rifting associated with the breakup of Rodinia which is recorded in the fluvial Liantuo Formation (platform) and the Baxi Group (basin). There is evidence for Snow Ball Earth (SBE) events during the Cryogenian on the Yangtze platform with the Sturtian represented by the diamictite of the Gucheng and related formations (these are not seen on the platform, possibly due to erosion from later glacial episodes) and the Marinoan represented by the Nantuo diamictite (Wang and Li, 2003; Li et al., 2008; Jiang

et al., 2011). The lack of volcanics in the late Cryogenian and Ediacaran strata of south China suggests that the transition from rifting to drifting likely occurred in late Cryogenian time.

The Ediacaran (635-542 Ma) strata of south China are composed of two formations, the Doushantuo and the Dengying. These formations display varying thicknesses, with platform sections being thicker (≤1000 m) than the basinal sections (~250 m) (Jiang et al., 2011). The Doushantuo Formation is divided into four members based on the well-known Jiulongwan section, which is just a few km away from the Wuhe section studied here. Member 1 is a ~5-m-thick cap carbonate followed by the alternating organic rich shale and carbonates with abundant pea-sized chert nodules of Member 2. Member 3 is composed of mainly carbonates interbedded with chert layers and minor shale laminae. Member 4 (like Member 1) is used as regional marker for the Doushantuo and is a ~10-m-thick black, organic-rich shale interval. The Doushantuo is bracketed by two U-Pb dates, an age of 635.2±0.6 Ma from cap carbonate (Condon et al., 2005) and another of 551.1±0.7 Ma from an ash layer near the Doushantuo/Dengying boundary (Condon et al., 2005). The Dengying Formation extends to the base of the Cambrian, with dates of 539.4±2.9 Ma (Compston et al., 2008) and 536.3±5.5 (Chen, 2005) from ash beds in the earliest Cambrian units.

The two locations examined in my dissertation, are Wuhe and Gaojiashan. The Wuhe locality is from a quarry near the town of Wuhe (in the Yangtze gorges region) in Hubei province and the other along the road to the mountain top town of Gaojiashan in Shaanxi province. The Dengying at the Wuhe section is composed of three units (in chronological order): the 25 m thick Hamajing peritidal dolostone, 115 m thick Shibantan

bituminous limestone, and ~65 m thick Baimatuo peritidal dolostone (Zhou and Xiao, 2007; Jiang et al., 2011). The section in Shaanxi province near the town of Gaojiashan has poor age constraints, but it also consists of three members (in chronological order): the ~150 m thick peritidal Zaobaiyunyan, ~ 55 m thick Gaojiashan calcareous siltstone, and 300 m thick Beiwan peritidal dolostone in the Gaojiashan area (Cai and Hua, 2007; Cai et al., 2010). The three members of the Dengying Formation at Gaojiashan are thought to be correlated to the tripartite system seen in the Yangtze Gorges area, constraining the age of the Dengying Formation at Gaojiashan to be 551-542 Ma.

1.3.2 Southern Namibia

The Kuibis Subgroup was deposited in a foreland basin on the northern edge of the Kalahari Craton (Fig. 1.1) (Germs, 1973). Available radiometric dates constrain the Kuibis Subgroup to be older than 548.8±1 Ma (revised as 547.32 ± 0.65 Ma) (Grotzinger et al., 1995; Schmitz, 2012b). This foreland basin includes two subbasins, the northern Zaris and the southern Witputs subbasins, separated by the Osis arch (Gresse and Germs, 1993; Saylor et al., 1995). The Witputs subbasin the Kuibis Subgroup contains two formations: the Dabis and Zaris Formations. Here, the Kuibis Subgroup is characterized by feldspathic sandstone-orthoquartzite-limestone cycles, with limestones becoming more common up-section.

Our specimens come from the Kliphoek Member of the Dabis Formation. The lower Kliphoek Member is the last major sandstone unit of the afore-mentioned sandstone-limestone cycles before the beginning of the Schwarzrand Subgroup (Gresse and Germs, 1993; Saylor et al., 1995). The lower Kliphoek Member (or the Kliphoek

sandstone; Fig. 1.1) consists of fine to coarse grained orthoquartzite, with coarser material found within mass flow deposits (Elliott et al., 2011), whereas the upper Kliphoek (Aar) Member (Hall et al., *submitted*) consists mainly of interbedded sandstones (1–2 m thick) and shales with a few limestone beds. The base of many Kliphoek Member sandstone beds are often characterized with scouring and tool marks, representing channel and gutter fills in shallow-water high-energy environments (Saylor et al., 1995; Hall et al., *submitted*). The Kliphoek Member is directly overlain by bedded limestones of the Mooifontein Member, indicating a major marine transgression (Gresse and Germs, 1993).

The upper Kliphoek Member, which was likely deposited in an extensive, sandy, braided fluvial to shallow marine system (Elliott et al., 2011; Hall et al., *submitted*), partly reworked into vast inter-tidal sand flats along a low gradient coastal plain. The upper Kliphoek (Aar) Member consists mainly of cross-bedded sandstones (1–2 m thick) interbedded with shale units. Shale interbeds found between the sandstones are interpreted as intertidal to shallow subtidal muds deposited during regional transgression. Individual sandstone beds range up to 35 cm in thickness, commonly showing thin laminations, occasionally with symmetric ripples, and sometimes containing pelloidal structures resembling rip-up clasts (Elliott et al., 2011). Sandstone beds in the upper Kliphoek Member typically have sharp bases and tops, and sometimes exhibit very low angle scouring of the underlying shale (Elliott et al., 2011; Hall et al., *submitted*). *Pteridinium simplex* fossils are found in these sandstone beds, particularly in the Aarhauser sandstone in the lower Aar Member (Hall et al., *submitted*).

1.4 References

BENGTSON, S., and YUE, Z., 1992, Predatorial borings in late Precambrian mineralized exoskeletons: Science, v. 257, p. 367-369.

CAI, Y., and HUA, H., 2007, Pyritization in the Gaojiashan Biota: Chinese Science Bulletin, v. 52, p. 645-650.

CAI, Y., HUA, H., XIAO, S., SCHIFFBAUER, J.D., and LI, P., 2010, Biostratinomy of the late Ediacaran pyritized Gaojiashan Lagerstätte from southern Shaanxi, south China: Importance of event deposits: Palaios, v. 25, p. 487-506.

CANFIELD, D.E., POULTON, S.W., KNOLL, A.H., NARBONNE, G.M., ROSS, G., GOLDBERG, T., and STRAUSS, H., 2008, Ferruginous conditions dominated later Neoproterozoic deep-water chemistry: Science, v. 321, p. 949-952.

CANFIELD, D.E., POULTON, S.W., and NARBONNE, G.M., 2007, Late Neoproterozoic deep-ocean oxygenation and the rise of animal life: Science, v. 315, p. 92-95.

CHEN, J., 2005, The Dawn of Animal World: Jiangsu Science and Technology Press, Nanjing, 366 p.

COMPSTON, W., ZHANG, Z., and COOPER, J.A., 2008, Futher SHRIMP Geochronology on the early Cambrian of South China: American Journal of Science, v. 208, p. 399–420.

CONDON, D., ZHU, M., BOWRING, S., WANG, W., YANG, A., and JIN, Y., 2005, U-Pb ages from the Neoproterozoic Doushantuo Formation, China: Science, v. 308, p. 95-98.

DROSER, M.L., JENSEN, S., and GEHLING, J.G., 2002, Trace fossils and substrates of the terminal Proterozoic-Cambrian transition: Implications for the record of early bilaterians and sediment mixing: Proceedings of the National Academy of Sciences, USA, v. 99, p. 12572-12576.

ELLIOTT, D.A., VICKERS-RICH, P., TRUSLER, P., and HALL, M., 2011, New evidence on the taphonomic context of the Ediacaran *Pteridinium*: Acta Palaeontologica Polonica, v. 56, p. 641-650.

FEDONKIN, M.A., GEHLING, J.G., GREY, K., NARBONNE, G.M., and VICKERS-RICH, P., 2007, The Rise of Animals: Evolution and Diversification of the Kingdom Animalia: Johns Hopkins University Press, Baltimore, 326 p.

GERMS, G.J.B., 1973, The Nama Group in South-West Africa and its relationship to the pan-African geosyncline: The Journal of Geology, v. 82, p. 301-317.

GRESSE, P.G., and GERMS, G.J.B., 1993, The Nama foreland basin: sedimentation, major unconformity bounded sequences and multisided active margin advance: Precambrian Research, v. 63, p. 247-272.

GROTZINGER, J.P., BOWRING, S.A., SAYLOR, B.Z., and KAUFMAN, A.J., 1995, Biostratigraphic and geochronologic constraints on early animal evolution: Science, v. 270, p. 598-604.

HALL, M., KAUFMAN, A.J., VICKERS-RICH, P., GUY, N., IVANSTOV, A.Y., TRUSLER, P., LINNEMANN, U., HOFMANN, M., ELLIOTT, D.A., CUI, H., FEDONKIN, M.A., HOFFMAN, K., WILSON, S.A., SCHNEIDER, G., and SMITH, J., ***submitted***, Changing environments and their impact on metazoan evolution and preservation during the terminal Proterozoic in african Gondwana: Precambrian Research, v. xxx, p. xxx.

JIANG, G., SHI, X., ZHANG, S., WANG, Y., and XIAO, S., 2011, Stratigraphy and paleogeography of the Ediacaran Doushantuo Formation (ca. 635–551 Ma) in South China: Gondwana Research, v. 19, p. 831-849.

KNOLL, A.H., 2003, Biomineralization and evolutionary history: Reviews in Mineralogy and Geochemistry, v. 54, p. 329-356.

LI, Z.X., BOGDANOVA, S.V., COLLINS, A.S., DAVIDSON, A., WAELE, B.D., ERNST, R.E., FITZSIMONS, I.C.W., FUCK, R.A., GLADKOCHUB, D.P., JACOBS, J., KARLSTROM, K.E., LU, S., NATAPOV, L.M., PEASE, V., PISAREVSKY, S.A., THRANE, K., and VERNIKOVSKY, V., 2008, Assembly, configuration, and break-up history of Rodinia: A synthesis: Precambrian Research, v. 160, p. 179–210.

MCCALL, G.J.H., 2006, The Vendian (Ediacaran) in the geological record: Enigmas in geology's prelude to the Cambrian explosion: Earth Science Reviews, v. 77, p. 1-230.

MCFADDEN, K.A., HUANG, J., CHU, X., JIANG, G., KAUFMAN, A.J., ZHOU, C., YUAN, X., and XIAO, S., 2008, Pulsed oxygenation and biological evolution in the Ediacaran Doushantuo Formation: Proceedings of the National Academy of Sciences, USA, v. 105, p. 3197–3202.

SAYLOR, B.Z., KAUFMAN, A.J., GROTZINGER, J.P., and URBAN, F., 1995, Sequence stratigraphy and sedimentology of the Neoproterozoic Kuibis and Schwarzrand Subgroups (Nama Group), southwestern Namibia: Precambrian Research, v. 73, p. 153-171.

SCHMITZ, M.D., 2012, Appendix 2—Radiometric ages used in GTS2012, *in* Gradstein, F., Ogg, J., Schmitz, M.D., and Ogg, G., eds., The Geologic Time Scale 2012: Elsevier, Boston, p. 1045–1082.

WANG, J., and LI, Z.-X., 2003, History of Neoproterozoic rift basins in South China: Implications for Rodinia break-up: Precambrian Research, v. 122, p. 141-158.

WILLE, M., NÄGLER, T.F., LEHMANN, B., SCHRÖDER, S., and KRAMERS, J.D., 2008, Hydrogen sulphide release to surface waters at the Precambrian/Cambrian boundary: Nature, v. 453, p. 767-769.

ZHOU, C., and XIAO, S., 2007, Ediacaran $d^{13}C$ chemostratigraphy of South China: Chemical Geology, v. 237, p. 89-108.

CHAPTER 2

Interactions between Ediacaran animals and microbial mats: insights from *Lamonte trevallis*, a new trace fossil from the Dengying Formation of South China

MIKE MEYER[1], SHUHAI XIAO[1], BENJAMIN C. GILL[1], JAMES D. SCHIFFBAUER[2], ZHE CHEN[3], CHUANMING ZHOU[3], XUNLAI YUAN[3]

[1]*Department of Geosciences, Virginia Polytechnic Institute and State University, Blacksburg, VA 24061, USA*

[2]*Department of Geosciences, University of Missouri, Columbia, MO, 65211, USA*

[3]*Nanjing Institute of Geology and Paleontology, Chinese Academy of Sciences, Nanjing 210008, China*

1.1 Abstract

A new ichnogenus and ichnospecies, *Lamonte trevallis*, is described from the Shibantan Member limestone of the late Ediacaran Dengying Formation in the Yangtze Gorges area of South China. It is characterized by horizontal burrows occurring exclusively within clayey and silty, crinkled, and microlaminated layers that are interpreted as the remnants of amalgamated microbial mats; no burrows have been found in intraclastic layers adjacent to the microlaminated layers. The burrows are preserved in full relief and filled with carbonate intraclasts and micrites, as well as calcite and silica cements. The burrow infill has $\delta^{18}O_{carb}$ and $\delta^{13}C_{carb}$ values distinct from, but intermediate between, microlaminated and intraclastic layers, consistent with petrographic observation that burrow infill consists of a mixture of carbonate cements, intraclasts, and micrites. Bioturbation intensity (22–41%)—measured as percentage of bedding plane area covered by *L. trevallis* traces—is comparable to similar measurements in pre-trilobite Cambrian carbonates. We suggest that there is a taphonomic and ecological significance in the exclusive occurrence of *L. trevallis* within microbial mats. Microbial mats provided firm substrates and localized geochemical conditions that contributed to the structural integrity of the burrow and diagenetic cementation of burrow infill, thus facilitating burrow preservation. The close association of these burrows with microbial mats suggests that the burrowers were actively mining microbial mats to exploit oxygen or nutrient resources. The trace makers of *L. trevallis* burrow systems were better able to utilize the resources around them than many other Ediacaran trace makers, and left ichnological evidence of a flourishing benthic ecology in late Ediacaran oceans at the dawn of the agronomic revolution.

2.2 Introduction

The establishment of burrowing and bioturbating behaviors is a key event in the evolution of bilaterian animals, with a significant impact on paleoecological and geobiological dynamics at the Ediacaran-Cambrian transition. Ediacaran burrows are traditionally known for their small size, simple morphology, shallow penetration depth, and relative scarcity when compared to their Phanerozoic counterparts (Droser et al., 1999; Jensen et al., 2005; Droser et al., 2006; Jensen et al., 2006; Seilacher, 2007). There are several reasons why Ediacaran burrows are limited in complexity, diversity, and abundance. Dissolved oxygen levels were relatively low and uneven in Ediacaran oceans (Kennedy et al., 2005; Fike et al., 2006; McFadden et al., 2008; Shen et al., 2008). The ubiquitous microbial mats of the time also maintained a sharp redox gradient across the sediment-water interface so that deeper sediments were poorly oxygenated and generally hostile to burrowers (Gehling, 1999; Fedonkin et al., 2007a). Predation pressures were not prevalent, thereby allowing animals to forage along the surface of microbial mats or sediments (Fedonkin and Waggoner, 1997; Ivanstov and Malakhovskaya, 2002; Dzik, 2005; Fedonkin et al., 2007b). It is also possible that Ediacaran animals may have been physically incapable of making large and complex burrows due to the lack of a strong musculature system (Miller, 2007; Seilacher, 2007). Despite their limited complexity and diversity, however, Ediacaran trace fossils do offer the only paleontological window onto the rising importance of bioturbation at a key transition in the history of life.

One of the important innovations in the Ediacaran evolution of animal bioturbation was for animals to explore and break through the ubiquitous microbial mats, leading to a deeper sediment penetration and greater geobiological impact (Canfield and

Farquhar, 2009). Numerous paleoichnological studies have shown that Ediacaran-Cambrian animals had begun to explore microbial mats for oxygen and nutrients (Seilacher, 1999; Seilacher et al., 2005; Gingras et al., 2011), and eventually put an end to the microbially dominated world (Hagadorn and Bottjer, 1999; Bottjer et al., 2000; Droser et al., 2002). Going hand in hand with their greater roles in shaping the microbial world, bilaterian animals also left increasingly complex burrow systems (Jensen et al., 2000; Jensen and Runnegar, 2005; Seilacher et al., 2005), indicating a more dynamic benthic ecology toward the late Ediacaran Period.

In the last decade the late Ediacaran Dengying Formation (~551–541 Ma) in the Yangtze Gorges area of South China has been an important source for Ediacaran trace fossils, including simple taxa such as *Helminthoidichnites*, *Palaeophycus*, *Planolites*, and *Torrowangea* (Zhao et al., 1988; Ding et al., 1992; Jensen et al., 2006; Weber et al., 2007), as well as more complex forms that represent under-mat feeding, epibenthic locomotion, and temporary dwelling of bilaterian animals (Chen et al., 2013b). In particular, the Shibantan Member limestone of the middle Dengying Formation holds great potential to illuminate ecological interactions between late Ediacaran animals and microbial mats, because of the abundance and exceptional preservation of both trace fossils and microlaminae that can be interpreted as microbial mats. Here, we describe a type of Ediacaran trace fossil, *Lamonte trevallis*, which can potentially broaden our understanding of trace maker behavior during this time. However, to realize this potential, it is necessary to have a holistic analysis of the taphonomy of the Shibantan fossils, their occurrence, and their relationship with the microbial mats. Building upon our previous report of Shibantan trace fossils (Chen et al., 2013b), this study synthesizes

petrographic and geochemical data in order to better understand the preservation and paleoecology of Shibantan burrows.

2.3 Geological setting

The geological and stratigraphic background of the Dengying Formation in the Yangtze Gorges area was described in Chen et al. (2013). Briefly, the Dengying Formation overlies the early-middle Ediacaran Doushantuo Formation and underlies the Yanjiahe Formation which contains the Ediacaran-Cambrian boundary (Dong et al., 2009; Jiang et al., 2012). It was deposited in a shallow water carbonate platform, and its age is constrained to be 551–541 Ma based on available radiometric dates (Condon et al., 2005; Jiang et al., 2009; Zhu et al., 2009). The Dengying Formation is divided into three units, in ascending age order: the Hamajing, Shibantan, and Baimatuo members (Fig. 2.1). The Hamajing Member consists of peritidal dolostone, with widespread tepee structures and karstification features such as dissolution vugs ranging from a few millimeters to a few meters in size (Fig. 2.2A–B). The Shibantan Member is composed of dark gray, thin-bedded, bituminous limestone deposited in a subtidal environment (Fig. 2.2C). Crinkled microlaminae (Fig. 2.2D) consisting of organic-rich, calcareous clays and silts are very common, and are often intercalated with thin layers of intraclastic (mostly pelloidal, oolitic, and oncolitic) packstone and grainstone (Fig. 2.2D). These crinkled microlaminae are interpreted as microbial mats that trapped silts/clays and were cemented by diagenetic calcite (Chen et al., 2013). Although the Shibantan Member is mostly characterized by parallel laminae, cross stratification and rip-up clasts are present (Figs. 2.2E–F), indicating deposition above storm wave-base. The Baimatuo Member is

composed of light gray massive peritidal dolostone, characterized with abundant dissolution vugs and breccia (Fig. 2.2G).

The Shibantan Member is the most fossiliferous member of the Dengying Formation (Zhao et al., 1988; Weber et al., 2007), with not only trace fossils, but also macroscopic Ediacara-like fossils such as *Paracharnia* (Sun, 1986) and *Yangtziramulus* (Xiao et al., 2005; Shen et al., 2009). The Gaojiashan Formation in southern Shaanxi Provence, which is correlative of the Shibantan Member, contains tubular fossils such as *Cloudina*, *Conotubus*, *Gaojiashania*, *Shaanxilithes*, and *Sinotubulites* (Hua et al., 2003; Hua et al., 2005; Chen et al., 2008; Cai et al., 2010; Cai et al., 2011; 2012; Meyer et al., 2012). Of these, *Sinotubulites* has also been found in the Baimatuo Member in the Yangtze Gorges area (Chen and Wang, 1977; Chen, 1999).

The trace fossils described in this paper came from a facies in the Shibantan Member that is characterized by parallel-bedded intraclastic limestone intercalated with clayey/silty, crinkled, microlaminated layers. Freshly excavated bedding surfaces are commonly rusty in color, resulting from oxidative weathering of pyrite. The intraclastic layers are 0.5–20 mm thick, consisting of fine-grained (~50–100 μm) peloidal and oolitic packstone and grainstone (Fig. 2.2D), though the intraclastic fabric may be obscured by recrystallization. The microlaminated layers are 0.1–2 mm thick, often with amalgamated microlaminae that are crinkled and anastomosed (Fig. 2.2D). Clays and silts are enriched in the microlaminae layers than in the intraclastic layers. The trace fossils occur exclusively in the microlaminated layers.

2.4 Methods and Materials

The trace fossils reported in this paper were collected from the Shibantan Member at a quarry near Wuhe in the Yangtze Gorges area (30º 46'47.74" N, 111º02'28.89" E) over multiple field seasons. Abundant trace fossils were observed on outcrops where stratigraphic orientation can be identified unambiguously. Numerous loose slabs and blocks containing trace fossils were collected (Figs. 2.3–4) from active quarries where thin-bedded limestone of the Shibantan Member is quarried for construction, roofing, and pavement material. The stratigraphic orientation of the loose slabs can sometimes (although not always) be inferred using sedimentary structures such as low-angle cross stratification and truncation of microlaminae. Selected fossils were cut perpendicular to bedding surfaces to make thin sections for petrographic observations in order to characterize the occurrence of fossils and their relationship with microbial mats (Figs. 2.5–6). Inferred stratigraphic orientations are marked in fossil figures, with ⊤ representing top bedding surface view, ⊥ representing bottom bedding surface view, and ↑ stratigraphic up direction when thin sections were made perpendicular to bedding surfaces.

Polished thin sections and slabs were examined using electron microscopy (Figs. 2.7–8), conducted on an FEI Quanta 600 field emission environmental scanning electron microscope (ESEM) in high vacuum mode using secondary electron (SE) or backscattered electron (BSE) detectors. Energy dispersive X-ray spectroscopic (EDS) point spectra and elemental maps were generated using an integrated Bruker AXS QUANTAX 400 with a high-speed silicon drift detector. Identical operating conditions were maintained for all EDS analyses: 20 keV accelerating voltage, 5.0 spot size (a

unitless measure of beam current and probe diameter), 11.5–12 mm working distance, and X-ray signal count-rates of 25–35 kcps. All elemental maps were acquired for 600 seconds live-time, and individual point spectra were collected for 100 seconds live-time. Elemental peaks from point spectra were identified and quantified (with zaf and Au-Pd coating corrections applied) using the Bruker Esprit 1.9.2 software. Initial X-ray point spectra were collected from the burrow infill, intraclastic layers, and clayey/silty microlaminated layers (Table 2.1–2). Elemental maps were subsequently generated (Figs. 2.7–8) for all elements found at >1% (normalized weight percentage; nwp) in point analysis.

Freshly exposed burrow infill, intraclastic layers, and microlaminated layers were microdrilled for carbon and oxygen isotope analysis (Fig. 2.9), using a 1 mm bit on a bench press drill. Veins and vugs were avoided when powders were microdrilled. The carbonate powders were then allowed to react with 100% phosphoric acid at 70 °C in a MultiFlow-Geo headspace sampler device connected to an Isoprime 100 continuous flow isotope ratio mass spectrometer. Carbon and oxygen isotope compositions are reported in standard delta notation as per mil (‰) deviations from Vienna Pee Dee Belemnite (VPDB). Reproducibility from repeated analysis of international standards IAEA CO-1, IAEA CO-9, and NBS 18 was better than 0.10‰ for $\delta^{13}C_{carb}$ and 0.22‰ for $\delta^{18}O_{carb}$ (Table 3). Trace fossil density on bedding surfaces (horizontal bioturbation intensities) was measured using ImageJ (Schneider et al., 2012). Burrows on slabs were traced digitally, using Adobe Illustrator (Adobe, 2010), into simplified illustrations (Fig. 2.3) which were then imported to ImageJ to measure bedding plane bioturbation intensity.

Vertical bioturbation intensities were measured in a similar way using cross-sections perpendicular to bedding planes.

2.5 Systematic Ichnology

The Shibantan Member has been an important source for Ediacaran trace fossils, but until recently these traces have been represented by simple forms. The most common forms are *Palaeophycus/Planolites*-type traces (Weber et al., 2007). These traces are horizontal, generally 5–8 mm in width, and sometimes extremely flat. These are thought to be shallow feeding burrows of early metazoans (Weber et al., 2007). *Torrowangea* traces are gently curved traces with a width of ~1 mm and irregularly spaced transverse constrictions (Weber et al., 2007). *Helminthoidichnites*–type trace fossils are also very common in the Shibantan Member. They have a large size range, 2–7 mm in width and reaching several decimeters in length. *Helminthoidichnites* traces are straight to sinusoidal trails, absent of any ornamentation, and can be preserved as epi- or hyporelief. *Helminthoidichnites* in the Neoproterozoic is thought to be broadly comparable to *Helminthopsis* and *Gordia*, in that they all represent foraging behavior or undermat mining activities (Jensen, 2003).

Recently an assemblage of trace fossils has been discovered in the Shibantan Member, in preferred association with microbial mats probably to exploit nutrient and oxygen resources (Chen et al., 2013b). This assemblage includes three types of trace fossils: surface trackways, vertical traces, and horizontal tunnels. These three types of traces are interpreted to have been made by the same bilaterian animal, representing locomotion, resting, and undermat mining behaviors, respectively. The horizontal tunnels are the most abundant among the three types. Below we provide a systematic description

of these horizontal tunnels with additional material and analysis. While we realize that the three types of traces described in Chen et al. (2013) could have been made by the same animal, we follow the common ichnotaxonomical practice to use only morphological criteria of the trace fossils to distinguish ichnotaxa (Bertling, 2007). In other words, different traces made by the same animals can be given different ichnotaxonomical names, as long as they have distinct morphologies, such as in the case of *Cruziana* and *Rusophycus* (Miller, 2007; Seilacher, 2007). These trace fossils and associated thin sections are deposited in the Virginia Polytechnic and State University Geoscience Museum (VPIGM).

2.5.1 Ichnogenus Lamonte *Description*

Ichnogenus Lamonte *igen. nov.*

Type and only ichnospecies. Lamonte trevallis igen. and isp. nov.

Diagnosis. Millimeter-sized horizontal lined burrows composed of straight to gently curved elements with cement/intraclast infill connected to vertical traces and found exclusively within crinkled and microlaminated layers.

Etymology. Ichnogenus name derived from Italian *la monte* (mountain) with reference to the mountainous region near the fossil locality.

2.5.2 Ichnogenus Lamonte trevallis *Description*

Lamonte trevallis *igen. and isp. nov.*

Figures 2.3–8

2013 Unnamed horizontal animal trace fossils (tunnels); Chen et al., figs. 2C–I, 3, 6C–E

Diagnosis. As for ichnogenus.

*Etymology***.** Ichnospecies epithet derived from Latin *tres* (three) and *vallis* (valley or gorge) with reference to the Three Gorges near the fossil locality.

Material. Five slabs (VPIGM-4642–4672) and numerous fragmentary specimens from the upper part of the Shibantan Member of the Dengying Formation collected in a quarry just west of Wuhe, Hubei Provence, South China (30º 46'47.74"N, 111º02'28.89"E).

Holotype. The arrowed specimen in Fig. 2.4E (VPIGM-4643) is designated as the holotype.

Description. Horizontal, straight to gently curved burrows, 3–8 mm in width, 1.5–4 mm in depth, up to 30 cm long, and elliptical or bilobed in transverse cross-section. Individual burrows maintain a constant width along its length, although it may taper at both ends when the burrow moves out of the plane of preservation. Burrows have a smooth or rough surface, and some seem to have paired knobs (Chen et al., 2013b). Previously described material has a prominent central longitudinal groove (Chen et al., 2013b), which is not present in every specimen and could have formed during collapse of the tunnel (see fig. 7 in Chen et al., 2013).

Burrows commonly overlap each other (Figs. 6C, 8) and rarely cross-cut. They may pass through or terminate at plug-shaped nodes that have flat tops and bottoms, and these plugs are the only vertical component of the burrow system (Figs. 2.6D–E). These plug-shaped nodes are similar to the "vertical traces" of Chen et al., 2013, up to 6 mm wide and 6 mm deep and laterally connected with horizontal burrows. Occasionally, multiple burrows appear to radiate from a node (Fig. 2.4A), but this is an artifact of

compaction, as thin sections cut perpendicular to bedding plane show that the burrows are stacked upon each other creating a node-like structure (Figs. 2.6C, 8).

Burrows are preserved as full relief tunnels, with the interior cast by micrite (Figs. 2.4D, 5A, 6B, F, 8) or filled with intraclasts (Fig. 2.6D–H), and sometimes lined with a thin organic layer (Fig. 2.5G, H). Regardless, the infill is cemented by diagenetic calcite and silica. Typically, silica cement is present in the center of the burrow, suggesting that it represents a later stage cementation than calcite cement. Some burrows have bitumen within their centers (arrows in Figs. 2.5A, G, 6B). Such bitumen probably derived from oil migration that filled the residual voids following calcite and silica cementation. However, while the bitumen is optically visible, due to the abundance of carbonate material within the intraclastic layers, the infill cement, and the microlaminated layers, the bitumen is not easily observed by EDS (Table. 2.1).

Burrows occur exclusively in clayey and silty, crinkled, and microlaminated layers that are interpreted as amalgamated microbial mats (Chen et al., 2013). In all cases, burrows either truncate or split microlaminae (Figs. 2.5F, G, I, 6A, G), and microlaminae above and below warp around the burrows, indicating that the burrow casts are more resistant to compaction than microlaminated and intraclastic layers. Thus, the burrows did not collapse immediately after the passage of the trace maker, and they must have had certain degree of structure integrity to allow diagenetic cementation of infilling sediment.

Discussion. Lamonte trevallis shares many characteristics of *Planolites* and *Palaeophycus* and traces ascribed to those ichnogenera that have been previously reported form the Shibantan Member (Pemberton and Frey, 1982; Weber et al., 2007) while remaining distinct from either trace fossil. *L. trevallis* is similar to *Planolites* in that

they are both filled with material that clearly differs from the surrounding host rock (Pemberton and Frey, 1982). However, *Planolites* are thought to be temporary structures, whereas *L. trevallis*, like *Palaeophycus*, is a stable structure that did not collapse soon after formation. That there are some remnants of linings in some *L. trevallis* burrows (Fig. 2.5I) suggest a closer affinity to *Palaeophycus* than the unlined burrows of *Planolites*. Also, the few intraclasts found in the cement infill of *L. trevallis* burrows suggests passive sediment filling unlike *Planolites*, but more similar to *Palaeophycus*. Unlike either *Planolites* or *Palaeophycus*, *L. trevallis* burrows often have regular ornamentation (paired knobs and longitudinal grooves; Figs. 2.5A, 6A) and terminate in plug-like structures (Figs. 2.6D–E). The combination of shared *Planolites/Palaeophycus* traits, its own distinct features, and its placement only in microbial mats, splitting or truncating them, are indicators that *L. trevallis* is a unique trace fossil and represents an advance in trace fossil behaviors in the late Ediacaran.

2.6 Analytical Results

The bedding plane bioturbation intensities on the five analyzed specimens are 22–41% (average 32%). In cross-section, the percentage of bioturbated area is ~5%; the lower percentage relative to bedding surface analysis is due to the fact that the burrows are exclusively restricted to the microlaminated layers and thus many layers are not bioturbated. The degree of bioturbation, as measured both on the bedding surfaces and in cross-sections perpendicular to bedding surfaces, is comparable to pre-trilobite Cambrian sediments (Droser and Bottjer, 1988; Droser et al., 1999; Skinner, 2005; Marenco et al., 2008; Marenco and Bottjer, 2011).

EDS spectral data of burrow fills, microlaminated layers, and intraclastic layers are presented in Table 2.1 and 2.2. As expected of limestone sediments, Ca, O, and C are the major elements. Minor constituents, <1% in total nwp, include Al, K, Fe, Mg, P, and S. Microlaminated layers exhibit higher levels of Si, Al, Fe, and K than intraclastic layers, consistent with the presence of silts and clays in the microlaminated layers. The burrow infill shows higher levels of Si than both the intraclastic and microlaminated layers, likely due to the presence of silica cements in the burrows. The elemental distribution patterns are confirmed by elemental maps (Figs. 2.7–8).

Stable isotope data from burrow fills, microlaminated layers, and intraclastic layers are presented in Fig. 2.9 and Table 2.3. Overall, intraclastic layers have the highest $\delta^{13}C_{carb}$ and $\delta^{18}O_{carb}$ values (average at 3.9‰ and –3.8‰, respectively), microlaminated layers have the lowest values (average at 2.0‰ and –6.0‰, respectively), and burrow infill falls in between. The combined data array shows a positive correlate between $\delta^{13}C_{carb}$ and $\delta^{18}O_{carb}$ ($R^2 = 0.8$), suggesting a two-component mixing between a diagenetic cement end-member (with lower $\delta^{13}C_{carb}$ and $\delta^{18}O_{carb}$ values) and intraclastic/micritic end-member (with higher values recording marine signatures).

2.7 Taphonomic and Paleoecological Discussion

Lamonte trevallis is interpreted as tunnels made by animals burrowing though microbial mat (Chen et al., 2013a; b) rather than by slime molds (Retallack, 2013). The truncation of microlaminae by the burrows (Fig. 2.6G) suggests that the burrowers were able to cut through the microbial mats, and no slime molds are known to be capable of truncating cm-thick microbial mats (see below). In addition, the sharp boundaries of the

tunnel walls, sometimes lined with an organic rich layer (Figs. 2.5I, 7C), suggest that these burrows may have been lined with organic material and were somewhat permanent structures. To our knowledge, no slime molds are known to be able to construct permanent tunnels within microbial mats or intraclastic sediments.

The exclusive occurrence of *Lamonte trevallis* burrows within microlaminated layers suggests a close association between the trace makers and microbial mats, and has important taphonomic and paleoecological implications. That the microlaminated layers represent remnants of amalgamated microbial mats has been discussed in Chen et al. (2013b). Briefly, this interpretation is supported by several observations including: 1) the wrinkled surfaces and crinkled microlaminae are very similar to those found in modern and Phanerozoic microbial mats (Gerdes et al., 2003; Schieber et al., 2007; Noffke, 2008); 2) the preferential concentration of clays and silts in the microlaminated layers, as suggested by both petrographic observations and elemental maps, is consistent with trapping and binding of detrital material by microbial mats (Laflamme et al., 2011b); 3) the opaque material in the microlaminated layers as seen in petrographic thin sections (Figs. 2.2D, 5A) is likely organic carbon and Fe-oxides (Fig. 2.7C), which may, respectively, have been derived from degradation and subsequent compaction of microbial mats and weathering of pyrite; and 4) the intraclastic layers probably represent episodes of rapid sedimentation, thus not allowing time for the establishment of microbial mats in the intraclastic layers.

The microbial mats probably facilitated the preservation of the burrows. It has been argued that the prevalence of microbial mats and the limited sediment mixing by shallow burrowers resulted in firm substrates and sharp geochemical gradients across the

sediment-water interfaces, as well as exceptional preservation of shallow tiers of burrows in the Ediacaran and early Cambrian periods (Droser et al., 2002). This argument is certainly applicable to the Shibantan traces. The firm microbial mats, as well as the possible linings of the Shibantan burrows, allowed the burrows to maintain their structural integrity even after they were buried by a layer of intraclastic sediments. Subsequently, the burrows were partially filled by intraclastic (and micritic) sediments which were introduced from the overlying intraclastic layers through burrow openings (i.e., vertical traces of Chen et al., 2013; Fig. 6H). This initial infilling imparted the burrows more resistance to compaction than surrounding microlaminated layers. Finally, after the burrow infill and surrounding microlaminated layers were differentially compacted, diagenetic calcite cementation occurred in both burrow infill and microlaminated layers, and residual void space in the burrows was filled by later diagenetic silica cementation. It is conceivable that microbial degradation of microbial mats, particularly through bacterial sulfate reduction, may have played a role in creating a microenvironment and providing a source of alkalinity for diagenetic calcite and later silica cementation within the microlaminated layers and the burrows (Xiao et al., 2010b).

The sequence of taphonomic events described above is supported by carbon and oxygen isotope data (Fig. 2.9). We propose that the positive $\delta^{13}C$ and mildly negative $\delta^{18}O$ values of the intraclastic layers represent normal marine signatures; similar values are typical of late Ediacaran marine carbonates elsewhere in the world (Halverson et al., 2010). Carbonate in the microlaminated layers has significantly lower $\delta^{13}C$ and $\delta^{18}O$, at least in part due to the incorporation of calcite cements formed during diagenesis, perhaps with the participation of organic degradation and meteoric fluids. The intermediate $\delta^{13}C$

and $\delta^{18}O$ values of the burrow infill fall along a mixing line in the $\delta^{13}C$–$\delta^{18}O$ cross-plot between the intraclastic and microlaminated layers, suggesting both intraclasts and diagenetic cements contributed to the burrow infill, an inference in perfect agreement with petrographic observation and the taphonomic scenario proposed above.

The taphonomic model proposed above also allows us to estimate the original (pre-compaction) thickness of the microlaminated layers. Assuming the burrows were originally cylindrical, their elliptical profile in transverse cross-section suggests that they were compacted, although the degree of compaction is less than that of the surrounding microlaminae which warp around the burrow. The original diameter of the burrows can be estimated by taking the geometric mean of the major and minor axes of the elliptical transverse cross section, thus allowing an estimate of the compaction ratio of the burrow (~1:1.5). A comparison of the restored diameter of burrows with the thickness of surrounding microlaminae extending beyond the burrows allows an estimate of the compaction ratio of the microlaminated layers (~1:9.5). Assuming that the microlaminated layers (~0.5–1.5 mm thick) represent amalgamated microbial mats, this compaction ratio indicates that the amalgamated microbial mats were ~2–14 mm in thickness, which is comparable to the thickness of modern cyanobacterial mats (Gingras et al., 2011).

The exclusive occurrence of *Lamonte trevallis* burrows within microlaminated layers or microbial mats also has important paleoecological implications. Traditionally, microbial mats have been regarded as an important nutrient resource, but recently they have also been hypothesized as “oxygen oases” for early metazoans (Seilacher, 1999; Gingras et al., 2011). Such oases, however, are limited in space and time. The oxygen

oases only exist only a few millimeters below the surface of the mats and during the day time; during night time, dissolved oxygen levels in the mat drop below levels in the overlying water column due to the production of H_2S by sulfate reduction bacteria in the mat (Gingras et al., 2011). These fluctuating conditions present a challenge for animals burrowing into the microbial mat to explore the oxygen oases. The burrowing animals need to be able to ventilate or escape from the tunnel during night time when conditions in the microbial mats become lethally sulfidic.

Although Chen et al. (2013b) propose that *L. trevallis* burrows were made to explore nutrients and oxygen in microbial mats, it appears that the oxygen oases were the main target. If nutrients were the major ecological drive, there would be no need for the feeding animals to tunnel within the mats. They could instead graze on the surface of microbial mats (particularly when predation pressure and competition for nutrients were not high in Ediacaran benthic communities), as many modern and Phanerozoic animal grazers do. In addition, the frequent occurrence of vertical traces connected to the burrows may have provided an escape or ventilation mechanism to avoid or mitigate the sulfidic conditions during night time. Of course, we cannot exclude the possibility that the burrowers exploited both oxygen and nutrients, but we believe that oxygen was the main driver.

Shibantan bioturbation intensities measured perpendicular to bedding surfaces are low (~5%), roughly equivalent to ichnofabric index 1 of Droser and Bottjer (1986); the relatively low vertical bioturbation intensities are largely due to the shallow penetration of burrows and the frequency of burrowed beds. However, when a bed is burrowed, the bedding plane bioturbation intensities measured on bedding surfaces are much higher

(22-41%), comparable to those of pre-trilobite Cambrian sediments (Dornbos et al., 2004; Marenco and Bottjer, 2008; Desjardins et al., 2010). Thus, the *L. trevallis* trace makers were the direct harbingers of the agronomic revolution in that they were some of the earliest animals capable of making tunnels within microbial mats. Although their burrow depth is limited to several millimeters, their tunnel size is relatively small, and the frequency of burrowed layers is still low compared to Cambrian carbonates, they did make the first step to explore the microbial mats, to modify the sedimentary record, and to influence the global geochemical cycles.

2.8 Conclusions

Previous reports of trace fossil assemblages from the Dengying Formation have concluded that they are usually characterized by simple horizontal traces. In this paper we describe the new ichnotaxon *Lamonte trevallis*, which is a horizontal burrow, generally elliptical or bilobed in transverse cross-section, preserved in full relief, cast by intraclasts, micrites, and diagenetic calcite and silica cements, and sometimes passing or terminating at plug-shaped nodes or vertical traces. These burrows occur exclusively in clayey and silty crinkled microlaminae that are interpreted as the remnants of microbial mats. Their close association with microbial mats has important taphonomic and ecological significance. On the basis of petrographic observations and stable isotope data, we propose a series of taphonomic events that contributed to the preservation of *L. trevallis*, including the maintenance of burrow structural integrity by firm mat-grounds, burrow infill with intraclastic and micritic sediments, sedimentary compaction, and final cementation by diagenetic calcite and silica. It appears that the trace makers tunneled the

microbial mats to mainly exploit oxygen and nutrient resources. *L. trevallis* trace makers are associated with more advanced behaviors, including under-mat tunneling, epibenthic locomotion, and temporary dwelling/resting (Chen et al., 2013b). Although *L. trevallis* burrows are relatively small in size, shallow in penetration depth, and infrequent in stratigraphic distribution, the bedding plane bioturbation intensity on burrowed beds is comparable to that of pre-trilobite Cambrian carbonates, suggesting the increasing role of late Ediacaran metazoans in modifying and modulating the benthic microbial ecosystems, sedimentary structures, and global geochemical cycles.

2.9 Acknowledgements

This work was supported by National Science Foundation, Chinese Academy of Sciences, National Natural Science Foundation of China, Chinese Ministry of Science and Technology, and Australian Research Council Discovery Grant Program.

2.10 Tables and Table Captions

Table 2.1. Average elemental concentrations (in normalized weight percentages) from EDS point analyses of burrow infill, intraclastic layers, and microlaminated layers. EDS measurements of carbon concentrations are not exact due to the low X-ray energy of carbon (K-alpha=0.277).

Table 1											
Average ± standard error (1σ)											
Type	**C**	**O**	**Mg**	**Al**	**Si**	**P**	**S**	**K**	**Ca**	**Fe**	Total
Intraclastic layer	2 ± 0.1	47 ± 0.6	0.7 ± 0	0.3 ± 0.1	0.5 ± 0.1	0.3 ± 0.1	0.2 ± 0	0.2 ± 0	49.2 ± 0.7	0.1 ± 0	100 ± 0
***L. trevallis* infill**	2.5 ± 0.4	48.1 ± 0.5	0.6 ± 0	0.2 ± 0	4.9 ± 1.1	0.1 ± 0	0.3 ± 0.1	0.2 ± 0	42.9 ± 1.4	0.1 ± 0.1	100 ± 0
Microlaminated layer	2 ± 0.4	47.5 ± 0.8	0.7 ± 0	1 ± 0.2	2.4 ± 0.6	0.3 ± 0	0.3 ± 0.1	0.7 ± 0.1	44.8 ± 1.2	0.4 ± 0.1	100 ± 0
All Samples	2.2 ± 0.3	47.5 ± 0.3	0.6 ± 0	0.5 ± 0.2	2.6 ± 1.3	0.2 ± 0	0.3 ± 0	0.4 ± 0.2	45.7 ± 1.9	0.2 ± 0.1	100 ± 0

Table 2.2. Elemental concentrations (in normalized weight percentages) from EDS point analyses of burrow infill, intraclastic layers, and microlaminated layers. EDS point analyses are identified as subfigure and spot numbers, and point locations are marked as labeled dots on Figure 10.

Sub. Fig. # (Spot #)	Spot Type	C	O	Mg	Al	Si	P	S	K	Ca	Fe	Total
1(3)	Intraclastic layer	2.65	49.06	0.76	0.22	0.78	0.14	0.21	0.24	45.94	0.00	100
1(5)	Intraclastic layer	2.43	49.85	0.52	0.47	0.59	0.25	0.13	0.37	45.38	0.00	100
1(6)	Intraclastic layer	2.94	52.32	0.62	0.27	0.32	0.23	0.17	0.14	42.99	0.00	100
1(8)	Intraclastic layer	2.40	48.69	0.62	0.25	0.26	0.16	0.31	0.20	47.09	0.00	100
1(14)	Intraclastic layer	1.74	49.75	0.58	0.20	0.21	0.14	0.15	0.17	47.06	0.00	100
1(16)	Intraclastic layer	3.76	50.77	0.86	0.31	0.29	0.12	0.18	0.10	43.61	0.00	100
2(5)	Intraclastic layer	0.98	39.08	0.88	0.31	0.33	0.13	0.31	0.21	57.76	0.00	100
2(7)	Intraclastic layer	0.33	36.53	0.50	0.04	0.12	0.20	0.23	0.28	61.77	0.00	100
2(9)	Intraclastic layer	0.64	37.82	0.78	0.22	0.19	0.14	0.29	0.25	59.66	0.00	100
2(10)	Intraclastic layer	1.19	41.75	0.98	0.19	0.25	0.11	0.25	0.18	55.09	0.00	100
2(12)	Intraclastic layer	1.39	29.93	0.38	0.02	0.07	0.06	0.26	0.20	67.69	0.00	100
2(13)	Intraclastic layer	1.83	37.57	1.03	0.13	0.11	0.08	0.21	0.10	58.83	0.11	100
3(10)	Intraclastic layer	2.62	46.89	0.87	0.26	0.27	0.16	0.39	0.18	48.27	0.09	100
3(11)	Intraclastic layer	2.58	41.03	0.89	0.09	0.13	0.10	0.15	0.24	54.80	0.00	100
3(12)	Intraclastic layer	2.77	42.95	0.81	0.02	0.04	0.03	0.16	0.22	52.69	0.31	100
3(13)	Intraclastic layer	2.16	42.30	0.67	0.11	0.12	0.07	0.23	0.17	54.10	0.07	100
3(14)	Intraclastic layer	1.73	39.88	0.33	0.08	0.60	0.06	0.23	0.16	56.80	0.12	100
3(15)	Intraclastic layer	1.48	45.35	0.72	0.16	0.38	0.12	0.24	0.14	51.41	0.00	100
3(16)	Intraclastic layer	1.34	45.62	0.78	0.22	0.24	0.13	0.20	0.18	51.30	0.00	100
3(17)	Intraclastic layer	1.19	36.30	0.25	0.00	0.04	0.01	0.16	0.12	61.82	0.11	100
3(18)	Intraclastic layer	1.72	43.45	0.57	0.05	0.08	0.06	0.14	0.12	53.68	0.14	100
5(1)	Intraclastic layer	3.75	55.11	0.85	0.92	1.09	0.17	0.11	0.41	37.45	0.13	100
5(10)	Intraclastic layer	1.65	45.20	0.55	0.34	0.73	0.25	0.18	0.41	50.52	0.18	100
5(13)	Intraclastic layer	2.41	48.03	0.61	0.24	0.43	0.13	0.19	0.30	47.65	0.00	100
5(14)	Intraclastic layer	3.43	45.55	0.59	0.17	0.34	0.31	0.45	0.25	48.91	0.00	100
5(19)	Intraclastic layer	1.03	44.72	0.52	0.08	0.16	0.18	0.16	0.25	52.90	0.00	100
6(4)	Intraclastic layer	0.76	53.76	1.09	0.36	0.40	0.24	0.14	0.13	43.02	0.10	100
6(7)	Intraclastic layer	0.39	53.84	0.81	0.34	0.34	0.23	0.26	0.19	43.55	0.04	100
6(11)	Intraclastic layer	0.93	56.31	0.56	5.03	8.24	0.10	0.17	2.73	24.88	1.04	100
6(12)	Intraclastic layer	0.81	50.79	0.49	0.14	1.56	0.12	0.40	0.20	45.40	0.10	100
6(13)	Intraclastic layer	0.76	50.20	0.52	0.73	1.31	0.37	0.19	0.62	45.22	0.09	100
6(14)	Intraclastic layer	0.84	46.10	0.35	0.49	0.96	0.25	0.23	0.60	50.06	0.13	100
6(15)	Intraclastic layer	0.00	52.04	0.62	0.22	0.20	0.17	0.19	0.23	46.24	0.11	100
7(6)	Intraclastic layer	0.72	48.60	0.54	0.15	0.95	0.15	0.25	0.22	48.29	0.14	100
7(7)	Intraclastic layer	0.63	42.63	0.26	0.20	0.53	8.20	0.61	0.36	46.50	0.07	100
7(8)	Intraclastic layer	0.87	51.69	0.77	0.08	0.12	0.13	0.14	0.09	46.05	0.08	100
7(9)	Intraclastic layer	0.49	52.26	0.55	0.10	0.18	0.17	0.22	0.21	45.82	0.00	100
7(14)	Intraclastic layer	0.83	53.44	1.16	0.28	0.26	0.22	0.28	0.18	43.15	0.21	100
7(15)	Intraclastic layer	0.77	49.36	1.02	0.25	0.24	0.24	0.30	0.25	47.40	0.17	100
7(16)	Intraclastic layer	0.29	46.15	0.81	0.23	0.99	0.23	0.34	0.24	50.72	0.00	100
7(17)	Intraclastic layer	0.86	52.40	0.77	0.74	1.06	0.29	0.21	0.50	43.08	0.09	100
7(18)	Intraclastic layer	0.72	50.53	0.53	0.11	0.23	0.18	0.23	0.17	47.27	0.04	100
8(7)	Intraclastic layer	2.84	45.03	0.55	0.17	0.22	0.09	0.20	0.16	50.64	0.10	100
8(12)	Intraclastic layer	3.01	50.36	0.91	0.25	0.20	0.10	0.18	0.15	44.81	0.04	100
8(19)	Intraclastic layer	0.85	44.81	0.77	0.20	0.34	0.20	0.29	0.46	52.08	0.00	100
8(23)	Intraclastic layer	3.72	47.97	0.65	0.24	0.25	0.11	0.19	0.24	46.64	0.00	100

Table 2.2. Cont.

8(24)	Intraclastic layer	3.78	52.59	0.61	0.22	0.27	0.11	0.10	0.16	42.07	0.08	100
8(25)	Intraclastic layer	1.49	44.36	0.25	0.03	0.20	0.08	0.13	0.22	53.13	0.10	100
8(26)	Intraclastic layer	3.42	48.50	0.77	0.34	0.39	0.23	0.27	0.29	45.61	0.19	100
8(29)	Intraclastic layer	2.92	48.10	0.63	0.17	0.35	0.13	0.20	0.23	47.10	0.16	100
8(30)	Intraclastic layer	2.08	44.61	0.36	0.02	0.20	0.08	0.18	0.24	52.08	0.15	100
9(1)	Intraclastic layer	0.76	46.30	0.71	0.19	0.22	0.20	0.23	0.32	51.07	0.00	100
9(10)	Intraclastic layer	1.41	43.31	0.61	0.19	0.19	0.15	0.26	0.19	53.61	0.08	100
9(11)	Intraclastic layer	0.82	38.86	0.26	0.00	0.03	0.08	0.23	0.23	59.37	0.12	100
9(12)	Intraclastic layer	2.17	45.07	0.56	0.19	0.22	0.19	0.20	0.27	51.13	0.00	100
9(18)	Intraclastic layer	1.91	44.97	0.70	0.16	0.15	0.17	0.21	0.20	51.53	0.00	100
10(10)	Intraclastic layer	1.10	39.96	0.66	0.14	0.19	0.09	0.25	0.23	57.38	0.00	100
10(11)	Intraclastic layer	2.57	38.27	0.43	0.06	0.23	0.03	0.26	0.25	57.58	0.32	100
10(19)	Intraclastic layer	1.19	42.45	0.68	0.13	0.22	0.20	0.24	0.22	54.66	0.00	100
11(6)	Intraclastic layer	0.77	51.16	0.78	0.18	0.35	0.16	0.19	0.09	46.17	0.15	100
11(7)	Intraclastic layer	0.02	48.63	1.14	0.24	0.22	0.00	0.26	0.13	49.34	0.01	100
11(8)	Intraclastic layer	0.69	51.15	0.82	0.18	0.23	0.12	0.24	0.11	46.35	0.11	100
11(9)	Intraclastic layer	0.88	44.55	0.72	0.12	0.21	0.21	0.21	0.18	52.74	0.18	100
11(28)	Intraclastic layer	0.72	51.89	0.88	0.27	0.35	0.18	0.26	0.15	45.26	0.05	100
11(29)	Intraclastic layer	0.75	47.18	0.59	0.15	0.37	0.38	0.23	0.13	50.09	0.12	100
11(30)	Intraclastic layer	0.02	47.48	0.84	0.19	0.28	0.25	0.00	0.00	50.81	0.13	100
11(41)	Intraclastic layer	0.70	49.35	0.75	0.20	0.28	0.16	0.27	0.14	48.07	0.07	100
11(42)	Intraclastic layer	0.72	47.40	0.91	0.26	0.23	0.18	0.26	0.13	49.84	0.07	100
11(43)	Intraclastic layer	0.80	52.29	0.85	0.23	0.67	0.14	0.21	0.08	44.61	0.13	100
11(45)	Intraclastic layer	0.03	43.78	0.41	0.21	0.81	0.10	0.00	0.46	53.98	0.24	100
11(47)	Intraclastic layer	0.02	51.16	0.92	0.24	0.35	0.00	0.33	0.10	46.78	0.10	100
11(48)	Intraclastic layer	0.75	49.92	0.80	0.23	0.26	0.27	0.33	0.22	47.05	0.17	100
11(49)	Intraclastic layer	0.79	48.75	0.91	0.26	0.31	0.23	0.29	0.14	48.25	0.07	100
11(63)	Intraclastic layer	1.23	62.37	0.31	0.01	0.12	0.00	0.00	0.06	35.91	0.00	100
11(64)	Intraclastic layer	6.72	57.77	0.52	0.02	0.16	0.00	0.00	0.00	34.81	0.00	100
1(1)	*L. trevallis* infill	3.08	48.98	0.86	0.31	0.22	0.45	0.26	0.26	45.57	0.00	100
1(10)	*L. trevallis* infill	3.16	50.23	0.79	0.29	0.32	0.28	0.25	0.21	44.47	0.00	100
1(11)	*L. trevallis* infill	2.56	50.10	0.84	0.21	0.23	0.25	0.23	0.15	45.29	0.15	100
1(12)	*L. trevallis* infill	2.61	51.81	0.70	0.24	0.27	0.15	0.23	0.15	43.85	0.00	100
2(1)	*L. trevallis* infill	1.42	41.53	0.96	0.29	0.31	0.14	0.29	0.23	54.82	0.00	100
2(2)	*L. trevallis* infill	0.59	36.29	0.49	0.08	0.15	0.11	0.23	0.24	61.81	0.00	100
2(3)	*L. trevallis* infill	2.01	44.79	0.85	0.23	0.23	0.12	0.29	0.21	51.12	0.14	100
2(15)	*L. trevallis* infill	1.04	40.44	0.81	0.26	0.33	0.31	0.26	0.23	56.21	0.11	100
2(16)	*L. trevallis* infill	0.72	38.25	0.57	0.27	2.06	0.14	0.12	0.31	57.56	0.00	100
2(17)	*L. trevallis* infill	0.88	40.63	0.43	0.04	0.12	0.08	0.20	0.17	57.45	0.00	100
3(1)	*L. trevallis* infill	1.54	46.42	0.70	0.19	0.18	0.13	0.28	0.19	50.37	0.00	100
3(2)	*L. trevallis* infill	2.49	45.47	0.64	0.10	0.11	0.06	1.28	0.14	48.87	0.84	100
3(3)	*L. trevallis* infill	2.66	45.29	0.76	0.13	0.12	0.09	0.21	0.13	50.52	0.11	100
4(1)	*L. trevallis* infill	3.66	51.15	0.35	0.00	1.45	0.00	0.00	0.00	43.39	0.00	100
4(2)	*L. trevallis* infill	0.08	57.22	0.00	0.38	33.14	0.00	0.00	0.00	9.17	0.00	100
4(3)	*L. trevallis* infill	10.68	53.48	0.11	0.00	27.42	0.00	0.00	0.00	8.31	0.00	100
4(4)	*L. trevallis* infill	5.47	53.97	0.25	0.00	2.01	0.00	0.00	0.00	38.30	0.00	100
4(5)	*L. trevallis* infill	5.17	55.33	0.20	0.00	7.98	0.00	0.00	0.00	31.31	0.00	100
5(3)	*L. trevallis* infill	3.78	47.21	0.55	0.22	2.94	0.01	0.06	0.17	44.93	0.13	100
5(4)	*L. trevallis* infill	4.12	48.94	0.63	0.20	0.23	0.08	0.33	0.15	45.25	0.06	100
5(5)	*L. trevallis* infill	1.44	46.49	0.35	0.03	0.19	0.05	0.18	0.22	51.06	0.00	100
5(6)	*L. trevallis* infill	2.27	48.41	0.51	0.19	1.05	0.09	0.19	0.17	47.12	0.00	100
5(7)	*L. trevallis* infill	3.34	50.15	0.67	0.28	0.30	0.13	0.10	0.16	44.80	0.06	100

Table 2.2. Cont.

5(8)	*L. trevallis* infill	1.92	46.29	0.41	0.10	0.46	0.10	0.16	0.24	50.19	0.13	100
5(11)	*L. trevallis* infill	2.45	47.70	0.74	0.17	0.22	0.10	0.19	0.16	48.12	0.16	100
5(16)	*L. trevallis* infill	3.07	42.87	2.24	0.22	2.20	0.10	0.23	0.29	48.78	0.00	100
5(17)	*L. trevallis* infill	2.88	48.54	0.45	0.18	0.76	0.08	0.11	0.21	46.78	0.00	100
5(20)	*L. trevallis* infill	43.68	35.61	0.43	0.20	3.75	0.00	12.57	0.00	3.28	0.49	100
6(3)	*L. trevallis* infill	0.95	52.09	0.27	0.05	4.07	0.02	0.06	0.01	42.40	0.09	100
6(5)	*L. trevallis* infill	1.02	50.55	0.45	0.70	1.15	0.33	0.16	0.64	44.82	0.17	100
6(6)	*L. trevallis* infill	0.82	52.98	1.23	3.20	5.23	1.55	0.31	1.38	33.17	0.14	100
6(8)	*L. trevallis* infill	0.99	49.66	0.47	0.09	0.20	0.15	0.11	0.23	48.02	0.08	100
7(1)	*L. trevallis* infill	0.87	52.91	0.59	0.27	0.35	0.17	0.19	0.21	44.33	0.10	100
7(2)	*L. trevallis* infill	0.78	52.53	0.89	0.22	0.29	0.18	0.28	0.23	44.55	0.07	100
7(3)	*L. trevallis* infill	0.74	44.80	0.12	0.00	0.09	0.14	0.16	0.35	53.55	0.05	100
7(4)	*L. trevallis* infill	0.89	51.73	0.57	0.37	17.94	0.22	0.32	0.14	27.72	0.09	100
7(5)	*L. trevallis* infill	0.86	49.94	0.38	0.20	0.26	0.17	0.17	0.33	47.62	0.06	100
7(10)	*L. trevallis* infill	0.92	50.40	0.65	0.15	0.24	0.15	0.16	0.27	46.99	0.07	100
7(11)	*L. trevallis* infill	0.90	52.99	0.67	0.16	0.29	0.14	0.21	0.20	44.38	0.05	100
7(12)	*L. trevallis* infill	0.86	52.40	0.23	0.00	0.13	0.07	0.16	0.23	45.80	0.11	100
7(13)	*L. trevallis* infill	0.90	49.39	0.10	0.00	6.11	0.02	0.09	0.15	43.05	0.18	100
8(1)	*L. trevallis* infill	3.22	51.36	0.68	0.25	0.18	0.14	0.14	0.13	43.80	0.10	100
8(2)	*L. trevallis* infill	2.42	46.39	0.45	0.14	0.20	0.09	0.24	0.17	49.91	0.00	100
8(3)	*L. trevallis* infill	2.60	50.05	0.55	0.22	1.84	0.12	0.21	0.16	44.26	0.00	100
8(4)	*L. trevallis* infill	2.64	49.99	0.62	0.19	0.49	0.09	0.19	0.16	45.63	0.00	100
8(8)	*L. trevallis* infill	3.32	49.06	0.45	0.07	0.09	0.06	0.14	0.12	46.55	0.14	100
8(9)	*L. trevallis* infill	2.75	49.76	0.66	0.24	0.28	0.13	0.25	0.22	45.71	0.00	100
8(14)	*L. trevallis* infill	2.83	48.71	0.59	0.14	0.27	0.09	0.22	0.15	46.93	0.07	100
8(15)	*L. trevallis* infill	3.16	47.01	0.56	0.16	0.16	0.09	0.13	0.13	48.43	0.18	100
8(16)	*L. trevallis* infill	2.99	50.22	0.66	0.20	0.24	0.12	0.19	0.18	45.04	0.15	100
8(17)	*L. trevallis* infill	2.67	47.30	0.48	0.14	0.48	0.08	0.21	0.27	48.14	0.22	100
8(21)	*L. trevallis* infill	3.06	45.66	0.40	0.08	0.45	0.07	0.15	0.22	49.85	0.07	100
9(3)	*L. trevallis* infill	5.32	47.77	0.30	0.65	45.33	0.09	0.07	0.08	0.40	0.00	100
9(4)	*L. trevallis* infill	3.25	56.08	0.74	0.37	6.20	0.15	0.16	0.12	32.92	0.00	100
9(5)	*L. trevallis* infill	2.61	52.70	0.75	0.46	0.62	0.13	0.27	0.21	42.13	0.12	100
9(6)	*L. trevallis* infill	2.30	48.75	0.85	0.31	0.38	0.19	0.42	0.21	46.40	0.19	100
9(7)	*L. trevallis* infill	5.72	55.05	0.35	0.38	18.43	0.11	0.12	0.08	19.59	0.17	100
9(8)	*L. trevallis* infill	2.20	47.06	0.48	0.13	0.15	0.12	0.16	0.15	49.56	0.00	100
9(14)	*L. trevallis* infill	2.37	44.95	0.48	0.24	1.53	0.15	0.18	0.28	49.66	0.17	100
9(15)	*L. trevallis* infill	3.28	50.45	0.72	0.23	0.48	0.11	0.17	0.22	44.25	0.09	100
10(1)	*L. trevallis* infill	2.11	38.00	0.23	0.04	1.11	0.04	0.61	0.24	57.62	0.00	100
10(2)	*L. trevallis* infill	2.86	48.93	1.27	0.28	0.26	0.09	0.17	0.18	45.91	0.05	100
10(3)	*L. trevallis* infill	2.94	53.50	0.64	0.21	0.19	0.09	0.17	0.17	41.96	0.12	100
10(4)	*L. trevallis* infill	0.73	37.49	0.22	0.02	0.45	0.04	0.14	0.24	60.68	0.00	100
10(5)	*L. trevallis* infill	5.30	50.29	0.55	0.83	39.74	0.15	0.15	0.14	2.86	0.00	100
10(6)	*L. trevallis* infill	1.07	38.53	0.51	0.16	0.31	0.10	0.25	0.28	58.80	0.00	100
10(7)	*L. trevallis* infill	0.56	33.78	0.34	0.05	2.45	0.03	0.32	0.27	62.20	0.00	100
10(13)	*L. trevallis* infill	1.87	45.61	0.52	0.44	2.32	0.12	0.18	0.35	43.52	5.07	100
10(14)	*L. trevallis* infill	0.41	39.11	0.42	0.04	0.21	0.06	0.22	0.16	59.37	0.00	100
10(15)	*L. trevallis* infill	2.02	43.28	0.51	0.12	0.41	0.04	0.18	0.11	53.23	0.09	100
10(16)	*L. trevallis* infill	3.09	45.17	0.44	0.49	27.08	0.22	0.26	0.21	22.91	0.13	100
10(17)	*L. trevallis* infill	2.77	49.89	0.84	0.29	2.26	0.10	0.18	0.12	43.44	0.11	100
10(18)	*L. trevallis* infill	2.87	45.36	0.84	0.29	2.21	0.11	0.26	0.21	47.67	0.16	100
10(21)	*L. trevallis* infill	0.77	44.10	0.60	0.13	0.23	0.08	0.17	0.16	53.76	0.00	100
10(22)	*L. trevallis* infill	2.22	43.38	0.66	0.26	9.71	0.15	0.20	0.14	43.21	0.06	100

Table 2.2. Cont.

10(23)	*L. trevallis* infill	2.67	52.17	1.01	0.35	0.27	0.10	0.15	0.13	42.99	0.17	100
10(24)	*L. trevallis* infill	1.44	35.92	0.04	0.00	0.39	0.05	0.14	0.32	61.70	0.00	100
11(1)	*L. trevallis* infill	0.70	47.86	0.72	0.26	0.37	0.18	0.34	0.13	49.34	0.10	100
11(2)	*L. trevallis* infill	0.72	47.49	0.86	0.29	0.50	0.19	0.36	0.00	49.47	0.11	100
11(3)	*L. trevallis* infill	0.71	50.16	0.75	0.27	0.35	0.27	0.26	0.10	47.08	0.05	100
11(4)	*L. trevallis* infill	0.03	49.59	0.82	0.26	0.35	0.00	0.23	0.19	48.41	0.13	100
11(5)	*L. trevallis* infill	0.76	47.46	0.78	0.30	0.54	0.17	0.00	0.25	49.56	0.18	100
11(17)	*L. trevallis* infill	0.70	49.94	0.80	0.36	2.49	0.00	0.26	0.14	45.26	0.05	100
11(18)	*L. trevallis* infill	0.74	48.95	0.79	0.41	12.54	0.12	0.19	0.11	36.10	0.04	100
11(19)	*L. trevallis* infill	0.73	45.46	0.73	0.20	0.40	0.17	0.22	0.26	51.76	0.08	100
11(20)	*L. trevallis* infill	0.69	48.68	0.55	0.18	0.35	0.11	0.30	0.01	49.03	0.12	100
11(21)	*L. trevallis* infill	0.80	48.02	0.58	0.17	0.36	0.16	0.32	0.11	49.35	0.13	100
11(22)	*L. trevallis* infill	0.71	50.53	0.86	0.28	0.48	0.19	0.32	0.18	46.37	0.08	100
11(23)	*L. trevallis* infill	0.62	48.83	0.72	0.31	0.91	0.18	0.23	0.00	48.16	0.04	100
11(24)	*L. trevallis* infill	0.73	51.39	0.27	0.14	12.03	0.00	0.04	0.00	35.32	0.08	100
11(25)	*L. trevallis* infill	0.74	47.82	0.75	0.27	0.68	0.19	0.30	0.15	48.98	0.12	100
11(26)	*L. trevallis* infill	0.49	46.99	0.32	0.83	45.30	0.00	0.17	0.11	5.78	0.00	100
11(27)	*L. trevallis* infill	0.85	48.87	0.57	0.18	0.38	0.18	0.23	0.20	48.48	0.08	100
11(37)	*L. trevallis* infill	0.89	49.95	0.38	0.24	12.87	0.02	0.15	0.10	35.25	0.14	100
11(38)	*L. trevallis* infill	0.77	50.73	0.92	0.76	1.33	0.28	0.30	0.53	44.27	0.10	100
11(39)	*L. trevallis* infill	0.82	48.90	0.61	0.17	0.58	0.17	0.27	0.01	48.43	0.05	100
11(40)	*L. trevallis* infill	0.45	51.54	0.19	0.17	21.32	0.00	0.01	0.01	26.12	0.19	100
11(57)	*L. trevallis* infill	10.17	55.70	0.30	0.01	0.23	0.00	0.00	0.00	33.59	0.00	100
11(58)	*L. trevallis* infill	1.61	52.63	0.00	0.00	0.00	0.00	0.00	0.00	45.76	0.00	100
11(59)	*L. trevallis* infill	1.03	53.86	0.00	0.00	45.11	0.00	0.00	0.00	0.00	0.00	100
11(60)	*L. trevallis* infill	1.03	55.01	0.00	0.00	43.96	0.00	0.00	0.00	0.00	0.00	100
1(2)	Microlaminated layer	0.00	42.31	0.16	0.05	0.29	0.11	0.82	0.40	55.85	0.00	100
1(4)	Microlaminated layer	2.70	54.24	0.36	0.66	1.25	0.21	0.30	0.68	39.60	0.00	100
1(7)	Microlaminated layer	2.02	50.47	0.74	0.22	0.26	0.15	0.23	0.19	45.72	0.00	100
1(9)	Microlaminated layer	2.47	49.95	0.66	0.65	0.85	0.49	0.17	0.40	44.36	0.00	100
1(13)	Microlaminated layer	2.32	48.52	0.91	0.24	0.42	0.14	0.14	0.19	47.11	0.00	100
1(15)	Microlaminated layer	1.80	43.49	0.27	0.09	0.60	0.12	0.35	0.27	53.00	0.00	100
2(4)	Microlaminated layer	26.71	42.03	0.81	1.06	2.39	0.08	5.33	0.37	20.70	0.51	100
2(6)	Microlaminated layer	0.46	33.42	0.43	0.48	0.61	0.13	0.24	0.42	63.81	0.00	100
2(8)	Microlaminated layer	0.81	35.28	1.04	0.12	0.28	0.12	0.15	0.33	61.85	0.00	100
2(11)	Microlaminated layer	1.24	43.88	1.09	0.28	0.28	0.11	0.23	0.20	52.69	0.00	100
2(14)	Microlaminated layer	1.93	44.66	0.84	0.65	0.73	0.10	0.18	0.35	50.57	0.00	100
2(18)	Microlaminated layer	1.47	39.31	0.00	2.00	8.35	0.00	0.00	4.96	35.60	8.32	100
3(4)	Microlaminated layer	2.71	49.83	0.79	0.48	1.21	0.15	0.19	0.34	44.23	0.06	100
3(5)	Microlaminated layer	3.19	51.87	0.75	0.42	0.34	0.23	0.13	0.27	42.64	0.16	100
3(6)	Microlaminated layer	1.67	40.88	0.27	0.19	0.50	0.07	0.11	0.51	55.81	0.00	100
3(7)	Microlaminated layer	2.40	45.25	0.91	0.20	0.23	0.14	0.22	0.18	50.33	0.16	100
3(8)	Microlaminated layer	2.48	37.27	0.42	3.63	11.94	0.35	0.77	2.52	39.67	0.94	100
3(9)	Microlaminated layer	1.55	42.82	0.54	3.91	6.21	1.42	0.35	2.66	39.55	0.99	100
5(2)	Microlaminated layer	6.15	56.42	0.96	0.68	0.74	0.14	0.17	0.20	34.39	0.15	100
5(9)	Microlaminated layer	1.95	46.04	0.66	0.18	0.40	0.09	0.22	0.27	50.04	0.16	100
5(12)	Microlaminated layer	3.24	46.58	0.46	0.64	1.59	0.42	0.24	0.68	46.16	0.00	100
5(15)	Microlaminated layer	4.92	55.78	0.93	1.76	2.35	0.19	0.18	0.76	32.83	0.30	100

Table 2.2. Cont.

5(18)	Microlaminated layer	1.79	48.15	0.37	0.08	0.18	0.15	0.19	0.34	48.75	0.00	100
6(1)	Microlaminated layer	0.83	53.98	1.16	0.33	0.27	0.19	0.15	0.15	42.83	0.11	100
6(2)	Microlaminated layer	1.02	50.83	0.84	0.09	0.25	0.17	0.14	0.25	46.36	0.05	100
6(9)	Microlaminated layer	0.77	53.23	1.00	0.52	0.57	0.22	0.23	0.34	43.03	0.09	100
6(10)	Microlaminated layer	0.06	60.25	0.87	6.14	8.92	0.37	0.02	2.86	20.51	0.00	100
6(16)	Microlaminated layer	0.81	52.06	0.82	0.16	0.29	0.16	0.11	0.13	45.43	0.03	100
8(5)	Microlaminated layer	1.45	45.32	0.40	0.09	1.41	0.10	0.19	0.23	50.79	0.00	100
8(6)	Microlaminated layer	1.95	45.02	0.51	0.14	0.20	0.12	0.17	0.23	51.55	0.11	100
8(10)	Microlaminated layer	1.78	45.67	0.66	0.00	0.63	0.17	0.14	0.49	50.09	0.37	100
8(11)	Microlaminated layer	2.52	52.46	0.74	2.76	4.18	0.07	0.10	1.48	35.24	0.45	100
8(13)	Microlaminated layer	5.37	45.54	0.52	1.59	2.95	0.14	0.27	1.14	41.88	0.60	100
8(18)	Microlaminated layer	0.92	49.41	0.79	1.83	2.90	2.34	0.30	1.14	40.36	0.00	100
8(20)	Microlaminated layer	3.64	43.49	0.02	0.51	34.05	0.00	0.01	0.12	18.15	0.00	100
8(22)	Microlaminated layer	1.37	21.01	0.00	0.00	0.50	0.00	0.32	1.04	75.76	0.00	100
8(27)	Microlaminated layer	2.74	44.31	0.37	0.62	1.02	0.29	0.17	0.67	49.65	0.16	100
8(28)	Microlaminated layer	3.38	49.13	0.53	0.34	0.42	0.17	0.22	0.29	45.39	0.13	100
9(2)	Microlaminated layer	2.07	48.78	0.60	1.05	1.34	0.23	0.14	0.60	41.77	3.41	100
9(9)	Microlaminated layer	0.88	40.27	0.67	0.00	0.56	0.05	0.15	0.17	57.24	0.00	100
9(13)	Microlaminated layer	2.62	46.91	0.80	1.00	1.83	0.32	0.22	0.63	45.67	0.00	100
9(16)	Microlaminated layer	2.30	46.65	0.80	3.50	5.26	0.66	0.12	2.05	37.83	0.84	100
9(17)	Microlaminated layer	3.04	50.92	0.43	0.27	0.38	0.06	0.11	0.31	44.27	0.21	100
10(8)	Microlaminated layer	2.63	52.98	1.15	1.52	2.02	0.38	0.17	0.58	38.28	0.30	100
10(9)	Microlaminated layer	0.71	39.15	0.99	0.50	0.60	0.28	0.33	0.45	56.77	0.22	100
10(12)	Microlaminated layer	2.41	51.68	1.00	2.07	3.96	1.20	0.20	1.11	34.30	2.09	100
10(20)	Microlaminated layer	1.11	44.56	0.73	0.18	0.21	0.12	0.15	0.16	52.78	0.00	100
11(10)	Microlaminated layer	0.90	51.00	0.74	0.72	3.59	0.14	0.17	0.41	41.99	0.34	100
11(11)	Microlaminated layer	0.98	43.32	0.00	0.30	1.09	0.32	0.01	0.95	52.35	0.68	100
11(12)	Microlaminated layer	0.79	48.39	0.65	0.09	0.25	0.10	0.24	0.19	49.15	0.14	100
11(13)	Microlaminated layer	0.38	49.33	0.76	0.23	0.88	0.17	0.34	0.21	47.62	0.08	100
11(14)	Microlaminated layer	0.81	43.95	0.22	0.43	1.05	0.34	0.16	0.53	51.61	0.89	100
11(15)	Microlaminated layer	0.69	47.98	0.78	0.40	0.64	0.25	0.21	0.26	48.56	0.23	100
11(16)	Microlaminated layer	0.33	46.50	0.93	0.33	0.50	0.24	0.15	0.04	50.91	0.06	100
11(31)	Microlaminated layer	0.26	49.59	1.41	6.20	11.01	0.81	0.40	2.86	25.97	1.49	100
11(32)	Microlaminated layer	0.74	47.28	0.90	4.10	6.45	0.74	0.41	2.69	34.58	2.11	100
11(33)	Microlaminated layer	0.73	50.45	0.60	2.62	3.32	0.20	0.09	1.25	40.13	0.61	100
11(34)	Microlaminated layer	0.65	48.97	0.63	0.17	0.29	0.14	0.25	0.23	48.59	0.07	100
11(35)	Microlaminated layer	0.02	46.52	0.82	0.78	1.32	0.29	0.00	0.52	49.38	0.34	100
11(36)	Microlaminated layer	0.03	49.50	0.71	0.46	0.61	0.00	0.21	0.25	48.09	0.15	100
11(44)	Microlaminated layer	0.76	52.40	1.01	0.60	0.97	0.63	0.20	0.34	42.97	0.12	100
11(46)	Microlaminated layer	0.02	52.37	1.33	4.33	11.30	0.38	0.00	1.90	27.83	0.53	100
11(50)	Microlaminated layer	0.82	46.75	0.76	0.19	0.33	0.20	0.24	0.20	50.34	0.17	100
11(51)	Microlaminated layer	0.83	34.23	0.00	0.00	0.26	0.00	0.00	0.15	64.30	0.24	100
11(52)	Microlaminated layer	0.74	52.80	0.98	1.85	6.55	0.64	0.20	0.78	35.03	0.42	100
11(53)	Microlaminated layer	0.73	49.89	1.04	0.34	0.29	0.24	0.27	0.16	46.97	0.08	100
11(54)	Microlaminated layer	0.87	49.37	0.84	0.23	0.33	0.19	0.26	0.15	47.64	0.13	100
11(55)	Microlaminated layer	0.89	48.93	0.69	0.16	0.20	0.16	0.28	0.20	48.36	0.12	100
11(56)	Microlaminated layer	0.63	53.05	0.66	0.88	1.24	0.34	0.17	0.62	42.21	0.19	100
11(61)	Microlaminated layer	0.50	64.79	0.00	0.00	0.85	0.00	0.00	0.00	33.86	0.00	100
11(62)	Microlaminated layer	3.26	64.60	0.28	0.00	1.09	0.00	0.00	0.00	30.77	0.00	100

Table 2.3. $\delta^{13}C_{carb}$ and $\delta^{18}O_{carb}$ values of burrow infill, intraclastic layers, and microlaminated layers. Analyses are identified as subfigure and spot numbers, and microsample locations are marked as labeled dots on Figure 10.

Sub. Fig. # (Spot #)	Sample Type	$\delta^{13}C$	$\delta^{18}O$
1(1)	Intraclastic layer	3.5	-4.4
1(4)	Intraclastic layer	3.8	-4.5
2(1)	Intraclastic layer	4.0	-2.9
2(2)	Intraclastic layer	3.2	-4.4
2(5)	Intraclastic layer	4.2	-3.0
3(5)	Intraclastic layer	3.8	-2.8
3(6)	Intraclastic layer	3.6	-4.4
4(5)	Intraclastic layer	3.8	-4.2
5(6)	Intraclastic layer	3.9	-4.3
5(7)	Intraclastic layer	3.9	-4.0
6(5)	Intraclastic layer	4.1	-3.7
6(6)	Intraclastic layer	3.8	-4.3
7(4)	Intraclastic layer	4.1	-4.1
7(5)	Intraclastic layer	4.2	-3.9
8(4)	Intraclastic layer	4.2	-3.1
8(5)	Intraclastic layer	4.3	-3.5
8(7)	Intraclastic layer	4.2	-3.1
3(1)	Microlaminated layer	2.0	-6.3
4(1)	Microlaminated layer	2.3	-5.4
4(3)	Microlaminated layer	1.8	-6.1
4(4)	Microlaminated layer	2.4	-5.2
5(1)	Microlaminated layer	1.2	-6.8
5(5)	Microlaminated layer	1.8	-6.6
6(3)	Microlaminated layer	2.1	-5.6
6(4)	Microlaminated layer	2.0	-5.7
7(3)	Microlaminated layer	2.2	-6.0
8(3)	Microlaminated layer	1.8	-6.6
1(2)	*L. trevallis* infill	3.3	-5.1
1(3)	*L. trevallis* infill	3.2	-5.5
2(3)	*L. trevallis* infill	3.2	-5.1
2(4)	*L. trevallis* infill	3.3	-5.0
3(2)	*L. trevallis* infill	3.0	-5.4
3(3)	*L. trevallis* infill	2.8	-5.3
3(4)	*L. trevallis* infill	3.0	-5.4
4(2)	*L. trevallis* infill	3.0	-5.2
5(2)	*L. trevallis* infill	3.0	-5.6
5(3)	*L. trevallis* infill	3.0	-5.4
5(4)	*L. trevallis* infill	2.9	-5.8
6(1)	*L. trevallis* infill	3.4	-5.1

Table 2.3. Cont.

6(2)	*L. trevallis* infill	3.3	-5.0
7(1)	*L. trevallis* infill	3.0	-5.3
7(2)	*L. trevallis* infill	3.3	-5.2
8(1)	*L. trevallis* infill	3.0	-5.6
8(2)	*L. trevallis* infill	3.2	-5.1
8(6)	*L. trevallis* infill	3.0	-5.3
Average ± standard error (1σ)			
Matrix		3.9 ± 0.1	-3.8 ± 0.1
Microlaminae		2.0 ± 0.1	-6.0 ± 0.2
Infill Cement		3.1 ± 0	-5.3 ± 0

2.1 Figure and Figure Captions

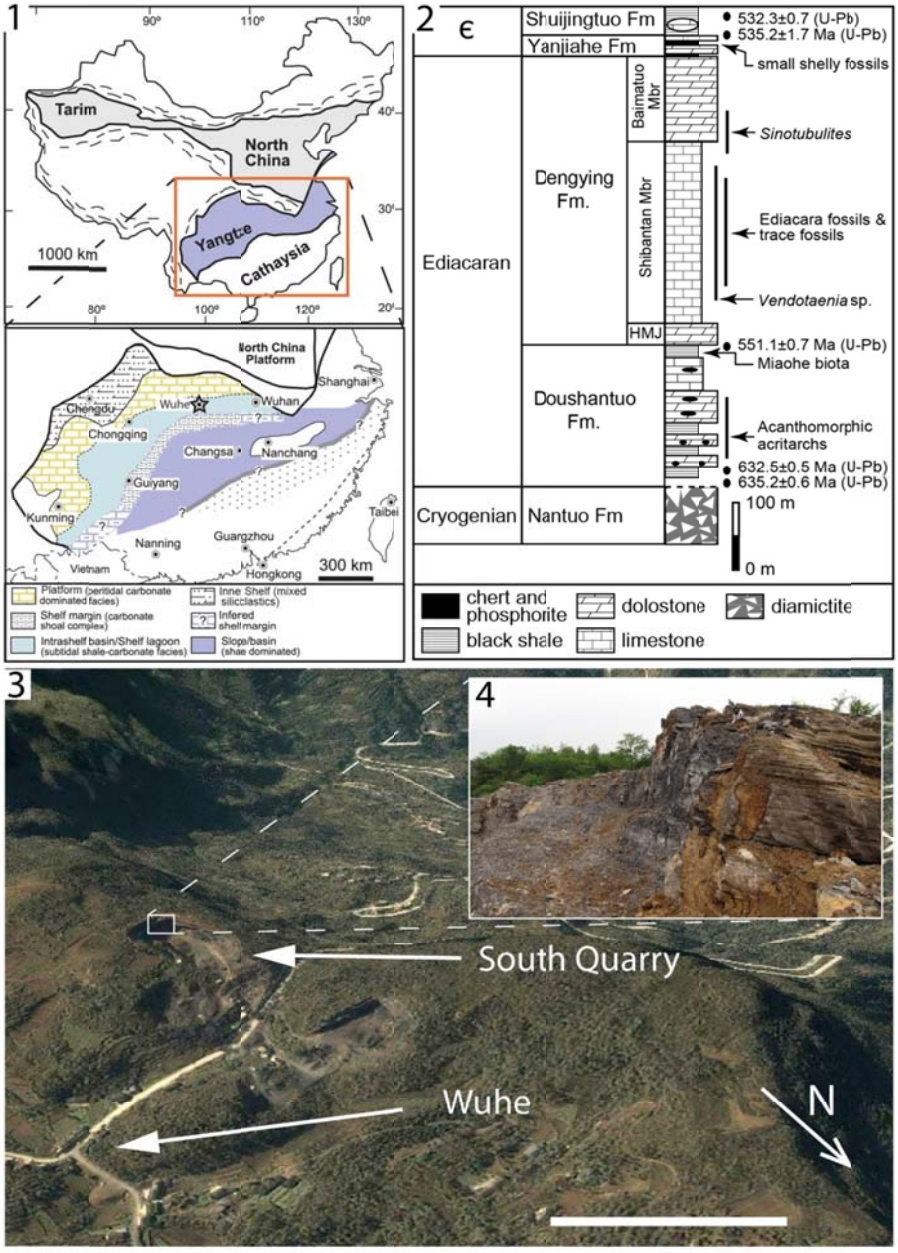

Fig. 2.1. Geological map and stratigraphic column. (A) Simplified geological map showing the major tectonic units in China and Ediacaran paleogeographic map of the Yangtze Craton showing facies distribution. Adopted from Jiang et al. (2011). (B) Stratigraphic column of the Doushantuo and Dengying formations showing stratigraphic occurrences of trace fossils in the Shibantan Member of the Dengying Formation. (C) Google Earth view showing quarry location west of Wuhe. Rectangle denotes fossil site. (D) View looking southeast to fossil site. Scale bar in C = 0.25 km.

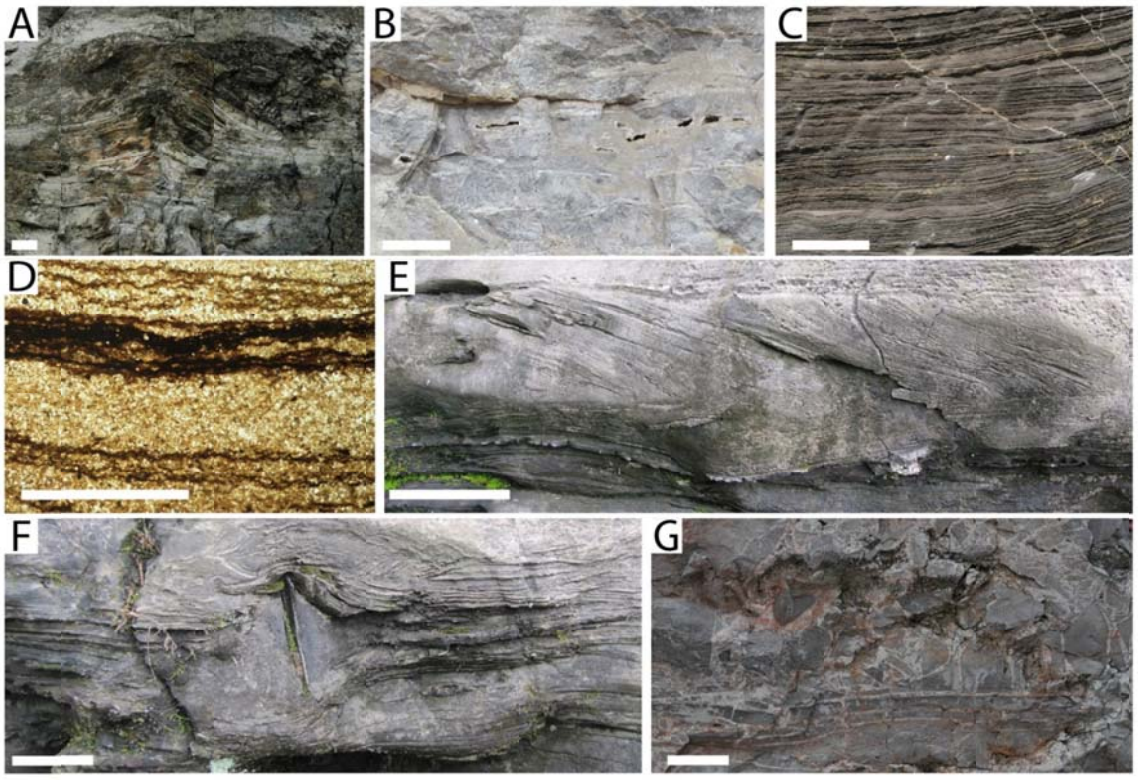

Fig. 2.2. Sedimentary structures of the Dengying Formation. (A) Tepee structures from the Hamajing Member. (B) Dissolution vugs from the Hamajing Member. (C) Closer view of the thin-bedded limestone in the quarry where the trace fossils were collected. (D) Transmitted light photomicrograph of microlaminated and intraclastic layers. (E) Cross stratification in the Shibantan Member. (F) Rip-up clast and convoluted bedding in the Shibantan Member. (G) Breccia and dissolution vugs in the Baimatuo Member. Scale bars in A–C, E–G = 10 cm, D = 1 mm.

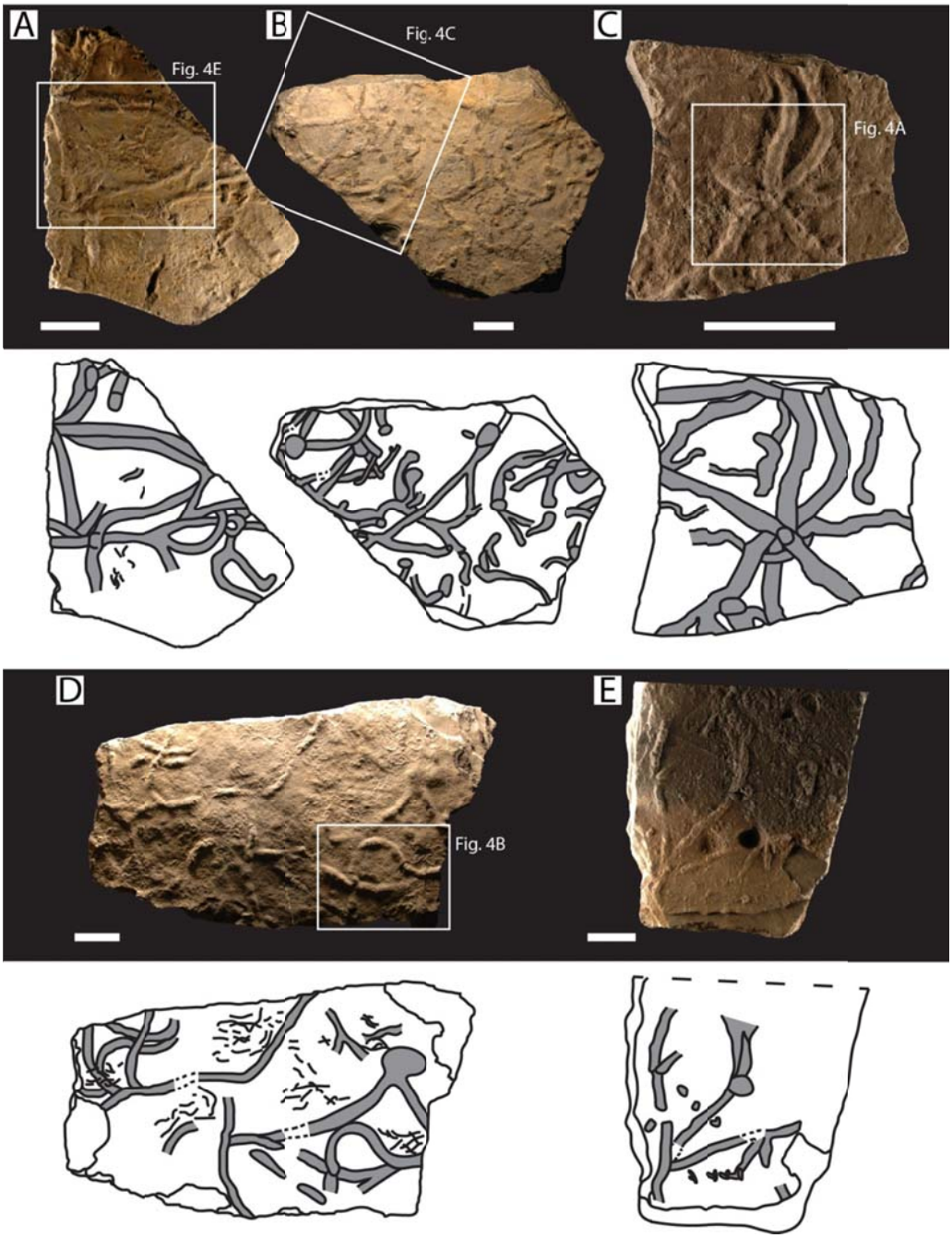

Fig. 2.3. Light photographs and corresponding interpretive drawings of trace fossil-bearing slabs, inferred top bedding surface (⊤) shown. Scale bars = 5 cm. *Lamonte trevallis* burrows are marked in gray color, and small and undescribed trace fossils are marked in black lines (e.g., Fig. 3A and 3D). Rectangles mark areas magnified in Fig. 4A–C, E. (A) VPIGM-4642. (B) VPIGM-4653. (C) VPIGM-4668. (D–E) VPIGM-4670.

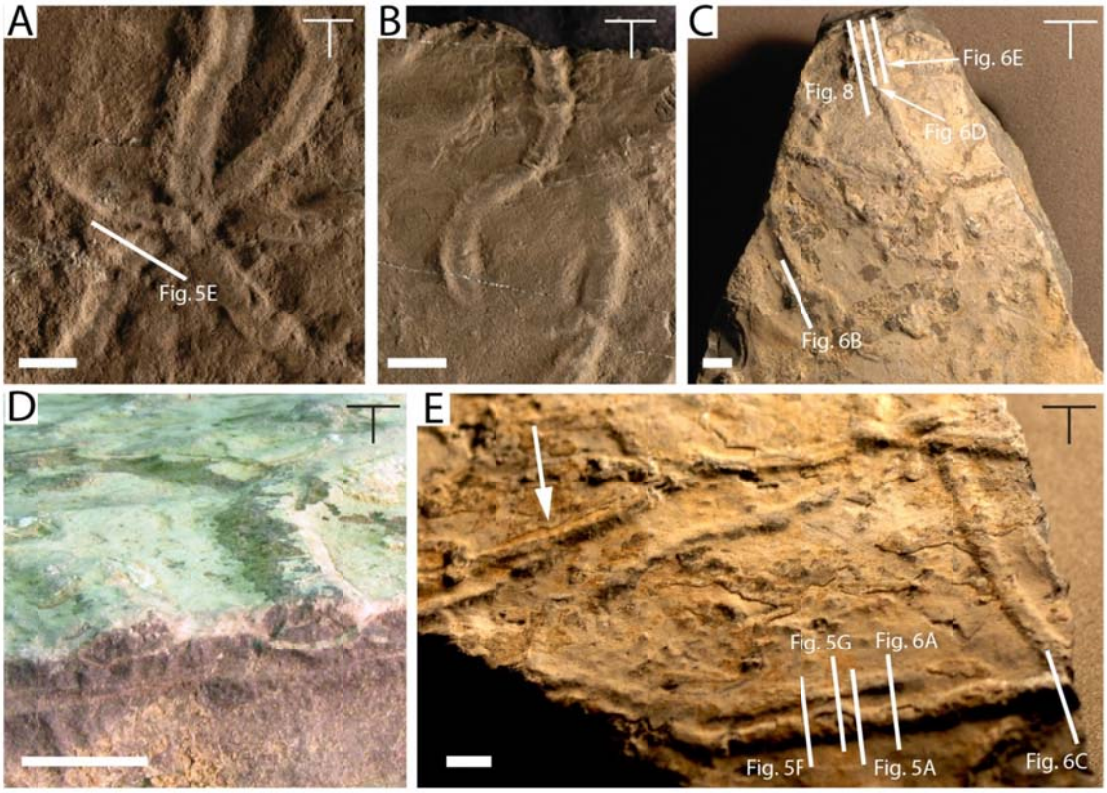

Fig. 2.4. Photographs of trace fossils on inferred top bedding surface (⊤). (A) Magnified view of box area in Figure 3C showing several burrows overlapping at one spot, VPIGM-4668. (B) Magnified view of box area in Figure 3D (rotated counter clock-wise 90 degrees), VPIGM-4670. (C) Slab with multiple burrows, VPIGM-4653. (D) Oblique view of tunnels on bedding surface and in cross-section, showing burrows enveloped by light-colored clay layer, VPIGM-4653. (E) Magnified view of box area in Figure 3A showing overlapping burrows. Labeled lines denote cross sections featured in Fig. 5. Arrow points to holotype of *Lamonte trevallis*, VPIGM-4643. Slab pictured is VPIGM-4642. Scale bars = 1 cm.

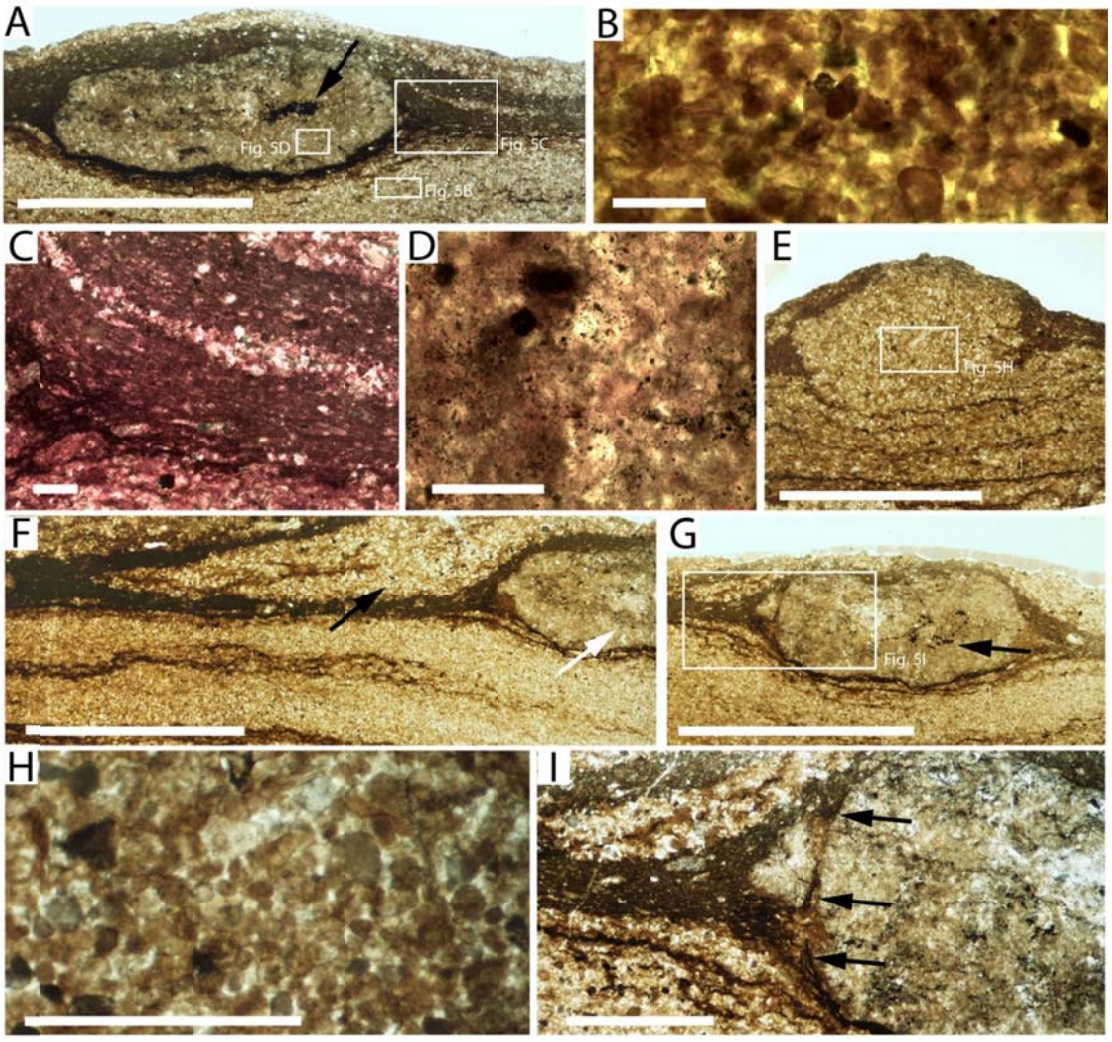

Fig. 2.5. Transmitted light photomicrographs of burrows in cross-sections perpendicular to bedding plane, all shown with inferred stratigraphic up direction on top. (A) Bilobed burrow filled with micritic sediments, cements, and bitumen (arrow). Boxes denoting areas magnified in Fig. 5B–D, VPIGM-4644. (B) Closer view of grains in intraclastic layers. (C) Closer view of crinkled microlaminae in microlaminated layers. (D) Micritic burrow infill with cements. (E) Burrow filled with intraclasts. Box denotes area magnified in Fig. 5H, VPIGM-4669. (F) Two overlapping burrows, one of which is obliquely cut and filled with intraclasts (black arrow), whereas the other is filled mostly with micrites (white arrow). Burrows are separated by a microlaminated layer, VPIGM-4645. (G) Burrow with micrites, cements, and bitumen (arrow). Box denotes area magnified in Fig. 5I, VPIGM-4646. (H) Magnified view of Fig. 5E showing intraclasts in cement. (I) Magnified view of Fig. 5G showing possible burrow lining (arrows). Scale bars in A = 5 mm, B–D = 100 μm, E–G = 5 mm, H–I = 1 mm.

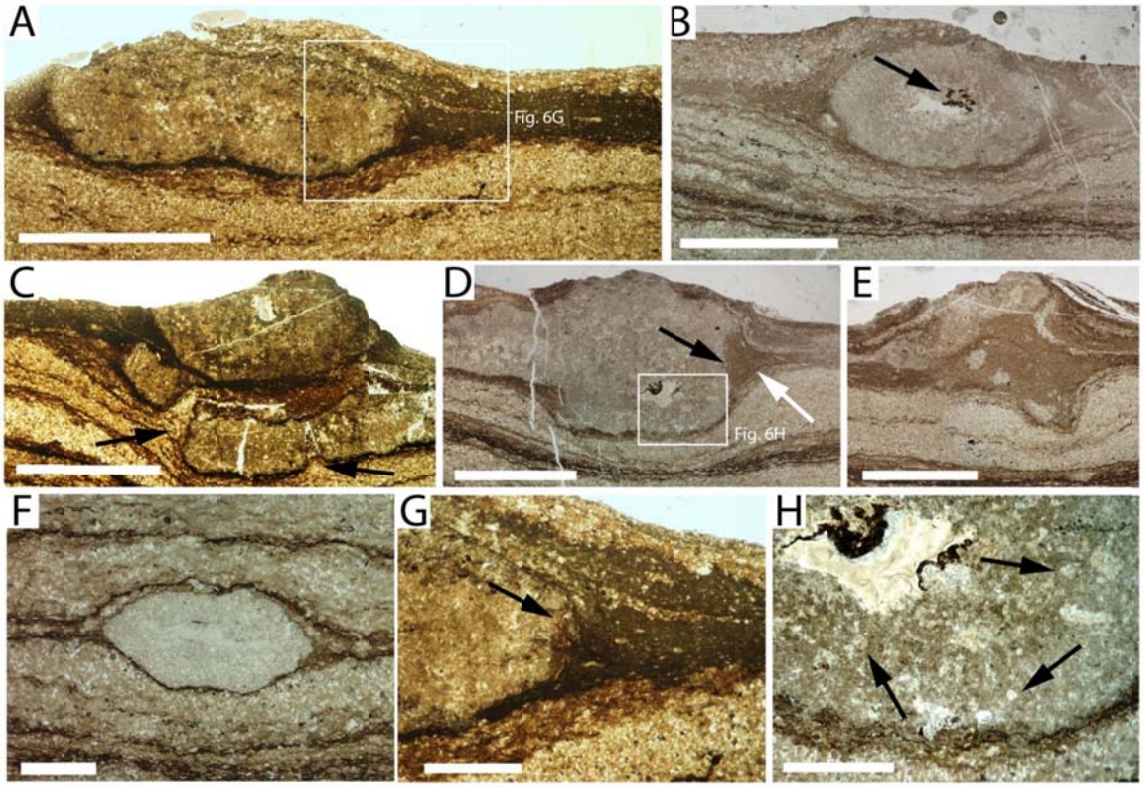

Fig. 2.6. Transmitted light photomicrographs of burrows and vertical traces in cross-sections perpendicular to bedding plane, all shown with inferred stratigraphic up direction on top. (A) Bilobed burrow filled with micrites and cements. Box denotes area magnified in Fig. 6G, VPIGM-4647. (B) Partially exposed burrow filled with micrites and some intraclasts, cements, and bitumen (arrow), VPIGM-4654. (C) Overlapping burrows, with the lower unexposed burrow cut obliquely. Arrows point to breaks in the unexposed burrow, probably due to during compaction, VPIGM-4648. (D–E) Plugs or vertical traces showing splitting and truncation of microlaminas (white and black arrows in Fig. 6D, respectively). D, VPIGM-4655. E, VPIGM-4656. Box denotes area magnified in Fig. 6H. (F) Unexposed burrow filled with micrites and cements, VPIGM-4671. (G) Magnified view of box in Fig. 5A showing truncation of microlaminae (arrow). (H) Magnified view of box in Fig. 5D, arrows point to intraclasts within the infill cement. Scale bars in A–E = 5 mm, F–H = 1 mm.

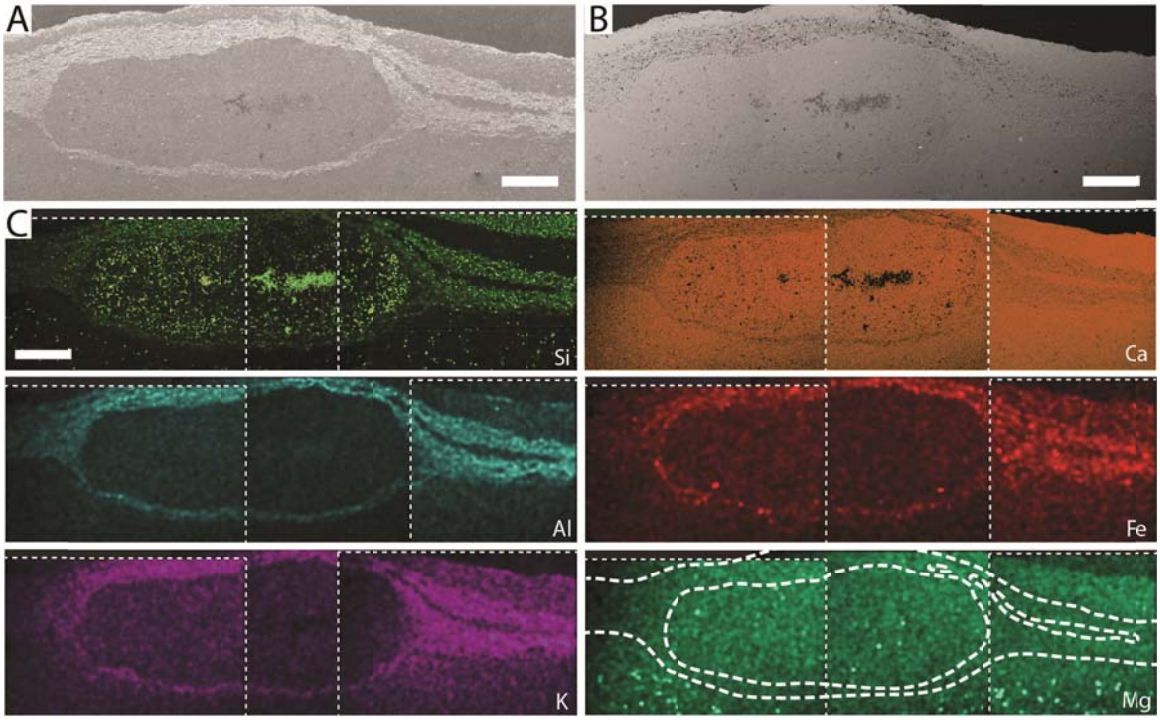

Fig. 2.7. SEM images and EDS elemental maps of *Lamonte trevallis* burrow in cross-section (see also Fig. 5A), VPIGM-4644. (A) SE SEM image. (B) BSE SEM image. (C) Composite elemental maps. Thin dashed lines represent boundaries of individual elemental maps. Thick dashed lines in Mg map outline microlaminae and burrow. All scale bars = 1 mm.

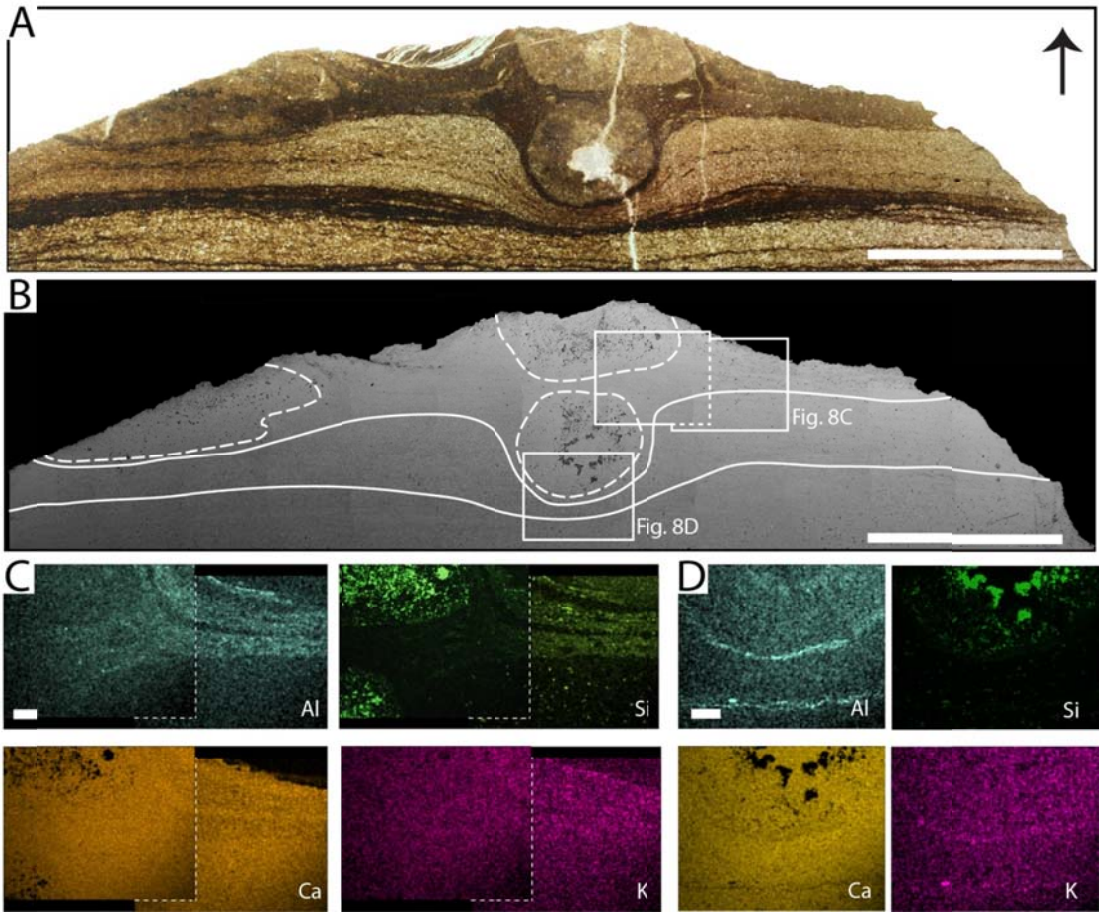

Fig. 2.8. Transmitted light photomicrograph, BSE images and EDS elemental maps of two overlapping burrows (one exposed, and the other unexposed) in cross-section perpendicular to bedding plane, VPIGM-4657. Slab illustrated in Figure 4C. (A) Transmitted light image. Arrow points to inferred stratigraphic up direction. (B) BSE image. Solid and dashed lines denote sedimentary laminae and burrows, respectively. Boxes denote elemental map areas in Fig. 8C–D. (C) Composite elemental maps of labeled boxes in Figure 7B. (D) Elemental map of labeled box in Figure 7B. Dashed lines represent boundaries of individual elemental maps. Scale bars in 1–2 = 1 cm, in 3–4 = 1 mm.

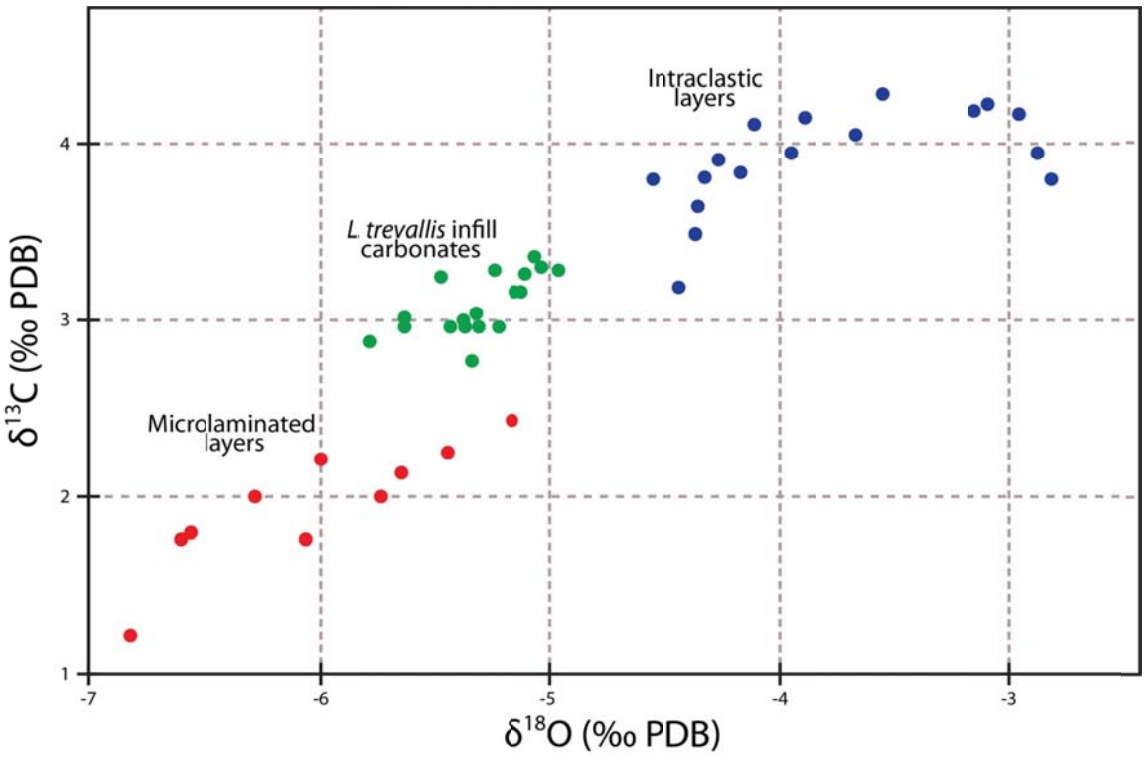

Fig. 2.9. $\delta^{13}C$ and $\delta^{18}O$ of microlaminated layers, intraclastic layers, and *Lamonte trevallis* infill carbonates.

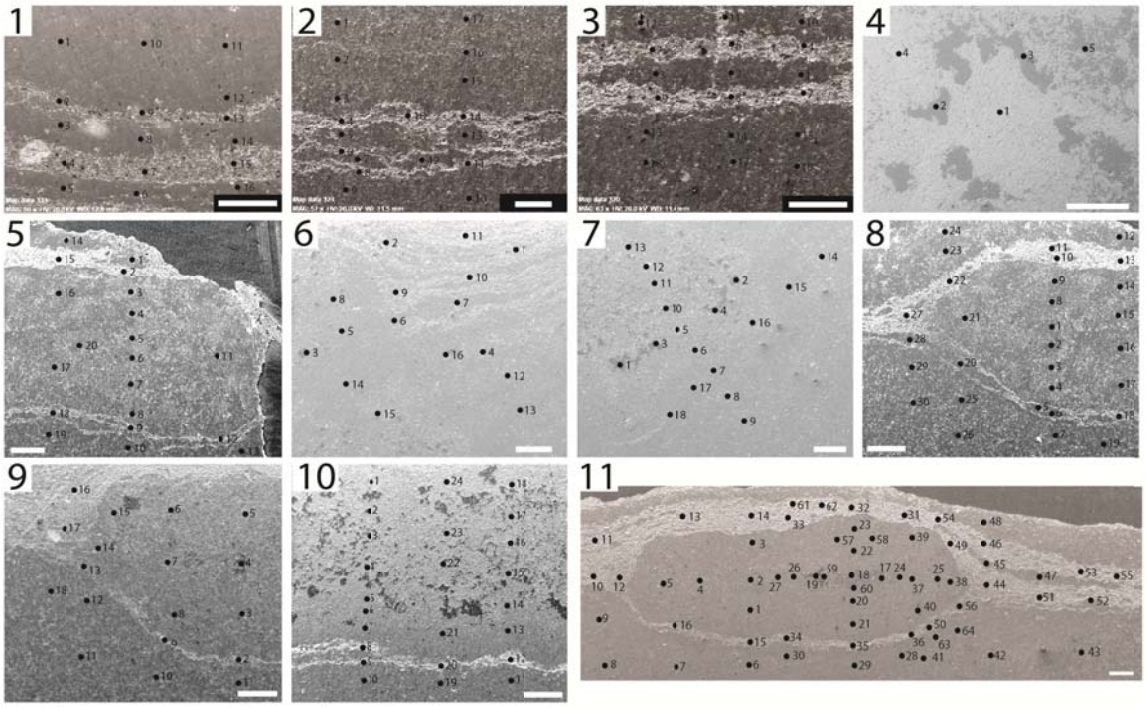

Fig. 2.10. SEM and BSE images showing locations of EDS point analyses on polished cross-sections. 1–3, 5, 9–13, and 15 are SE images, while 4, 6–8 and 14 are BSE images. Data are shown in Table 2. Scale bars = 500 μm.

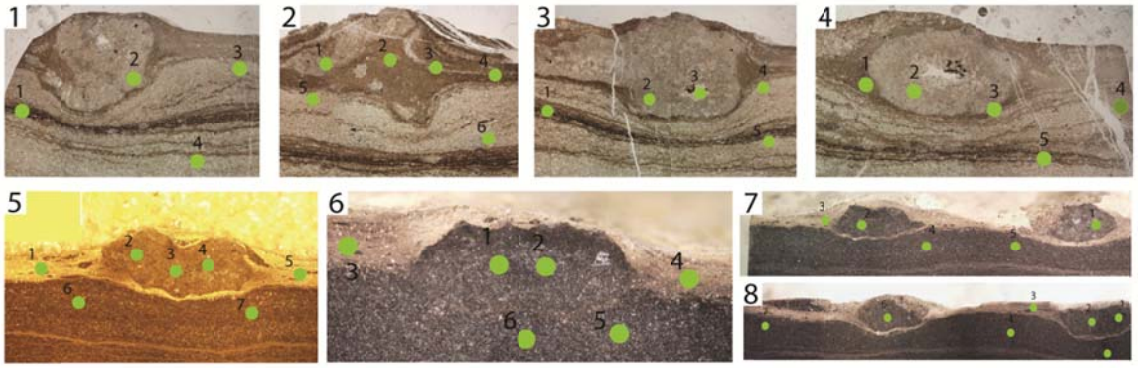

Fig. 2.11. Transmitted light (1–4) and reflected light (5–8) photomicrographs of $\delta^{13}C_{carb}$ and $\delta^{18}O_{carb}$ microsampling locations. Data are shown in Table 3.

2.12 References

Adobe Systems, Inc., 2010, Adobe Illustrator, Vers. CS5: San Jose, California.

BERTLING, M., 2007, What's in a Name? Nomenclature, Systematics, Ichnotaxonomy, *in* Miller, W., ed., Trace Fossils: Concepts, Problems, Prospects: Elsevier, Amsterdam, The Netherlands, p. 81-91.

BOTTJER, D.J., HAGADORN, J.W., and DORNBOS, S.Q., 2000, The Cambrian substrate revolution: GSA Today, v. 10, p. 1-7.

CAI, Y., HUA, H., XIAO, S., SCHIFFBAUER, J.D., and LI, P., 2010, Biostratinomy of the late Ediacaran pyritized Gaojiashan Lagerstätte from southern Shaanxi, south China: Importance of event deposits: Palaios, v. 25, p. 487-506.

CAI, Y., SCHIFFBAUER, J.D., HUA, H., and XIAO, S., 2011, Morphology and paleoecology of the late Ediacaran tubular fossil *Conotubus hemiannulatus* from the Gaojiashan Lagerstätte of southern Shaanxi Province, South China: Precambrian Research, v. 191, p. 46-57.

CAI, Y., SCHIFFBAUER, J.D., HUA, H., and XIAO, S., 2012, Preservational modes in the Ediacaran Gaojiashan Lagerstätte: Pyritization, aluminosilicification, and carbonaceous compression: Palaeogeography Palaeoclimatology Palaeoecology, v. 326-328, p. 109-117, doi: 10.1016/j.palaeo.2012.02.009.

CANFIELD, D.E., and FARQUHAR, J., 2009, Animal evolution, bioturbation, and the sulfate concentration of the oceans: Proceeding of the National Academy of Sciences of the United State of America, v. 106, p. 8123–8127.

CHEN, M., and WANG, Y., 1977, Note on the tubular metazoan fossils from the Dengying Formation of the upper Sinian System in the Gorge District of the Yangtze River: Kexue Tongbao (Chinese Science Bulletin), v. 22, p. 219-221.

CHEN, Z., 1999, Late Sinian metazoan Tubular fossils from western Hubei and Southern Shaanxi, ChinaPh.D Dissertation, Nanjing, 128 p.

CHEN, Z., BENGTSON, S., ZHOU, C., HUA, H., and YUE, Z., 2008, Tube structure and original composition of *Sinotubulites*: shelly fossils from the late Neoproterozoic in southern Shaanxi, China: Lethaia, v. 41, p. 37-45.

CHEN, Z., ZHOU, C., MEYER, M., XIANG, K., SCHIFFBAUER, J.D., YUAN, X., and XIAO, S., 2013a, Reply to Comment on "Trace fossil evidence for Ediacaran bilaterian animals with complex behaviors" [Precambrian Res. 224 (2013) 690-701]: Precambrian Research, v. xx, p. xx.

CHEN, Z., ZHOU, C., MEYER, M., XIANG, K., SCHIFFBAUER, J.D., YUAN, X., and XIAO, S., 2013b, Trace fossil evidence for Ediacaran bilaterian animals with complex behaviors: Precambrian Research, v. 224, p. 21.

CONDON, D., ZHU, M., BOWRING, S., WANG, W., YANG, A., and JIN, Y., 2005, U-Pb ages from the Neoproterozoic Doushantuo Formation, China: Science, v. 308, p. 95-98.

DESJARDINS, P.R., MANAGANO, M.G., BUATOIS, L.A., and PRATT, B.R., 2010, *Skolithos* pipe rock and associated ichnofabrics from the southern Rocky Mountains, Canada: colonization trends and environmental controls in an early Cambrian sand-sheet complex: Lethaia, v. 43, p. 507-528.

DING, L., ZHANG, L., LI, Y., and DONG, J., 1992, The Study of the Late Sinian -- Early Cambrian Biotas from the Northern Margin of the Yangtze Platform: Scientific and Technical Documents Publishing House, Beijing, 135 p.

DONG, L., XIAO, S., SHEN, B., ZHOU, C., LI, G., and YAO, J., 2009, Basal Cambrian microfossils from the Yangtze Gorges area (South China) and the Aksu area (Tarim Block, northwestern China): Journal of Paleontology, v. 83, p. 30-44.

DORNBOS, S.Q., BOTTJER, D.J., and CHEN, J.-Y., 2004, Evidence for seafloor microbial mats and associated metazoan lifestyles in Lower Cambrian phosphorites of Southwest China, v. 37, p. 127-137.

DROSER, M.L., and BOTTJER, D.J., 1986, A semiquantitative field classification of ichnofabric: Journal of Sedimentary Petrology, v. 56, p. 558-559.

DROSER, M.L., and BOTTJER, D.J., 1988, Trends in depth and extent of bioturbation in Cambrian carbonate marine environments, western United States: Geology, v. 16, p. 233-236.

DROSER, M.L., GEHLING, J.G., and JENSEN, S., 1999, When the worm turned: Concordance of Early Cambrian ichnofabric and trace-fossil record in siliciclastic rocks of South Australia: Geology, v. 27, p. 625-628.

DROSER, M.L., GEHLING, J.G., and JENSEN, S.R., 2006, Assemblage palaeoecology of the Ediacara biota: The unabridged edition?: Palaeogeography, Palaeoclimatology, Palaeoecology, v. 232, p. 131-147.

DROSER, M.L., JENSEN, S., and GEHLING, J.G., 2002, Trace fossils and substrates of the terminal Proterozoic-Cambrian transition: Implications for the record of early bilaterians and sediment mixing: Proceedings of the National Academy of Sciences, USA, v. 99, p. 12572-12576.

DZIK, J., 2005, Behavioral and anatomical unity of the earliest burrowing animals and the cause of the ‘‘Cambrian explosion’’: Paleobiology, v. 31, p. 503-521.

FEDONKIN, M.A., GEHLING, J.G., GREY, K., NARBONNE, G.M., and VICKERS-RICH, P., 2007a, The Rise of Animals: Evolution and Diversification of the Kingdom Animalia: Johns Hopkins University Press, Baltimore, 326 p.

FEDONKIN, M.A., SIMONETTA, A., and IVANTSOV, A.Y., 2007b, New data on *Kimberella*, the Vendian mollusc-like organism (White Sea region, Russia): palaeoecological and evolutionary implications, *in* Vickers-Rich, P., and Komarower, P., eds., The Rise and Fall of the Ediacaran Biota: Geological Society of London Special Publications 286, p. 157-179.

FEDONKIN, M.A., and WAGGONER, B.M., 1997, The late Precambrian fossil *Kimberella* is a mollusc-like bilaterian organism: Nature, v. 388, p. 868-871.

FIKE, D.A., GROTZINGER, J.P., PRATT, L.M., and SUMMONS, R.E., 2006, Oxidation of the Ediacaran ocean: Nature, v. 444, p. 744-747.

GEHLING, J.G., 1999, Microbial mats in terminal Proterozoic siliciclastics: Ediacaran death masks: Palaios, v. 14, p. 40-57.

GERDES, G., KLENKE, T., and NOFFKE, N., 2003, Microbial signatures in peritidal siliciclastic sediments: A catalogue: Sedimentology, v. 47, p. 279-308.

GINGRAS, M., HAGADORN, J.W., SEILACHER, A., LALONDE, S.V., PECOITS, E., PETRASH, D., and KONHAUSER, K.O., 2011, Possible evolution of mobile animals in association with microbial mats: Nature Geoscience, v. 4, p. 372-375.

HAGADORN, J.W., and BOTTJER, D.J., 1999, Restriction of a Late Neoproterozoic biotope: Suspect-microbial structures and trace fossils at the Vendian -- Cambrian transition: Palaios, v. 14, p. 73-85.

HALVERSON, G.P., WADE, B.P., HURTGEN, M.T., and BAROVICH, K.M., 2010, Neoproterozoic chemostratigraphy: Precambrian Research, v. 182, p. 337-350.
HUA, H., CHEN, Z., YUAN, X., ZHANG, L., and XIAO, S., 2005, Skeletogenesis and asexual reproduction in the earliest biomineralizing animal *Cloudina*: Geology, v. 33, p. 277-280.
HUA, H., PRATT, B.R., and ZHANG, L., 2003, Borings in *Cloudina* shells: Complex predator-prey dynamics in the terminal Neoproterozoic: Palaios, v. 18, p. 454–459.
IVANSTOV, A.Y., and MALAKHOVSKAYA, Y.E., 2002, Giant Traces of Vendian Animals: Doklady Akademii Nauk, v. 385, p. 382-386.
JENSEN, S., 2003, The Proterozoic and earliest Cambrian trace fossil record: patterns, problems and perspectives: Integrative and Comparative Biology, v. 43, p. 219-228.
JENSEN, S., DROSER, M.L., and GEHLING, J.G., 2005, Trace fossil preservation and the early evolution of animals: Palaeogeography Palaeoclimatology Palaeoecology, v. 220, p. 19-29.
JENSEN, S., DROSER, M.L., and GEHLING, J.G., 2006, A critical look at the Ediacaran trace fossil record, *in* Xiao, S., and Kaufman, A.J., eds., Neoproterozoic Geobiology: Springer, Dordrecht, the Netherlands, p. 115-157.
JENSEN, S., and RUNNEGAR, B., 2005, A complex trace fossil from the Spitskop Member (terminal Ediacaran–? Lower Cambrian) of southern Namibia: GEOLOGICAL MAGAZINE, v. 145, p. 561-569.
JENSEN, S., SAYLOR, B.Z., GEHLING, J.G., and GERMS, G.J.B., 2000, Complex trace fossils from the terminal Proterozoic of Namibia: Geology, v. 28, p. 143-146.
JIANG, G., SHI, X., ZHANG, S., WANG, Y., and XIAO, S., 2011, Stratigraphy and paleogeography of the Ediacaran Doushantuo Formation (ca. 635–551 Ma) in South China: Gondwana Research, v. 19, p. 831-849.
JIANG, G., WANG, X., SHI, X., and XIAO, S., 2012, The origin of decoupled carbonate and organic carbon isotope signatures in the early Cambrian (ca. 542-520 Ma) Yangtze platform: Earth and Planetary Science Letters, v. 317-318.
JIANG, S.-Y., PI, D.-H., HEUBECK, C., FRIMMEL, H., LIU, Y.-P., DENG, H.-L., LING, H.-F., and YANG, J.-H., 2009, Early Cambrian ocean anoxia in South China: Nature, v. 459, p. E5-E6.
KENNEDY, M., DROSER, M., MAYER, L.M., PEVEAR, D., and MROFKA, D., 2005, Late Precambrian oxygenation: inception of the clay mineral factory: Science, v. 311, p. 1446-1449.
LAFLAMME, M., SCHIFFBAUER, J.D., NARBONNE, G.M., and BRIGGS, D.G., 2011, Microbial biofilms and the preservation of the Ediacara biota: Lethaia, v. 44, p. 203-213.
MARENCO, K.N., and BOTTJER, D.J., 2008, The importance of *Planolites* in the Cambrian substrate revolution: Palaeogeography Palaeoclimatology Palaeoecology, v. 258, p. 189-199.
MARENCO, K.N., and BOTTJER, D.J., 2011, Quantifying Bioturbation in Ediacaran and Cambrian Rocks, *in* Laflamme, M., Schiffbauer, J.D., and Dornbos, S.Q., eds., Quantifying the Evolution of Early Life: Elseiver, New York, p. 20.

MARENCO, P.J., CORSETTI, F.A., HAMMOND, D.E., KAUFMAN, A.J., and BOTTJER, D.J., 2008, Oxidation of pyrite during extraction of carbonate associated sulfate: Chemical Geology, v. in press.

MCFADDEN, K.A., HUANG, J., CHU, X., JIANG, G., KAUFMAN, A.J., ZHOU, C., YUAN, X., and XIAO, S., 2008, Pulsed oxygenation and biological evolution in the Ediacaran Doushantuo Formation: Proceedings of the National Academy of Sciences, USA, v. 105, p. 3197–3202.

MEYER, M., SCHIFFBAUER, J.D., XIAO, S., CAI, Y., and HUA, H., 2012, Taphonomy of the upper Ediacaran enigmatic ribbonlike fossil *Shaanxilithes*: Palaios, v. 27, p. 354-372, doi: 10.2110/palo.2011.p11-098r.

MILLER, W., 2007, Trace fossils: concepts, problems, prospects: Elsevier, Amsterdam, 611 p.

NOFFKE, N., 2008, Turbulent lifestyle: Microbial mats on Earth's sandy beaches -- today and 3 billion years ago: GSA Today, v. 18(10), p. 4-9.

PEMBERTON, S.G., and FREY, R.W., 1982, Trace fossil nomenclature and the *Planolites-Palaeophycus* dilemma: Journal of Paleontology, v. 56, p. 843-881.

RETALLACK, G.J., 2013, Comment on "Trace fossil evidence for Ediacaran bilaterian animals with complex behaviors" by Chen et al. [Precambrian Res. 224 (2013) 690-701]: Precambrian Research, v. xx, p. xx.

SCHIEBER, J., BOSE, P., ERIKKSON, P., BANERJEE, S., SARKAR, S., ALTERMANN, W., and CATUNEANU, O., 2007, Atlas of Microbial Mat Features Preserved within the Siliciclastic Rock Record: Elsvier, Amsterdam, 324 p.

SCHNEIDER, C.A., RASBAND, W.S., and ELICEIRI, K.W., 2012, NIH Image to ImageJ: 25 years of image analysis: Nature Methods, v. 9, p. 4.

SEILACHER, A., 1999, Biomat-related lifestyles in the Precambrian: Palaios, v. 14, p. 86-93.

SEILACHER, A., 2007, Trace Fossil Analysis, p. 226.

SEILACHER, A., BUATOIS, L.A., and MÁNGANO, M.G., 2005, Trace fossils in the Ediacaran–Cambrian transition: Behavioral diversification, ecological turnover and environmental shift: Palaeogeography, Palaeoclimatology, Palaeoecology, v. 227, p. 323-356.

SHEN, B., XIAO, S., ZHOU, C., and YUAN, X., 2009, *Yangtziramulus zhangi* new genus and species, a carbonate-hosted macrofossil from the Ediacaran Dengying Formation in the Yangtze Gorges area, South China: Journal of Paleontology, v. 83, p. 575-587.

SHEN, Y., ZHANG, T., and HOFFMAN, P.F., 2008, On the co-evolution of Ediacaran oceans and animals: Proceeding of the National Academy of Sciences of the United State of America, v. 105, p. 7376–7381.

SKINNER, E.S., 2005, Taphonomy and depositional circumstances of exceptionally preserved fossils from the Kinzers Formation (Cambrian), southeastern Pennsylvania: Palaeogeography, Palaeoclimatology, Palaeoecology, v. 220, p. 167-192.

SUN, W., 1986, Late Precambrian pennatulids (sea pens) from the eastern Yangtze Gorge, China: *Paracharnia* gen. nov.: Precambrian Research, v. 31, p. 361-375.

WEBER, B., STEINER, M., and ZHU, M.Y., 2007, Precambrian Cambrian trace fossils from the Yangtze Platform (South China) and the early evolution of bilaterian lifestyles: Palaeogeography Palaeoclimatology Palaeoecology, v. 254, p. 328-349.

XIAO, S., SCHIFFBAUER, J.D., MCFADDEN, K.A., and HUNTER, J., 2010, Petrographic and SIMS pyrite sulfur isotope analyses of Ediacaran chert nodules: Implications for microbial processes in pyrite rim formation, silicification, and exceptional fossil preservation: Earth and Planetary Science Letters, v. 297, p. 481-495.

XIAO, S., SHEN, B., ZHOU, C., XIE, G., and YUAN, X., 2005, A uniquely preserved Ediacaran fossil with direct evidence for a quilted bodyplan: Proceedings of the National Academy of Sciences, USA, v. 102, p. 10227-10232.

ZHAO, Z., XING, Y., DING, Q., LIU, G., ZHAO, Y., ZHANG, S., MENG, X., YIN, C., NING, B., and HAN, P., 1988, The Sinian System of Hubei: China University of Geosciences Press, Wuhan, 205 p.

ZHU, R.X., LI, X.H., HOU, X.G., PAN, Y.X., WANG, F., DENG, C.L., and HE, H.Y., 2009, SIMS U–Pb zircon age of a tuff layer in the Meishucun section, Yunnan, southwest China: Constraint on the age of the Precambrian–Cambrian boundary: Science, v. 39, p. 1105-1111.

CHAPTER 3

TAPHONOMY OF THE LATE EDIACARAN ENIGMATIC RIBBON-LIKE FOSSIL *SHAANXILITHES*

MIKE MEYER[1], JAMES D. SCHIFFBAUER[2], SHUHAI XIAO[1], YAOPING CAI[3], HONG HUA[3]

[1]*Department of Geosciences, Virginia Polytechnic Institute and State University, Blacksburg, VA 24061, USA*

[2]*Department of Geosciences, University of Missouri, Columbia, MO, 65211, USA*

[3]*State Key Laboratory of Continental Dynamics, and Department of Geology, Northwest University, Xi'an, 710069, China*

3.1 Abstract

Shaanxilithes ningqiangensis is an enigmatic ribbon-shaped fossil from the late Ediacaran Gaojiashan Member of the Dengying Formation, southern Shaanxi Province, South China. This taxon has also been reported from Ediacaran successions in North China and possibly in southeastern Siberia, making it a potential index fossil for inter-regional biostratigraphic correlation of upper Ediacaran successions. At Gaojiashan, *Shaanxilithes ningqiangensis* is often preserved along bedding planes of phosphate-rich silty and calcareous shale, with no evidence of vertical intrusion into adjacent beds and containing little to no carbonaceous material. Here, through detailed microstructural and microchemical investigation using a combination of analytical techniques, taphonomic details of *Shaanxilithes ningqiangensis* and potentially related forms are revealed, showing that these enigmatic fossils are preserved as clay molds in the surrounding matrix. Together with other taphonomic features, such as abruptly bent ribbons, overlapping but not cross-cutting ribbons, and co-occurring discoidal structures interpreted as disarticulated sections of the original organism, the new data suggest that *Shaanxilithes ningqiangensis* is a body fossil consisting of serially arranged units that are discoidal, lensoidal, or crescentic in shape. *Shaanxilithes ningqiangensis* is not a trace fossil as some previous researchers have suggested.

3.2 Introduction

Fossils of the Ediacaran Period (ca. 635–542 Ma) are widely known for their enigmatic nature, both phylogenetically and taphonomically. Some of the better-known examples from a range of Ediacaran taphonomic windows include the classic macrofossil

representatives of Ediacara-type death-mask preservation captured in coarse-grained siliciclastic rocks in Newfoundland, the White Sea Region (Russia), South Australia, and Namibia (Gehling, 1999; Narbonne, 2005; Xiao and Laflamme, 2009), the three-dimensionally phosphatized and cellularly preserved microfossils of the Doushantuo phosphorites (Xiao and Knoll, 2000), and the macroalgal carbonaceous compressions within the Doushantuo and Lantian black shale successions (Xiao et al., 2002; Yuan et al., 2011b). While these fossils provide an extraordinary opportunity to investigate the Ediacaran biosphere, their biological and taphonomic interpretations are often complicated, not least because they are frequently stem representatives of living clades (Narbonne, 2004; Xiao and Laflamme, 2009) and their preservation often involves non-actualistic processes (Gehling, 1999; Narbonne, 2005; Liu et al., 2011).

Recent analyses, using a combination of petrographic and microchemical tools, have allowed critical assessment of the affinities and taphonomy of many Ediacaran fossils. For example, it has been shown that many Ediacaran trace fossils may actually be body fossils (Droser et al., 2005; Jensen et al., 2006; Cai et al., 2011; Sappenfield et al., 2011) and that associations with clay minerals and pyrite may be important and recurrent factors in multiple Ediacaran taphonomic windows (Anderson et al., 2011; Laflamme et al., 2011b; Cai et al., 2012). Indeed, numerous studies have focused on the potential taphonomic role of authigenic clay minerals in exceptional preservation (the preservation or replication of non-biomineralized tissues), particularly in carbonaceous compressions (widely referred to as Burgess Shale-type [BST]) preservation in early Phanerozoic marine deposits (Butterfield, 1990; 1995; Orr et al., 1998; Gaines et al., 2005; Zhu et al., 2005; Butterfield et al., 2007; Gaines et al., 2008; Page et al., 2008). Hypotheses for the

association of clay minerals with BST preservation place varying levels of influence on their potential role in the preservation of soft tissue. Some hypotheses invoke active involvement of authigenic or detrital clay minerals in impeding organic decomposition and facilitating replication, pointing to physical or chemical affinities between clay minerals and organic molecules—a view that finds some support from experimental taphonomic studies (Martin et al., 2004; Darroch et al., 2012). For instance, Orr et al. (1998) argued that authigenic clay minerals adsorbed on soft tissues serve as physical templates to facilitate replication, Butterfield (1995) proposed that detrital clay minerals bind to enzymes to slow down autolytic decay of soft tissues, and Petrovich (2001) suggested that nucleation of Fe-rich clay minerals on Fe^{2+} adsorbed on soft tissues could delay degradation and promote preservation. Other hypotheses alternatively advocate that clay mineral association with carbonaceous compressions is incidental and results from metamorphic mineralization, thus implying that clay minerals do not play a constructive role in the preservation of soft tissues (Butterfield et al., 2007; Gaines et al., 2008; Page et al., 2008). To further examine the potential taphonomic importance of clay mineral associations in soft tissue preservation, we investigated the enigmatic ribbon-like fossil *Shaanxilithes ningqiangensis* and other potentially related forms (such as imbricated or meniscate forms as well as disarticulated discoidal or lensoidal structures) from the late Ediacaran Gaojiashan Lagerstätte of southern Shaanxi Province, South China. From previous descriptions, these fossils are typically preserved as compressions but with very little organic remains (Cai et al., 2010; Cai and Hua, 2011). Available data indicate that *Shaanxilithes* and *Shaanxilithes*-like fossils have a restricted stratigraphic distribution in late Ediacaran rocks (ca. 551–542 Ma) but a wide geographic distribution in South China

(Hua et al., 2004; Cai et al., 2010), North China (Shen et al., 2007), Chaidam of northwestern China (Shen et al., 2007), and probably southeastern Siberia (Zhuravlev et al., 2009; Cai and Hua, 2011), indicating the potential of *Shaanxilithes* as an index fossil for inter-regional correlation of late Ediacaran successions.

3.3 Geological and Stratigraphic Background

Samples were collected from the type locality of the Gaojiashan Lagerstätte near the village of Gaojiashan, Ningqiang County, southern Shaanxi Province, South China (Lin et al., 1986; Zhang, 1986). The Ediacaran Dengying Formation (ca. 551–542 Ma) at this locality consists of three units (Fig. 3.1), in ascending order: the Algal Dolomite, Gaojiashan, and Beiwan members, which are likely equivalent to the Hamajing, Shibantan, and Baimatuo members of the Dengying Formation in the well-known Yangtze Gorges area (Shen et al., 2007; Zhou and Xiao, 2007; Cai et al., 2010). The Algal Dolomite Member is a light gray peritidal dolostone with dissolution structures filled with isopachous and botryoidal quartz cements. The subtidal Gaojiashan Member is characterized by thinly bedded calcareous siltstone and mudstone with minor limestone beds and a thick capping sandstone unit. The middle Gaojiashan Member hosts most of the fossils, typically preserved in the siltstone layers of event-deposit siltstone-mudstone couplets (Cai et al., 2010). The Beiwan Member consists of light gray, thick-bedded, peritidal dolostone and contains abundant dissolution voids filled with pyrobitumen.

The genus *Shaanxilithes* includes the type species *S. ningqiangensis* (Xing et al., 1984) and only one other published species *S. erodus* (Zhang, 1986), which is likely a junior synonym of *S. ningqiangensis* (Shen et al., 2007). It was first described from the

Gaojiashan Member at the Lijiagou and Shizhonggou sections of Ningqiang, southern Shaanxi (Xing et al., 1984). The *S. ningqiangensis* specimens collected and analyzed here (hereafter referred to as *Shaanxilithes* for simplicity), occur abundantly on multiple bedding surfaces within an interval of greenish-gray silty shale (Fig. 3.1B–C) of the lower Gaojiashan Member in this region (Cai et al., 2010). Field observations at the type section (Fig. 3.1C) show the occurrence of *Shaanxilithes* in several horizons from 12–16 m above the base of the Gaojiashan Member.

3.4 Materials and Methods

Our specimens were collected from a gray phosphate-rich silty shale interval approximately 14–15 m above the base of the Gaojiashan Member at the Gaojiashan section (Fig. 3.1B), including both *Shaanxilithes* ribbons (Fig. 3.2A–F) and co-occurring discoidal structures (Fig. 2G–H). Despite the abundance of discoidal structures found at the Gaojiashan section, they have not been previously described in the literature (see description in systematic paleontology section below). As discussed here, their potential relationship to the typically ribbon-like *Shaanxilithes* fossils may provide morphological and taphonomic clues to aid in resolving the body vs. trace fossil controversy surrounding *Shaanxilithes*. The specimens are reposited at the Virginia Polytechnic Institute Geosciences Museum under the catalog number VPIGM-4621 to VPIGM-4638.

Hand samples with *Shaanxilithes* ribbons and discoidal structures were examined under reflected light microscopy. Partially exposed ribbons (i.e., part of the ribbon is exposed but the rest is imbedded in matrix) were thin sectioned and examined under petrographic microscopy (Fig. 3.2K–M). Further, polished thin sections and slabs cut

perpendicular to bedding planes and freshly exposed specimens on bedding surface were sputter coated with ~5–7.5 nm Au-Pd in preparation for electron microscopy (Fig. 3.3–6). Some discoidal structures are preserved somewhat three dimensionally, with a biconvex lensoidal shape. A few of these lensoidal structures were physically detached from the rock matrix and then examined under electron microscopy (Figs. 3.7–8), either directly on disc surface or on cut surfaces perpendicular to the disc surface.

Electron microscopic analyses were conducted using an FEI Quanta 600 field emission environmental scanning electron microscope (ESEM) in high vacuum mode using secondary (topographic) and backscattered (atomic number contrast) electron detectors. Energy dispersive X-ray spectroscopic (EDS) point spectra and elemental maps (of fossils on unpolished bedding surfaces and in polished cross-sections) were generated using an integrated Bruker AXS QUANTAX 400 with a high-speed silicon drift detector. Identical operating conditions were maintained for all EDS analyses: 20 keV accelerating voltage, 5.0 spot size (a unitless measure of beam current and probe diameter), 11.5 mm working distance, and X-ray signal count-rates between 25–35 kcps. All elemental maps were acquired for 600 seconds live-time, and individual point spectra were collected for 100 seconds live-time. Elemental peaks from point spectra were identified and quantified (with zaf and Au-Pd coating corrections applied) using the Bruker Esprit 1.9.2 software.

Initial X-ray point spectra were collected from the host rock matrix, *Shaanxilithes* ribbons, and associated discoidal structures (Table 3.1). Elemental maps were subsequently generated (Figs. 3.3–8) for all elements found at >1% (normalized weight percentage; nwp) in point analysis. While topography of unpolished specimens can significantly affect EDS analysis and elemental mapping, it is clear from our analyses

here that elemental signal trends observed in the elemental maps generally do not match specimen topography from secondary electron imaging, suggesting that observed elemental distributions are not topographic artifacts. In addition, EDS point analyses of unpolished specimens on bedding surfaces were carefully placed in locally flat surfaces of the specimens to minimize topographic irregularities that may obscure X-ray signal. EDS point data from unpolished specimens are broadly consistent with those from polished specimens (Table 3.1; see below), supporting the reliability of the EDS data and elemental maps.

To assist in mineral identification, fossil and matrix material were also analyzed using Raman spectroscopy (Fig. 3.9). A total of 15 polished and unpolished samples were analyzed via laser Raman microspectroscopy, using a JY Horiba HR 800 UV Spectrometer with a 244 nm laser (15 mW) with a 2400 gr/mm grating and a Symphony CCD detection system (LN2 cooled, 2048 x 512 pixel). The sampling time was 300 seconds/scan using a 40× UV objective (4 μm spot size). Raman spectra were baseline corrected using Labspec software.

3.5 Results

The analyzed *Shaanxilithes* ribbons are 9.9–95.0 mm in length and 0.8–7.8 mm in width (Fig. 3.10), with sub-millimetrically spaced annulations (spacing distance = 0.16–0.20 mm). As there are no definitive holdfasts or distinct terminations identified in *Shaanxilithes* ribbons, the measured lengths likely underestimate the original ribbon length and maximum widths were assessed at the midpoint of the preserved length. *Shaanxilithes* shows no evidence of branching or cross-cutting; instead, densely

accumulated specimens curve (Fig. 3.2E, J), abruptly bend (Fig. 3.2C–D), and overlap (Fig. 3.2A–B, F, J). The overlapping specimens are separated by an extremely thin layer of matrix material (Fig. 3.2F). In addition, some specimens are seemingly disarticulated into isolated (Figs. 3.2G–H, 3A, 7, and 8) or overlapping (Fig. 3.2D) discs, resembling a fallen stack of coins. In one case, a partially disarticulated specimen was observed with disjointed discs oriented perpendicular to the bedding plane (Fig. 3.2K) rather than lying prone to bedding as usually seen with disconnected and isolated discoidal structures (Figs. 3.2H, 3A, 7–8). The average diameter of the isolated discs (1.28 mm) is smaller than the average width of co-occurring ribbons (2.02 mm), with a mean ratio of 1:1.58 (Fig. 3.10). Incidentally, this ratio is comparable to the expected ratio between the diameter of a cylinder and the width of a ribbon resulting from inelastic lateral compression of the same cylinder ($\pi d/2$, or a ratio of 1:1.57), indicating that *Shaanxilithes* ribbons and associated discs might be related. We note that, whereas collapse of soft-bodied organisms sometimes produces a two-dimensional "shallow" of the original organisms, compaction can generate a "foot-print" larger than original organisms (e.g., compressed acritarchs and siphonous green algae).

EDS spectral data of bedding surfaces and cross-sections indicate that the major elemental constituents of the host lithology are (in mean nwp): O=39.0%, Ca=22.3%, Si=15.3%, P=7.3%, Al=4.4%, K=3.8%, Fe=2.6%, Mg=1.9%, and C=1.6% (Table 1). Minor constituents, ~0.5% total combined nwp, include S, Ti, and Na. As expected of siliciclastic sediments, O and Si are the most abundant components of the host rock matrix, and minor dolomitic cements (as shown by Ca and Mg localization) are also present in the host lithology. Highly localized concentrations of P (in some locations up

to ~20% nwp) were unanticipated, corresponding to previously undescribed sub-millimetric phosphatic grains.

Mean weight percentages from combined EDS point spectra of *Shaanxilithes* ribbons and discoidal structures (Table 3.1) show a compositional departure from the host rock matrix as described above. *Shaanxilithes* ribbons exhibit higher levels of Si, Al, K, C, Fe, and Ti than the surrounding host rock matrix, but lower fractions of Ca and P. The discoidal structures show a similar pattern, although the distinction in Si, K, Ca, and P concentrations from the matrix is not significant (Table 3.1).

Confirming the EDS point analysis, elemental mapping shows that both *Shaanxilithes* ribbons and discoidal structures on bedding surfaces are characterized by higher concentrations of Si, Al, and K, but lower concentrations of Ca and P, relative to the matrix (Figs. 3.3–4, 7–8). In polished section perpendicular to bedding plane, *Shaanxilithes* is visible as compressed ribbons consisting of multiple Al-rich and Al-poor layers (Figs. 3.4–6). In one specimen, EDS point analysis (Table 3.2) and elemental mapping (Fig. 3.6B, D) reveal a central layer with lower C but higher Si, Al, K, and Mg contents. This central layer is surrounded by two outer layers with higher C and S contents (probably organic carbon), which are further surrounded by two Al-rich layers that appear to be continuous with the matrix. In other specimens (Figs. 3.4C–D, 4F, 5), there appear to be two Al-rich layers separated by a gap along which the *Shaanxilithes* ribbons can be split into composite part and counterparts. A few *Shaanxilithes* ribbons in cross section show the presence of S and/or Fe (Figs. 3.4E–F, 5D, 6D), representing pyrite or its weathering product. Elemental maps of three-dimensionally preserved discoidal structures clearly show that the discoidal surface is enveloped by a layer rich in

Al, Si, and K, but poor in Ca and P (Fig. 3.7–8). This is clearly seen in elemental maps of cross sections cut perpendicular to the discoidal structures (Fig. 3.8E).

While surface roughness in unpolished specimens inevitably causes EDS take-off angle variation and therefore topographically-induced aberrances in EDS point spectra and elemental maps, we argue that the observed microchemical variations between fossils and matrix are not topographic artifacts. First, patterns observed in the elemental maps do not match topographic variations. Second, the elemental distinction between fossils and matrix is confirmed on polished cross sections (Figs. 3.3–8) where topographic effect is minimized. Third, a comparison between unpolished and polished rock matrix shows that differences in average elemental compositions are relatively small (Table 3.1). The minimal impact of surface roughness in rock matrix EDS analyses may be, at least in part, a result of the fine grain size producing relatively smooth surfaces.

The layered structure of the *Shaanxilithes* ribbons, however, does contribute to the observed variation in EDS point analyses of the ribbons, particularly when the ribbons are highly compressed. As expected, because the layers are compositionally different (Figs. 3.4F, 5C−D, 6D–E, and Table 3.2), EDS spectra of vertical cross sections of *Shaanxilithes* ribbons are highly sensitive to the positioning of analytical spots. Thus, compared to the matrix, differences in average elemental concentrations between unpolished (bedding surface) and polished (thin-sectioned) *Shaanxilithes* ribbons are greater for most elements (Table 3.1).

Raman spectral analysis (Fig. 3.9) showed differences between *Shaanxilithes* ribbons, discs, and matrix. Discs and ribbons exhibit peaks at ~600, ~700, ~1600, and ~3620 cm^{-1}. One ribbon spectrum shows a strong peak at ~1096 cm^{-1}. Matrix spectra all

have peaks around ~1600 and ~3620 cm^{-1}, but some show peaks at ~700, ~961 and ~1096 cm^{-1}. The peak at ~600 cm^{-1} matches the signature of rutile (Balachandran and Eror, 1982; Parker and Siegel, 1990; Mazza et al., 2007); the peak at ~700 cm^{-1} matches the signal of many phyllosilicate minerals (Wada and Kamitakahara, 1991; McKeown et al., 1999; Wang et al., 2002); and the prominent peak around ~3620 cm^{-1} may be related to the OH groups in phyllosilicate minerals (Wang et al., 2002). The peak seen at ~1600 cm^{-1} may be due to kerogen, particularly when accompanied by a peak around ~1350 cm^{-1} (as in several disc and ribbon spectra) (Wopenka and Pasteris, 1993; Schopf et al., 2005). The peaks at ~1096 and ~961 cm^{-1} likely result from the presence of dolomite and apatite, respectively, mainly in the matrix (although a dolomite signal is also present in one ribbon spectrum) (Nicola et al., 1976; Awonusi et al., 2007).

3.6 Discussion

3.6.1 Clay Association

Shaanxilithes ribbons and discoidal structures are easily identifiable on bedding surfaces (Figs. 3.2−3) due to the distinction in color and grain sizes, with the fossils replicated by finer-grained and typically lighter-colored sediments than found in the surrounding matrix. There are also compositional differences, with fossils exhibiting elevated localization of Al, Si, and K and the host rock matrix showing higher concentrations of P and Ca (Figs. 3.3–8). The co-occurrence of Al, Si, and K in conjunction with the finer grain texture are indicative of clay minerals or their diagenetic derivatives (Orr et al., 1998), and signifies a clay mineral association for both the *Shaanxilithes* ribbons and discoidal structures. Raman spectra show that peaks (i.e., ~700

cm^{-1} and ~3620 cm^{-1} peaks; Wang et al., 2002) characteristic of certain clay minerals are present in both fossils and matrix, but these peaks are consistently present in all fossils, which (with one exception) do not show peaks characteristic of dolomite and apatite. Together, the EDS and Raman data are consistent with the preferential presence of clay minerals in association of fossils.

While it is likely that clay minerals in association with *Shaanxilithes* ribbons and discoidal structures could have been altered in late diagenesis or low grade metamorphism, we suggest that the initial formation of clay precursors preferentially in association with fossils may have occurred in life (e.g., agglutination) or during early diagenesis, and that the clay association is not a *de novo* result of late diagenesis or metamorphism (Page et al., 2008). Our argument is based on the following observations. First, although clay minerals are ubiquitously present in the host rock, they are distinctively concentrated on *Shaanxilithes* ribbons and discoidal structures (Figs. 3.2–8). The spatial configuration of clay layers relative to fossil ribbons and discs are clearly shown in elemental maps of sections or slabs cut perpendicular to bedding surfaces. These clay layers either define compressed *Shaanxilithes* ribbons or wrap around three-dimensionally preserved discoidal structures; they do not follow veins or other conduits for diagenetic or metamorphic fluids (Butterfield et al., 2007). Secondly, it appears that taphonomic association with clay minerals is characteristic of *Shaanxilithes* and related discoidal structures in the lower Gaojiashan Member, but not a dominant taphonomic mode for *Conotubus* and *Gaojiashania* in the middle-upper Gaojiashan Member (Cai et al., 2010; Cai et al., 2012). In other words, this taphonomic mode preferentially occurs in certain taxa and in certain stratigraphic horizons. Three taphonomic modes—pyritization,

aluminosilicification or association with clay minerals, and carbonaceous compression—have been reported in the Gaojiashan biota (Cai et al., in press). Although some *Shaanxilithes* ribbons show distinct organic C layers (Figs. 3.4F, 6D), most *Shaanxilithes* and related discoidal fossils from the lower Gaojiashan Member are preferentially preserved through aluminosilicification with little or no organic carbon. This is in sharp contrast to the predominance of pervasively and three-dimensionally pyritized *Conotubus* and *Gaojiashania* fossils in the middle-upper Gaojiashan Member (Cai et al., 2010), hence the stratigraphic and taxonomic preference of aluminosilicification within the Gaojiashan Member is unlikely due to metamorphic differences. Finally, clays are also found in association with *Shaanxilithes*-like fossils in Ediacaran rocks of North China and Chaidam (Shen et al., 2007; Dong et al., 2009), despite distinct metamorphic histories from the Gaojiashan section in the South China Block. Thus, we infer that the clay minerals in association with *Shaanxilithes* and related discoidal fossils are unlikely a *de novo* metamorphic product.

We cannot distinguish whether the clay minerals associated with *Shaanxilithes* ribbons and discoidal structures were formed as agglutinated particles (Shen et al., 2007; Dong et al., 2009) or as authigenic products. The clay envelope surrounding three-dimensionally preserved discoidal structures (Figs. 3.7–8) is consistent with both hypotheses. At the present, we regard that the clay association was formed either in life or during early diagenesis. Regardless of the validity of the agglutination interpretation, however, clay minerals likely formed a physical template (or skeleton) that enhanced the preservation of *Shaanxilithes* and associated discoidal structures as clay molds, and

undoubtedly facilitated fossil identification in electron and optical microscopy (Figs. 3.2–8).

Thus, *Shaanxilithes* joins a group of other exceptionally preserved fossils where clay minerals may have facilitated preservation and distinction from the rock matrix, including *Chuaria* from the Ediacaran Doushantuo Formation in Hubei Province of South China, *Aspidella* from the Ediacaran Fermeuse Formation in Newfoundland of Canada, and Cambrian fossils from the Burgess Shale biota in British Columbia of Canada, Kaili biota in Guizhou Province of South China, and Chengjiang biota in Yunnan Province of South China (Orr et al., 1998; Butterfield, 2003; Gabbott et al., 2004; Zhu et al., 2005; Lin and Briggs, 2010; Anderson et al., 2011; Laflamme et al., 2011b). *Shaanxilithes* ribbons and related discoidal fossils differ from Burgess Shale-type fossils, but are similar to Fermeuse *Aspidella* fossils, in their lack of organic carbon in most specimens. This may be related to the low organic content of the original organism (e.g., agglutinated "test"; Shen et al., 2007), excessive bacterially-mediated degradation, or loss of organic carbon due to weathering or metamorphism (Lin and Briggs, 2010).

In the Ediacaran Fermeuse Formation, Laflamme et al. (2011) reported a marked contrast in grain size and composition between fine-grained clay-rich envelopes surrounding *Aspidella* holdfasts and the coarser-grained quartz-rich host rock matrix. A similar pattern is observed here with *Shaanxilithes* ribbons and discoidal fossils, which are also composed of, or replicated by, fine-grained clay-rich material (Figs. 3.3–8). In comparison to *Shaanxilithes* fossils, the surrounding matrix is a coarser-grained and much more heterogeneous silty-shale with sub-millimetric grains of dolomite and phosphate minerals.

3.6.2 Possible Pyrite Association

Although its consistency varies from specimen to specimen, the concentration of Fe and/or S in association with some *Shaanxilithes* ribbons (Figs. 3.4E–F, 5D, 6D) indicates a possible (but minor) role of pyritization and bacterial sulfate reduction in the lower Gaojiashan Member, as compared to the middle-upper Gaojiashan Member where pervasive three-dimensional pyritization is a common mode of fossil preservation (Cai et al., 2010; Cai et al., 2012). Brown lines around some specimens are iron oxide rims that are found around poorly preserved specimens such as those seen in Figs. 3.2E and 3.2J. Bacterial sulfate reduction and pyritization may also be directly or indirectly linked to numerous Ediacaran and early Phanerozoic taphonomic modes, including BST carbonaceous compression, silicification in chert nodules, Ediacara-type death mask preservation, and clay-associated preservation of *Aspidella* (Gehling, 1999; Xiao et al., 2010b; Anderson et al., 2011; Laflamme et al., 2011b; Cai et al., 2012). The localized distributions of pyrite (≤70 μm in size) identified near or surrounding some *Shaanxilithes* specimens suggests that pyrite formation was curtailed during early authigenesis. Unlike the pervasive pyritization of Gaojiashan fossils such as *Conotubus*, which led to three-dimensional pyritization (Cai et al., 2011; 2012), an early interruption of pyritization allowed the preservation of *Shaanxilithes* as two-dimensional compressions. Due to the small number of specimens with pyrite association observed in this study, we cannot determine whether pyrite precipitation played any constructive role in *Shaanxilithes* preservation. It is possible, however, that rare *Shaanxilithes* ribbons share some aspects of taphonomy with compression fossils in the Chengjiang (Gabbott et al., 2004) and

Fezouata biotas (Van Roy et al., 2010), where association with pyrite is more common than in the Gaojiashan biota analyzed in this study.

In summary, our analysis of *Shaanxilithes* and related discoidal structures build support for the hypothesis that some sort of mineralization or stabilization processes (e.g., aluminosilicification, pyritization, kerogenization, silicification, and phosphatization) are a key step to the exceptional preservation of soft-bodied tissues (Briggs, 2003).

3.6.3 Body vs. Trace Fossil Affinity

While it has been debated whether the preserved morphology of *Shaanxilithes* is indicative of a trace or body fossil (Shen et al., 2007; Weber et al., 2007; Zhuravlev et al., 2009; Cai and Hua, 2011), the fact that *Shaanxilithes* ribbons share taphonomic characteristics and a consistent size relation with the discoidal structures may present the most significant evidence that these are indeed body fossils. The observation that the mean width of compressed *Shaanxilithes* ribbons is 1.58× the mean diameter of the discoidal structures in the Gaojiashan Member suggests that the discoidal structures could represent disarticulated segments of *Shaanxilithes*. We speculate that the original organism may have been constructed of stacked discoidal, lensoidal, or meniscate segments (Fig. 3.11), possibly within a cylindrical sheath with transverse annulations. The traditional ribbon-like *Shaanxilithes* morphology is a result of compression. This reconstruction is supported by partial disarticulation of some *Shaanxilithes* ribbons, which results in chains of overlapping/imbricated discoidal, lensoidal, or crescentic segments (Fig. 3.2D, 2K, 4A, 7-8).

If the Gaojiashan discoidal structures are disarticulated segments of *Shaanxilithes*, then *Shaanxilithes* must be a body fossil rather than a trace fossil as other workers have previously suggested (Yang and Zheng, 1985; Weber et al., 2007). The absence of *Shaanxilithes* ribbons that cross-cut each other (Fig. 3.2A–B, F, J), despite their dense accumulation, also argues against a trace fossil interpretation. Finally, the occurrence of abruptly bent (Fig. 3.2C–D), twisted, and folded ribbons (*Taenioichnus zhengmuguanensis* in Yang and Zheng, 1985; regarded as synonym of *Shaanxilithes* by Shen et al., 2007) further support a body fossil interpretation for *Shaanxilithes*.

Our reconstruction of *Shaanxilithes* indicates that it consists of serially arranged modules, a body construction that is characteristic of many fossils in the late Ediacaran Period. In addition to *Shaanxilithes* described here, several other Ediacaran organisms were also constructed by the repetition of relatively simple spheroidal, discoidal, and meniscate units. These include *Palaeopascichnus* and associated body fossils (Shen et al., 2007), *Orbisiana* fossils (Jensen, 2003; Yuan et al., 2011b), as well as *Horodyskia*-like fossils described from the late Ediacaran Liuchapo Formation of South China (Dong et al., 2008). Indeed, *Funisia dorothea* from the Ediacara Member of South Australia (Droser and Gehling, 2008) may also consist of serially arranged discoidal units. These fossils, together with a large assemblage of Ediacaran fossils consisting of biserially and radially arranged tubular or fractal modules (Seilacher, 1992; Narbonne, 2004), indicate that modular construction is a common strategy adopted by Ediacaran organisms to build macroscopic and seemingly complex body plans with sufficient surface area to support osmotrophy (Laflamme et al., 2009; Sperling et al., 2011).

3.9 Conclusions

Shaanxilithes ningqiangensis and related discoidal structures are shown to be associated with clay minerals, and rarely with pyrite, in a silty, calcareous, and phosphate-rich matrix—a style of preservation sharing some similarities with Fermeuse-type preservation (Laflamme et al., 2011b) and Burgess Shale-type preservation (Butterfield, 1995; Orr et al., 1998; Orr et al., 2002; Zhu et al., 2005). It is unlikely that the clay association was formed *de novo* during metamorphism. Rather, clay precursors likely existed in life or during authigenesis, and may have facilitated the preservation of *Shaanxilithes ningqiangensis*. Abruptly bent ribbons, overlapping but not cross-cutting ribbons, and a probable relationship with disarticulated discoidal, lensoidal, or meniscate modules suggest that *Shaanxilithes ningqiangensis* likely represents an enigmatic body fossil constructed of serially arranged units.

3.10 Systematic Paleontology

As with many Ediacaran organisms, the phylogenetic affinity of *Shaanxilithes ningqiangensis* is unresolved. While the goal of this report is not to determine the phylogenetic affinity of *S. ningqiangensis*, this section aims to provide a systematic description of *S. ningqiangensis* and to clarify its morphologies based on the observations presented herein.

Genus *SHAANXILITHES* Xing, Yue, and Zhang *in* Xing et al., 1984

Type species: *Shaanxilithes ningqiangensis* Xing, Yue, and Zhang *in* Xing et al., 1984

Shaanxilithes ningqiangensis Xing, Yue, and Zhang *in* Xing et al., 1984

(Figs. 3.2–5)

cf. *Sabellidites* Yanichevsky, 1926; Chen, Chen, and Lao, 1975, p. 186, pl. 1, figs. 8, 9.
Shaanxilithes ningqiangensis Xing, Yue, and Zhang *in* Xing et al., 1984, p. 182, pl. 28, figs. 19, 20.
Taenioichnus zhengmuguanensis Yang *in* Yang and Zheng 1985, p. 16, pl. I, fig. 8.
Shaanxilithes erodus Zhang, 1986, p. 83, pl. IV, figs. 11, 13b.
Shaanxilithes sp. Li, Yang, and Li, 1997, p. 73, pl. 5, fig. 2.
Shaanxilithes sp. Hua, Chen, and Zhang, 2004, pl. I, figs. 1–6.
Shaanxilithes cf. *ningqiangensis* Xing, Yue, and Zhang *in* Xing et al., 1984; Shen et al., 2007, p. 1406, fig. 8.8–8.12.
Shaanxilithes ningqiangensis Xing, Yue, and Zhang *in* Xing et al., 1984; Weber et al., 2007, p. 334, fig. 6.
Gaojiashania annulucosta Zhang, Li and Dong in Ding et al., 1992; Zhuravlev et al., 2009, p. 776–777, fig. 2.
Shaanxilithes ningqiangensis Xing, Yue, and Zhang *in* Xing et al., 1984; Cai et al., 2010, p. 491, fig. 4A.
Shaanxilithes ningqiangensis Xing, Yue, and Zhang *in* Xing et al., 1984; Cai and Hua, 2011, p. 329, fig. 1g–l.

3.10.1 Description. Shaanxilithes ningqiangensis is a ribbon-shaped body fossil with millimeter-scale width (0.8–7.8 mm) and centimeter-scale length (up to 95.0 mm in our collection). It has numerous closely spaced annulae (0.16–0.20 mm) with about 5–7 annulae per 1 mm (Fig. 3.2A), clearly defined lateral margins, and no branching structures. From the studied material, ribbon width follows a unimodal distribution (Fig. 3.10), with a maximum width of 7.8 mm and a mode at approximately 2 mm. In the Gaojiashan Member, *S. ningqiangensis* is often found with abundant discoidal structures (Fig. 3.2G–H) that range from ~1 mm to 4 mm in diameter, commonly outnumbering *S. ningqiangensis* specimens at a ratio greater than 5:1. The width of *S. ningqiangensis* is, on average, 1.58× the diameter of the discoidal structures. *S. ningqiangensis* is reconstructed as a cylindrical organism consisting of discoidal, lensoidal, or meniscate segments, perhaps surrounded by an annulated sheath.

3.10.2 Discussion. The Ediacaran fossil *Helanoichnus helanensis* is morphologically similar to *Shaanxilithes ningqiangensis*. The only difference is the lack of annulae in *H. helanensis* (fig. 8.8–8.12 of Shen et al., 2007), which could result from lower preservational quality. Poor preservation is also believed to be the primary difference between the two *Shaanxilithes* species, *S. ningqiangensis* and *S. erodus*, which are likely synonyms (Shen et al., 2007). *Gaojiashania annulucosta* from the late Ediacaran Aim Formation of southeastern Siberia (Zhuravlev et al., 2009) does not fit the diagnosis of the genus *Gaojiashania* (Lin et al., 1986), but is instead similar in morphology to *S. ningqiangensis* (Cai and Hua, 2011).

3.11 Acknowledgments

Financial support for this study was provided by National Science Foundation, National Natural Science Foundation of China (40872021, 41030209, 41028002), NASA Exobiology and Evolutionary Biology Program, the Virginia Tech Institute for Critical Technology and Applied Science Nanoscale Characterization and Fabrication Laboratory, and the Paleontology Society. We would like to thank Charles Farley for technical assistance and anonymous reviewers for constructive comments.

3.12 Tables and Table Captions

Table 3.1. Elemental concentrations (in normalized weight percentages) from EDS point analyses of *Shaanxilithes* ribbons, discoidal structures, and host rock matrix. Spot number: *—spots marked on Figs. 3–8; Sample preparation: U—unpolished bedding surface; P—polished cross section.

Sample #	Spot location	Sample preparation	C	O	Na	Mg	Al	Si	P	S	K	Ca	Ti	Fe	Total
SH09(11, Fig. 3C)*	matrix	U	0.0	60.1	0.0	0.0	2.9	6.3	6.4	0.0	1.4	22.0	0.0	0.9	100
SH09(12, Fig. 3C)*	matrix	U	0.0	52.1	0.0	1.1	6.5	19.9	5.3	0.0	3.9	9.3	0.6	1.4	100
SH13(1, Fig. 4A)*	matrix	U	0.0	50.8	0.0	1.7	8.7	21.9	3.7	0.0	6.4	4.6	0.0	2.2	100
SH13(2, Fig. 4A)*	matrix	U	0.0	36.3	0.0	0.0	0.3	6.6	17.1	0.0	0.7	39.0	0.0	0.0	100
SH13(3, Fig. 4A)*	matrix	U	0.0	53.8	0.0	1.2	9.0	18.8	2.9	0.7	7.3	4.9	0.0	1.6	100
SH11_01(30, Fig. 3D)*	matrix	U	0.0	47.1	0.0	1.2	5.8	15.8	8.6	0.0	4.8	13.8	0.0	3.0	100
SH11_01(28, Fig. 3D)*	matrix	U	0.0	46.3	0.0	1.7	10.0	27.6	0.0	0.0	6.4	0.5	1.1	6.5	100
SH_02_3(4, Fig. 7C)*	matrix	U	1.7	37.7	0.7	0.3	1.4	5.2	13.9	0.4	1.6	36.2	0.2	0.7	100
SH_02_3(5, Fig. 7C)*	matrix	U	2.7	38.8	0.0	0.9	5.6	11.8	0.7	0.0	5.2	10.0	18.5	5.8	100
SH_02_3(6, Fig. 7C)*	matrix	U	4.4	24.0	0.0	0.0	0.3	4.5	7.3	0.0	2.9	54.8	0.5	1.4	100
SH_02_2(4)	matrix	U	0.0	47.3	0.8	2.3	11.2	22.1	0.4	0.1	5.4	1.0	0.8	8.6	100
SH_02_2(5, Fig. 8D)*	matrix	U	3.9	43.0	0.6	1.9	4.7	10.7	8.5	0.2	3.3	20.8	0.4	1.9	100
SH_02_2(6)	matrix	U	4.2	43.4	0.7	0.8	3.2	11.6	9.5	0.3	1.9	23.0	0.2	1.2	100
SH_02_2(7)	matrix	U	4.2	47.8	1.6	1.9	6.1	12.3	5.4	0.3	2.8	12.7	2.6	2.5	100
SH_02_2(8, Fig. 8D)*	matrix	U	3.5	34.0	0.0	0.0	10.6	28.1	0.5	0.0	18.5	2.1	1.3	1.2	100
SH_02_2(9, Fig. 8D)*	matrix	U	5.5	52.2	1.2	1.8	6.6	10.9	3.3	0.1	2.7	8.1	2.4	5.3	100
SH_02_1(6)	matrix	U	1.1	45.7	1.4	0.8	1.6	4.2	12.4	1.6	1.1	29.0	0.0	1.2	100
SH_02_1(7)	matrix	U	4.1	37.3	0.0	2.3	13.2	18.4	0.0	3.4	8.1	2.4	1.8	9.0	100
SH_02_4(1)	matrix	P	3.0	24.0	0.6	0.2	0.3	1.9	18.4	0.6	0.7	49.8	0.1	0.3	100
SH_02_4(2, Fig. 5B)*	matrix	P	1.7	33.3	2.3	9.0	5.2	13.5	1.0	2.8	4.0	22.0	0.6	4.6	100
SH_02_4(7, Fig. 5B)*	matrix	P	2.3	25.5	1.3	1.3	4.8	29.3	7.2	0.6	4.7	21.4	0.2	1.4	100
SH_02_4(12)	matrix	P	2.9	33.2	1.8	2.0	3.6	13.2	10.9	1.8	1.7	25.8	0.2	3.0	100
SH_02_4(13)	matrix	P	2.7	25.9	0.3	0.2	0.9	4.9	16.7	0.5	1.1	46.2	0.1	0.7	100
SH_02_4(14)	matrix	P	3.4	23.8	0.9	0.5	0.6	3.7	13.8	2.6	1.2	37.1	0.1	12.3	100
SH_02_4(20, Fig. 5B)*	matrix	P	2.9	34.2	0.3	0.2	4.3	14.8	9.3	0.2	4.3	28.9	0.1	0.4	100
SH_02_5(1)	matrix	P	0.8	34.7	0.3	0.7	1.4	8.8	11.9	0.7	1.3	38.7	0.0	0.7	100
SH_02_5(5)	matrix	P	0.4	42.5	1.0	16.4	0.3	0.3	0.1	0.5	0.5	35.8	0.0	2.3	100
SH_02_5(6)	matrix	P	0.1	27.2	0.0	10.9	0.0	0.0	0.0	3.7	0.4	55.5	0.0	2.3	100
SH_02_5(9)	matrix	P	3.3	41.4	1.3	2.5	5.3	15.7	6.6	1.8	2.5	17.7	0.3	1.5	100
SH_02_6(0, Fig. 5A)*	matrix	P	1.0	24.3	0.6	0.4	1.3	8.9	16.0	0.5	1.4	44.7	0.0	1.1	100
SH_02_6(4, Fig. 5A)*	matrix	P	0.1	20.2	0.8	0.5	1.3	6.7	18.3	0.5	1.2	49.2	0.0	1.0	100
SH_02_6(5, Fig. 5A)*	matrix	P	0.2	18.8	0.7	0.4	0.7	9.4	18.6	0.7	0.6	49.2	0.0	0.5	100
SH_02_6(9, Fig. 5A)*	matrix	P	0.3	20.2	0.7	0.3	0.1	0.3	19.1	2.2	0.2	51.6	0.0	5.0	100
SH_02_6(10, Fig. 5A)*	matrix	P	2.3	30.7	0.1	0.0	0.9	60.3	1.3	0.1	0.5	2.6	0.3	0.7	100
SH_02_6(14, Fig. 5A)*	matrix	P	0.2	31.7	0.7	0.4	2.9	15.4	12.4	0.4	3.6	31.5	0.0	1.0	100
SH_02_7(1)	matrix	P	1.2	24.0	0.7	0.5	1.5	5.4	15.9	0.8	0.9	44.0	0.3	4.6	100
SH_02_7(2)	matrix	P	1.2	22.1	1.1	0.5	0.8	4.1	18.4	0.7	0.9	49.1	0.3	0.7	100
SH_02_7(6)	matrix	P	0.9	20.6	0.6	0.4	1.1	13.0	17.5	0.6	1.0	43.3	0.3	0.7	100
SH_02_7(10)	matrix	P	2.8	30.6	0.1	1.1	6.3	25.8	6.6	0.2	4.3	18.7	0.6	2.9	100
SH_02_7(13)	matrix	P	1.7	30.6	0.0	1.1	10.3	22.2	0.3	0.4	11.7	3.4	4.7	13.7	100
SH_02_8(4)	matrix	P	3.0	34.5	1.0	0.8	3.3	27.8	7.3	0.4	3.2	17.7	0.2	0.8	100
SH_02_8(5, Fig. 4D)*	matrix	P	3.8	30.8	0.4	0.3	2.1	12.9	12.3	0.3	1.7	34.6	0.1	0.6	100
SH_02_8(13, Fig. 4D)*	matrix	P	2.0	25.8	0.4	0.5	7.9	28.6	5.9	0.3	10.2	17.1	0.2	1.1	100
SH_02_8(14)	matrix	P	3.0	16.6	0.0	0.3	8.8	24.9	2.8	0.5	12.4	13.2	5.8	11.7	100
SH_02_8(17)	matrix	P	0.9	22.1	1.1	1.7	8.9	25.2	2.9	0.8	10.9	12.6	2.1	10.8	100
SH_02_8(20)	matrix	P	1.7	30.6	1.0	1.3	9.7	32.1	2.5	0.3	10.3	8.7	0.5	1.5	100
SH_02_12(11, Fig. 7D)*	matrix	P	5.6	35.9	0.5	0.5	2.5	8.8	12.4	0.4	1.0	31.6	0.3	0.5	100
SH_02_12(12)	matrix	P	6.8	32.1	0.1	0.2	6.1	11.8	8.9	0.3	2.6	29.8	0.3	1.1	100
SH_02_12(13)	matrix	P	4.9	45.4	0.7	0.4	2.6	37.3	1.9	0.2	0.7	5.3	0.0	0.6	100
SH_02_12(14)	matrix	P	7.7	31.3	0.2	0.8	7.1	16.5	4.8	0.2	5.3	15.0	0.0	11.1	100
SH_02_12(15)	matrix	P	6.2	35.9	0.0	0.9	8.1	18.0	3.6	0.0	6.8	13.3	2.7	4.6	100
SH13_2(19)	matrix	P	0.0	46.7	0.0	0.0	6.1	16.7	8.0	0.0	6.8	15.9	0.0	0.0	100
SH13_2(20)	matrix	P	0.0	55.9	2.4	1.1	7.8	19.9	3.4	0.0	7.6	2.1	0.0	0.0	100
SH02 (1, Fig. 6C)*	matrix	P	0.1	41.3	0.0	0.2	2.4	8.8	12.7	0.3	2.7	30.9	0.1	0.5	100
SH02 (2, Fig. 6C)*	matrix	P	0.7	40.6	0.7	0.7	2.9	12.7	11.4	1.7	2.3	24.6	0.0	1.7	100
SH02 (3)	matrix	P	0.0	39.9	0.7	0.0	0.9	2.3	15.0	1.6	1.0	36.9	0.0	1.7	100
SH02 (5, Fig. 6C)*	matrix	P	0.0	40.7	0.0	0.0	7.4	21.8	5.1	0.0	7.7	16.5	0.6	0.0	100
SH02 (7)	matrix	P	2.2	39.7	0.0	0.8	3.3	10.8	10.0	3.0	2.0	25.3	0.0	2.9	100
SH02 (8)	matrix	P	0.3	39.9	0.2	0.2	1.1	9.7	13.0	0.6	1.0	33.7	0.0	0.5	100
SH02 (9, Fig. 6C)*	matrix	P	0.2	34.1	0.0	0.0	0.0	0.0	14.8	7.0	0.0	37.3	0.0	6.7	100
SH02 (12, Fig. 6C)*	matrix	P	0.8	50.9	0.2	0.5	5.7	10.1	6.0	0.0	3.7	21.2	0.0	1.0	100
GJS1(28)	matrix	P	0.0	57.0	0.0	15.5	0.6	0.4	1.2	0.0	0.4	23.5	0.0	1.3	100
GJS1(29)	matrix	P	0.0	50.5	0.0	1.5	8.8	24.1	3.3	0.0	7.7	3.5	0.0	0.6	100
GJS1(30)	matrix	P	0.0	45.0	1.2	0.0	1.2	1.7	17.0	0.0	0.0	34.0	0.0	0.0	100
GJS1(31)	matrix	P	0.0	56.8	0.0	14.9	0.0	1.2	0.0	0.0	0.0	25.7	0.0	1.4	100
GJS1(32)	matrix	P	0.0	47.7	0.6	0.6	4.0	18.1	9.0	0.0	4.0	16.1	0.0	0.0	100
GJS1(33)	matrix	P	0.0	49.8	1.0	4.4	12.1	22.2	0.0	0.0	4.6	0.8	0.0	5.3	100
GJS1(34)	matrix	P	0.0	55.9	0.0	1.5	8.1	24.5	0.0	0.0	4.4	4.0	0.0	1.7	100
GJS2(35)	matrix	P	0.0	55.0	0.0	0.0	9.1	24.5	0.0	0.0	11.4	0.0	0.0	0.0	100
GJS2(36)	matrix	P	0.0	58.7	0.0	16.4	1.2	1.2	0.0	0.0	0.0	21.6	0.0	1.0	100
GJS2(37)	matrix	P	0.0	50.4	0.9	0.0	9.8	27.2	0.0	0.0	11.8	0.0	0.0	0.0	100
GJS2(38)	matrix	P	0.0	56.8	0.3	0.1	1.4	39.6	0.0	0.0	0.4	1.4	0.0	0.0	100
GJS2(39)	matrix	P	0.0	58.0	0.0	0.3	2.2	37.9	0.0	0.0	1.0	0.0	0.0	0.6	100
GJS2(40)	matrix	P	0.0	54.7	0.0	6.8	0.0	19.0	0.0	0.0	0.0	15.0	0.0	4.6	100
Average ± standard error (1σ)			1.6 ± 0.2	39.0 ± 1.4	0.5 ± 0.1	1.9 ± 0.4	4.4 ± 0.4	15.3 ± 1.3	7.3 ± 0.7	0.6 ± 0.1	3.8 ± 0.4	22.3 ± 1.9	0.7 ± 0.3	2.6 ± 0.4	

Table 3.1. Cont.

SH13(4, Fig. 4A)*	ribbon	U	0.0	52.7	0.0	2.4	10.5	23.4	0.0	0.0	5.1	1.6	0.6	3.7	100
SH13(5, Fig. 4A)*	ribbon	U	0.0	51.4	0.0	1.2	10.0	19.2	0.0	0.0	6.0	0.8	3.0	8.5	100
SH13(6, Fig. 4A)*	ribbon	U	0.8	49.0	0.0	1.7	12.8	21.6	0.0	0.0	7.3	0.0	2.3	4.6	100
SH11_01(29, Fig. 3D)*	ribbon	U	0.0	47.9	0.0	1.9	11.0	28.1	0.0	0.0	6.7	0.7	1.0	2.7	100
SH11_01(31, Fig. 3D)*	ribbon	U	0.0	47.7	0.0	1.6	10.0	29.6	0.0	0.0	6.2	0.0	0.9	4.1	100
SH13_2(17)	ribbon	P	0.0	56.2	0.0	2.4	9.4	21.0	0.0	0.0	5.8	0.0	0.0	5.1	100
SH13_2(18)	ribbon	P	0.0	54.2	0.0	2.4	7.8	29.0	0.0	0.0	4.2	0.0	1.1	1.4	100
SH02 (10, Fig. 6C)*	ribbon	P	11.5	25.2	0.0	0.0	3.7	35.5	0.0	0.1	5.3	8.4	6.1	4.3	100
SH02 (11, Fig. 6C)*	ribbon	P	0.3	43.7	0.7	0.6	1.8	5.2	13.6	0.7	1.1	32.0	0.0	0.4	100
GJS2(41)	ribbon	P	0.0	55.8	0.0	12.0	0.5	1.5	2.2	0.0	0.0	25.8	0.0	2.2	100
GJS2(42)	ribbon	P	0.0	60.3	0.0	0.0	1.1	38.0	0.0	0.0	0.6	0.0	0.0	0.0	100
GJS2(43)	ribbon	P	0.0	52.5	0.0	1.4	7.0	27.6	2.3	0.0	5.6	2.9	0.0	0.8	100
SH_02_4(3)	ribbon	P	2.3	16.2	0.0	0.0	5.3	22.1	1.5	2.7	12.9	18.7	7.1	11.1	100
SH_02_4(4)	ribbon	P	4.0	43.1	1.2	2.1	8.6	17.0	2.0	3.8	4.5	9.5	0.9	3.4	100
SH_02_4(5, Fig. 5B)*	ribbon	P	1.6	30.9	0.6	1.1	6.7	20.9	4.0	5.0	6.0	18.2	1.0	4.0	100
SH_02_4(6)	ribbon	P	3.2	36.7	2.0	1.4	3.5	11.8	10.7	1.9	2.5	25.4	0.2	0.7	100
SH_02_4(8, Fig. 5B)*	ribbon	P	1.1	25.8	1.3	2.6	12.2	27.0	0.9	3.6	8.9	7.3	2.4	7.1	100
SH_02_4(9)	ribbon	P	2.3	24.4	0.0	1.4	10.7	25.4	0.5	3.6	10.1	7.9	3.4	10.5	100
SH_02_4(10)	ribbon	P	1.3	39.2	3.5	3.2	7.4	12.9	0.7	3.4	3.1	5.0	17.5	2.8	100
SH_02_4(11, Fig. 5B)*	ribbon	P	2.2	24.7	0.1	1.1	7.3	21.3	3.8	2.8	6.0	15.0	12.0	3.6	100
SH_02_4(15, Fig. 5B)*	ribbon	P	2.4	18.7	0.0	0.2	6.4	19.5	4.9	2.8	11.4	30.5	0.5	2.8	100
SH_02_4(16)	ribbon	P	2.3	29.2	0.0	0.6	5.3	17.4	0.8	6.8	6.8	23.1	1.4	6.4	100
SH_02_4(17)	ribbon	P	3.0	31.7	1.3	3.4	11.4	22.0	2.0	3.3	5.6	7.3	1.4	7.8	100
SH_02_4(18)	ribbon	P	2.8	32.5	1.5	1.2	5.1	18.6	8.1	2.1	3.7	21.8	0.5	1.9	100
SH_02_4(19)	ribbon	P	3.1	33.4	2.2	1.3	2.0	7.2	13.9	1.0	1.0	34.0	0.1	0.7	100
SH_02_5(2)	ribbon	P	3.4	38.6	0.3	1.4	13.0	18.8	0.3	6.1	6.7	9.4	0.5	1.4	100
SH_02_5(3)	ribbon	P	2.2	24.0	0.0	0.0	8.2	21.9	0.0	7.7	13.8	16.3	1.7	4.2	100
SH_02_5(4)	ribbon	P	2.2	24.9	0.0	1.0	10.9	36.6	0.0	2.2	10.5	5.1	2.1	4.5	100
SH_02_5(7)	ribbon	P	3.5	43.3	0.0	0.0	4.0	17.0	0.0	0.0	10.3	6.1	6.8	9.0	100
SH_02_5(8)	ribbon	P	3.0	40.8	0.0	1.3	6.4	18.4	0.5	1.8	7.3	10.7	3.8	6.0	100
SH_02_6(1, Fig. 5A)*	ribbon	P	0.9	24.4	0.5	2.0	13.8	37.2	0.5	0.1	8.9	2.5	2.1	7.2	100
SH_02_6(2, Fig. 5A)*	ribbon	P	3.9	41.3	0.8	2.8	12.4	22.7	1.0	0.1	6.6	2.3	3.0	3.0	100
SH_02_6(3, Fig. 5A)*	ribbon	P	2.3	24.4	0.0	1.5	12.3	32.6	1.5	0.0	11.0	5.9	2.0	6.6	100
SH_02_6(6, Fig.5A)*	ribbon	P	2.0	34.2	0.4	2.3	13.9	26.6	0.9	0.1	8.0	3.3	4.4	3.9	100
SH_02_6(7, Fig. 5A)*	ribbon	P	3.3	32.7	0.2	5.2	15.1	25.9	0.6	0.0	8.1	2.0	1.2	5.8	100
SH_02_6(8, Fig. 5A)*	ribbon	P	2.1	35.6	0.7	2.7	14.0	25.5	0.8	0.1	7.8	2.3	1.7	6.7	100
SH_02_6(11, Fig. 5A)*	ribbon	P	1.6	31.9	0.0	0.8	7.5	37.0	1.8	0.1	6.1	8.6	1.3	3.3	100
SH_02_6(12, Fig. 5A)*	ribbon	P	3.6	40.9	1.1	2.9	13.7	23.0	0.5	0.2	7.4	1.5	2.4	2.8	100
SH_02_6(13, Fig. 5A)*	ribbon	P	2.7	39.1	1.2	1.4	5.5	14.7	8.4	0.3	3.1	20.3	1.0	2.2	100
SH_02_7(3)	ribbon	P	4.1	29.2	0.4	1.6	10.5	22.7	1.1	1.3	10.7	6.0	2.0	10.5	100
SH_02_7(4)	ribbon	P	4.7	32.4	0.5	2.3	12.7	26.3	0.5	1.5	8.6	1.9	2.6	6.3	100
SH_02_7(5)	ribbon	P	1.5	32.3	1.2	1.2	3.5	7.3	13.4	0.5	1.9	33.9	0.8	2.6	100
SH_02_7(7)	ribbon	P	4.5	31.9	0.1	1.7	12.1	21.8	0.0	1.6	9.0	1.3	4.8	11.3	100
SH_02_7(8)	ribbon	P	3.6	9.9	0.0	0.7	13.9	32.4	0.6	0.3	16.8	3.6	7.0	11.1	100
SH_02_7(9)	ribbon	P	4.0	42.3	1.0	2.6	13.3	19.6	0.9	0.1	7.7	1.7	0.9	5.8	100
SH_02_7(11)	ribbon	P	1.1	40.0	1.0	0.9	12.3	28.6	0.3	0.2	14.1	0.7	0.0	0.7	100
SH_02_7(12)	ribbon	P	2.0	19.3	0.0	0.5	12.5	27.1	0.0	0.0	10.7	1.6	4.1	22.2	100
SH_02_8(1, Fig. 4D)*	ribbon	P	2.7	15.8	0.0	0.1	3.6	13.2	11.0	0.1	5.9	39.4	1.7	6.4	100
SH_02_8(2)	ribbon	P	2.2	41.5	1.4	2.4	9.7	26.2	0.7	0.2	6.7	2.6	2.0	4.4	100
SH_02_8(3, Fig. 4D)*	ribbon	P	3.5	38.4	1.3	2.5	10.5	25.3	1.8	0.3	6.3	4.2	1.5	4.3	100
SH_02_8(6)	ribbon	P	1.4	22.6	0.2	0.8	9.9	22.4	6.1	0.5	8.3	21.0	1.0	5.8	100
SH_02_8(7, Fig. 4D)*	ribbon	P	3.1	29.7	0.7	2.0	11.7	29.4	1.3	1.1	8.8	3.4	2.2	6.4	100
SH_02_8(8)	ribbon	P	1.0	29.9	0.5	2.3	8.4	19.7	3.8	0.1	9.9	15.4	1.1	7.7	100
SH_02_8(9)	ribbon	P	4.8	42.6	0.2	0.0	0.6	42.6	2.8	0.1	0.4	5.5	0.1	0.2	100
SH_02_8(10)	ribbon	P	2.5	15.0	0.0	0.0	4.0	16.4	5.7	0.1	9.1	31.9	2.2	13.2	100
SH_02_8(11, Fig. 4D)*	ribbon	P	2.9	25.8	0.9	2.1	10.2	27.3	1.0	5.1	8.5	3.8	2.5	9.8	100
SH_02_8(12)	ribbon	P	2.6	21.8	0.0	0.8	9.6	26.5	3.6	0.1	9.8	13.1	2.8	9.5	100
SH_02_8(15)	ribbon	P	13.3	22.0	2.4	2.9	10.7	22.4	0.5	4.9	7.8	1.9	3.9	7.2	100
SH_02_8(16)	ribbon	P	1.8	29.6	1.1	2.2	11.7	27.7	2.2	0.3	8.4	7.5	1.8	5.6	100
SH_02_8(18)	ribbon	P	5.1	27.0	2.9	3.6	11.3	23.5	0.7	3.6	7.1	2.8	2.2	10.2	100
SH_02_8(19)	ribbon	P	1.2	29.1	0.4	1.1	7.3	38.8	0.4	0.2	5.1	1.7	4.7	9.9	100
Average ± standard error (1σ)			2.5 ± 0.3	34.2 ± 1.5	0.6 ± 0.1	1.8 ± 0.2	8.8 ± 0.5	23.4 ± 1.1	2.4 ± 0.5	1.4 ± 0.2	7.1 ± 0.4	9.8 ± 1.4	2.4 ± 0.4	5.5 ± 0.5	

Table 3.1. Cont.

SH09(7, Fig. 3C)*	disc	U	0.0	51.6	0.0	0.5	11.4	25.0	0.0	0.0	10.0	0.0	0.0	1.5	100
SH09(8, Fig. 3C)*	disc	U	0.0	51.3	0.0	2.2	13.3	21.2	0.0	0.0	6.4	0.0	1.6	4.1	100
SH09(9, Fig. 3C)*	disc	U	0.0	50.8	0.0	2.3	11.8	23.7	0.0	0.0	7.5	0.0	0.9	3.1	100
SH_02_3(1, Fig. 7C)*	disc	U	3.9	45.3	0.3	1.6	6.7	14.5	4.9	0.1	3.9	14.5	0.3	4.0	100
SH_02_3(2, Fig. 7C)*	disc	U	3.2	41.7	0.0	0.4	4.5	11.2	4.0	0.0	3.3	29.0	0.5	2.3	100
SH_02_3(3, Fig. 7C)*	disc	U	4.6	44.7	0.3	1.2	8.0	17.9	3.5	0.1	6.0	10.8	0.6	2.4	100
SH_02_2(1, Fig. 8D)*	disc	U	3.9	40.5	0.0	4.5	12.9	19.3	0.3	0.0	6.8	2.1	1.1	8.5	100
SH_02_2(2, Fig. 8D)*	disc	U	0.9	10.5	0.0	0.0	3.0	7.6	3.8	0.0	5.2	26.3	1.5	41.2	100
SH_02_2(3, Fig. 8D)*	disc	U	1.3	40.7	0.1	1.0	7.5	15.5	6.2	0.0	6.0	16.0	2.1	3.8	100
SH_02_2(10)	disc	U	3.2	44.0	0.1	1.8	8.5	18.2	2.6	0.1	4.7	9.0	0.9	7.0	100
SH_02_2(11)	disc	U	2.5	30.5	0.0	4.5	13.6	20.9	0.0	0.0	9.1	1.6	2.8	14.5	100
SH_02_1(1)	disc	U	2.7	36.3	0.2	0.3	2.4	11.2	12.1	0.5	2.5	30.8	0.2	0.7	100
SH_02_1(2)	disc	U	3.6	41.8	0.6	0.7	2.8	9.3	10.7	0.5	2.1	26.7	0.2	0.8	100
SH_02_1(3)	disc	U	1.4	29.6	0.0	0.5	9.0	22.8	0.9	0.0	11.0	7.6	11.4	5.9	100
SH_02_1(4)	disc	U	2.8	33.9	0.0	0.4	7.6	24.7	2.6	0.0	8.1	15.9	0.9	3.1	100
SH_02_1(5)	disc	U	4.4	47.4	1.3	0.9	4.8	10.0	8.0	0.4	4.3	17.6	0.4	0.5	100
SH_02_9(1)	disc	P	5.0	38.3	0.2	1.6	4.0	6.1	10.4	0.8	1.7	28.5	0.3	3.0	100
SH_02_9(2)	disc	P	1.4	39.0	0.8	0.5	1.2	3.6	14.1	0.5	0.9	37.6	0.0	0.4	100
SH_02_9(3)	disc	P	2.1	41.7	0.2	0.3	7.1	6.0	10.9	0.4	1.5	29.2	0.0	0.5	100
SH_02_9(4)	disc	P	1.7	38.6	0.1	0.3	3.8	10.8	10.9	0.3	1.8	30.4	0.0	1.1	100
SH_02_9(5)	disc	P	16.6	42.7	1.5	0.7	2.0	4.1	5.6	5.4	0.4	16.7	0.0	4.2	100
SH_02_9(6)	disc	P	6.1	26.5	0.0	0.0	0.9	3.0	9.2	0.6	0.7	51.1	0.3	1.6	100
SH_02_9(7)	disc	P	3.5	37.2	0.3	0.2	0.8	4.1	14.2	0.4	0.5	38.2	0.2	0.4	100
SH_02_9(8)	disc	P	1.0	40.4	0.5	0.4	1.9	7.3	12.0	0.5	1.1	34.3	0.0	0.5	100
SH_02_9(9)	disc	P	1.2	43.6	0.9	0.5	0.7	2.0	14.3	0.4	0.4	35.4	0.0	0.6	100
SH_02_9(10)	disc	P	2.0	33.9	0.3	0.5	3.0	10.4	13.1	0.4	2.7	33.0	0.0	0.8	100
SH_02_10(1)	disc	P	3.3	40.2	0.7	0.7	2.4	8.9	12.1	0.5	1.3	29.2	0.0	0.8	100
SH_02_10(2, Fig. 8C)*	disc	P	5.3	46.4	0.0	0.7	5.7	13.7	4.0	0.0	3.8	15.4	0.9	4.0	100
SH_02_10(3, Fig. 8C)*	disc	P	5.8	43.5	0.3	1.7	7.7	18.0	4.0	0.2	3.8	10.2	0.8	4.1	100
SH_02_10(4, Fig. 8C)*	disc	P	11.2	48.4	0.8	1.1	4.7	26.1	1.4	0.4	1.9	2.8	0.4	0.9	100
SH_02_10(5, Fig. 8C)*	disc	P	1.3	48.2	0.7	0.8	3.2	11.6	8.5	0.3	1.9	22.3	0.0	1.2	100
SH_02_10(6, Fig. 8C)*	disc	P	1.4	38.8	0.1	0.1	2.5	18.7	9.9	0.2	1.2	26.4	0.0	0.8	100
SH_02_10(7)	disc	P	1.5	48.9	0.9	0.7	3.1	9.0	9.2	0.3	2.2	23.4	0.0	0.8	100
SH_02_10(8)	disc	P	1.9	45.2	0.2	0.6	4.7	12.2	8.2	0.2	2.4	23.0	0.0	1.2	100
SH_02_11(1)	disc	P	7.0	33.5	0.2	0.3	6.0	20.1	5.6	0.2	6.5	16.8	2.4	1.2	100
SH_02_11(2)	disc	P	3.1	36.1	0.5	0.6	4.2	14.3	9.8	0.4	3.5	25.1	0.3	2.3	100
SH_02_11(3)	disc	P	5.4	41.1	0.9	0.6	3.2	8.0	10.6	0.4	2.2	26.1	0.0	1.4	100
SH_02_11(4)	disc	P	4.1	38.1	0.5	0.3	8.5	22.3	4.1	0.2	11.3	9.8	0.0	0.7	100
SH_02_11(6)	disc	P	6.3	41.0	0.8	0.5	6.6	9.4	9.5	0.8	0.4	23.3	0.0	1.3	100
SH_02_11(7)	disc	P	0.8	43.5	0.9	1.2	4.0	10.0	10.7	0.5	2.0	25.3	0.0	1.1	100
SH_02_12(16)	disc	P	7.2	34.9	0.2	0.7	5.1	11.8	9.7	0.3	2.9	25.5	0.5	1.2	100
SH_02_12(17)	disc	P	1.8	44.7	0.7	1.3	4.9	14.4	8.2	0.3	2.7	19.3	0.0	1.8	100
SH_02_12(18, Fig. 7D)*	disc	P	1.6	32.6	0.4	0.3	2.3	10.8	12.9	0.4	2.1	34.9	0.0	1.8	100
SH_02_12(19)	disc	P	1.8	40.9	0.6	0.5	2.3	15.0	9.8	0.4	1.1	26.0	0.0	1.6	100
SH_02_12(20)	disc	P	4.8	35.9	1.1	0.5	0.9	3.3	15.3	0.5	0.3	36.9	0.0	0.4	100
Average ± standard error (1σ)			3.4 ± 0.5	40.1 ± 1.1	0.4 ± 0.1	0.9 ± 0.1	5.2 ± 0.5	13.1 ± 1	7.1 ± 0.7	0.4 ± 0.1	3.6 ± 0.4	21.4 ± 1.8	0.7 ± 0.3	3.2 ± 0.9	
Ribbons and discs combined															
Average ± s.e. (1σ):			2.9 ± 0.3	36.7 ± 1	0.5 ± 0.1	1.4 ± 0.1	7.3 ± 0.4	19 ± 0.9	4.6 ± 0.5	1.0 ± 0.2	5.6 ± 0.4	14.7 ± 1.2	1.7 ± 0.3	4.6 ± 0.5	

Table 3.2. Elemental concentrations (in normalized weight percentages) from EDS point analyses of a *Shaanxilithes* ribbon cut in cross section (Fig. 6B).

Sample #	C	O	Mg	Al	Si	S	K	Ca	Ti	Fe	Total
Sh11_S1(Fig. 6B)*	14.8	20.4	3.8	12.8	22.1	3.0	5.6	1.3	3.1	12.9	100.0
Sh11_S2(Fig. 6B)*	14.2	21.3	2.0	9.9	25.5	11.4	7.2	3.2	1.3	3.9	100.0
Sh11_S3(Fig. 6B)*	4.1	46.0	1.5	10.5	23.1	0.0	7.6	1.9	2.2	3.2	100.0
Sh11_S4(Fig. 6B)*	1.8	35.3	3.7	14.5	26.2	0.0	8.1	1.6	1.2	7.6	100.0
Sh11_S5(Fig. 6B)*	17.0	25.1	1.8	10.3	28.4	6.2	5.6	1.4	2.0	2.2	100.0
Sh11_S6(Fig. 6B)*	23.0	26.9	1.3	8.4	24.1	5.1	5.9	1.1	1.5	2.5	100.0

3.13 Figures and Figure Captions

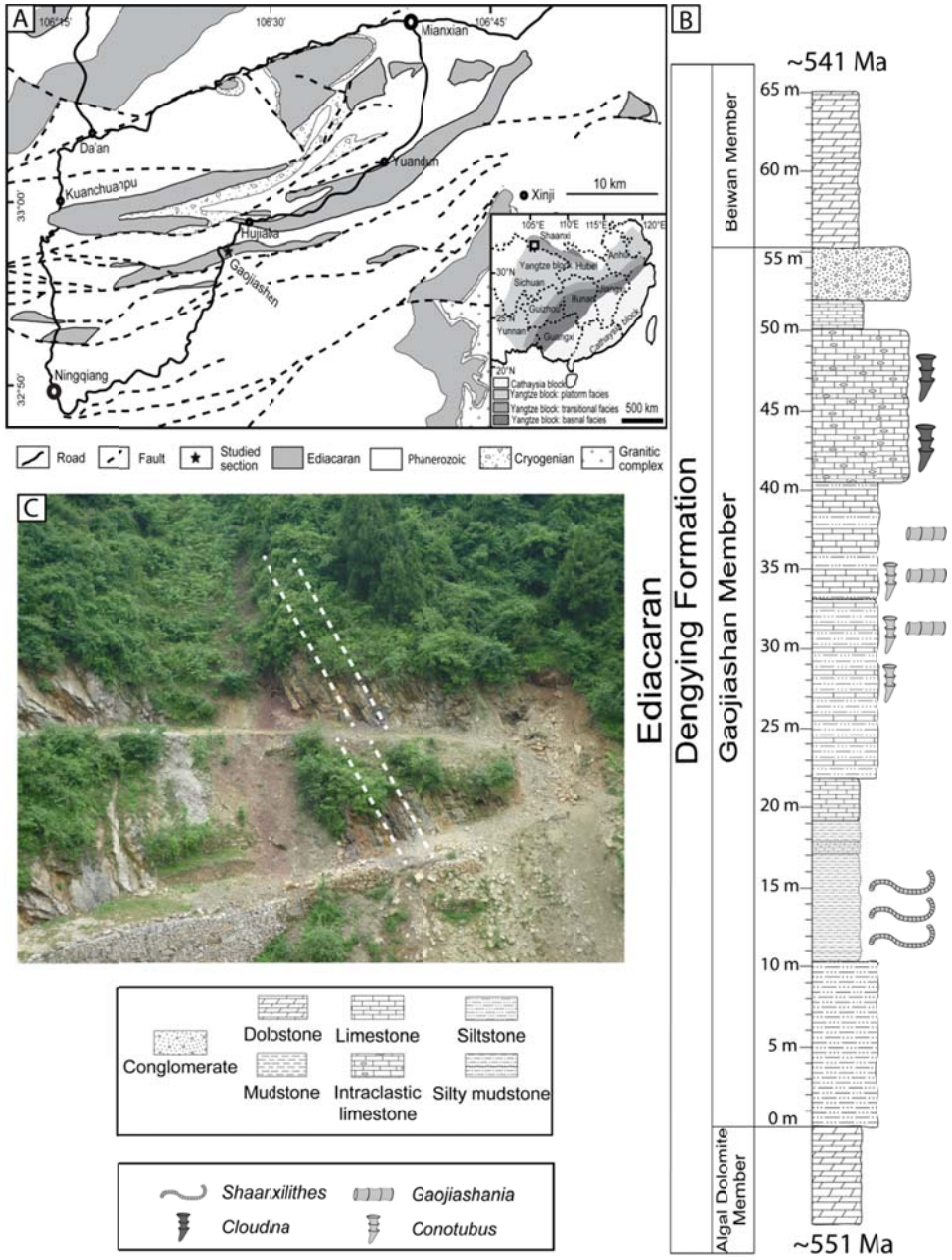

Figure 3.1. Geological map and stratigraphic column. (A) Geological map of the Ningqiang area showing the location of the Gaojiashan section. Inset shows important tectonic blocks in China with, the Ningqiang area (box) located in the northwestern margin of the Yangtze block . Modified from Cai et al. (2010). (B) Stratigraphic column of the Gaojiashan section showing the fossil horizon of *Shaanxilithes ningqiangensis*. Modified from Cai et al. (2011). (C) Field photo of the lower Gaojiashan Member. Dashed lines bracket the interval in which *Shaanxilithes ningqiangensis* specimens were collected for this study.

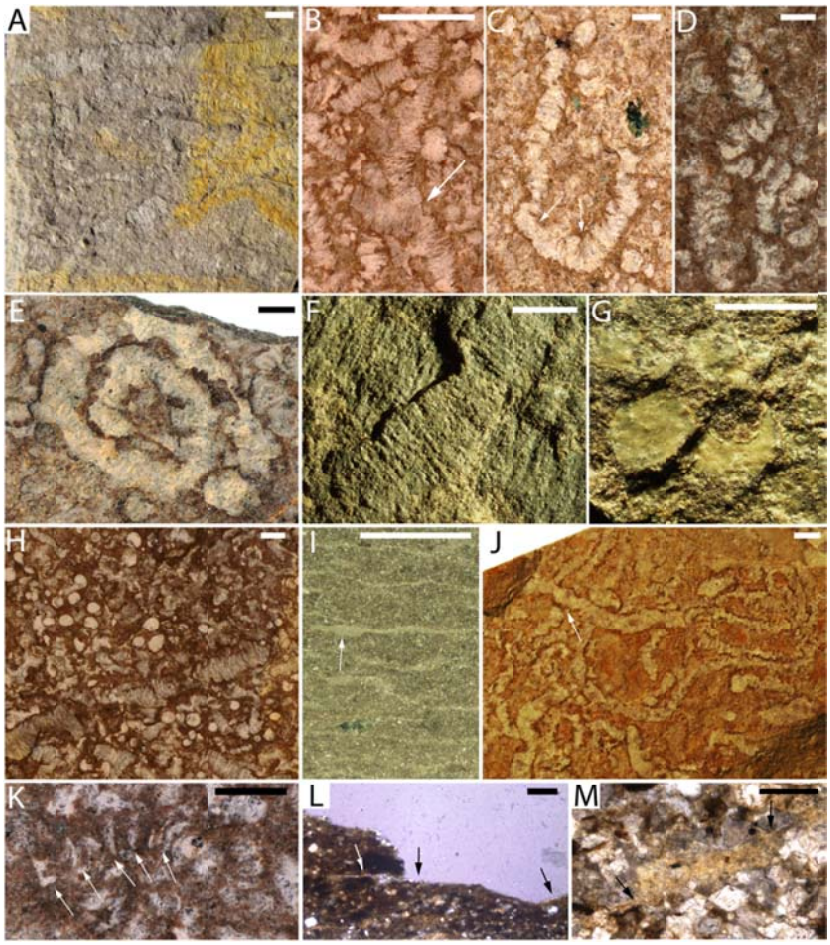

Figure 3.2. Light photography of *Shaanxilithes ningqiangensis* ribbons and related discoidal structures. All are bedding surface views except otherwise indicated. (A) Hand specimen covered with *Shaanxilithes* ribbons. Colors are from weathering. VPIGM-4621. (B) Dense accumulation of ribbons and discoidal structures. Arrow points to two overlapping ribbons. VPIGM-4622. (C) Kinked or sharply bent ribbons and discoidal structures. Arrows denote bending points. VPIGM-4623. (D) Slightly disarticulated and bent ribbon. VPIGM-4624-A. (E) Highly curved ribbon without preservation of annulation. VPIGM-4625. (F) Two over-lapping ribbons. VPIGM-4626. (G) Close up of discoidal structures slightly askew from bedding plane. VPIGM-4627. (H) Numerous discoidal structures with some *Shaanxilithes* ribbons. VPIGM-4628. (I) Light grey clay-rich stringers (arrow) representing *Shaanxilithes* ribbons on polished cross section cut perpendicular to bedding plane. VPIGM-4629. (J) Densely accumulated and overlapping ribbons (arrow). VPIGM-4630. (K) Disarticulated segments (arrows) resting perpendicular to bedding plane on a bedding surface view. VPIGM-4624-B. (L) Transverse section of *Shaanxilithes* ribbon (arrows) in thin-section cut perpendicular to bedding plane, under plane polarized transmitted light. Fossil lies on bedding surface and partially exposed. This specimen is also seen in Fig. 6. VPIGM-4631. (M) Thin-section perpendicular to bedding plane showing partially exposed specimen in cross-section under cross polarized light. Arrows delineate fossil. VPIGM-4632. Scale bar is 1 cm for (A), 2 mm for (B–K), 500 μm for (L), and 100 μm for (M).

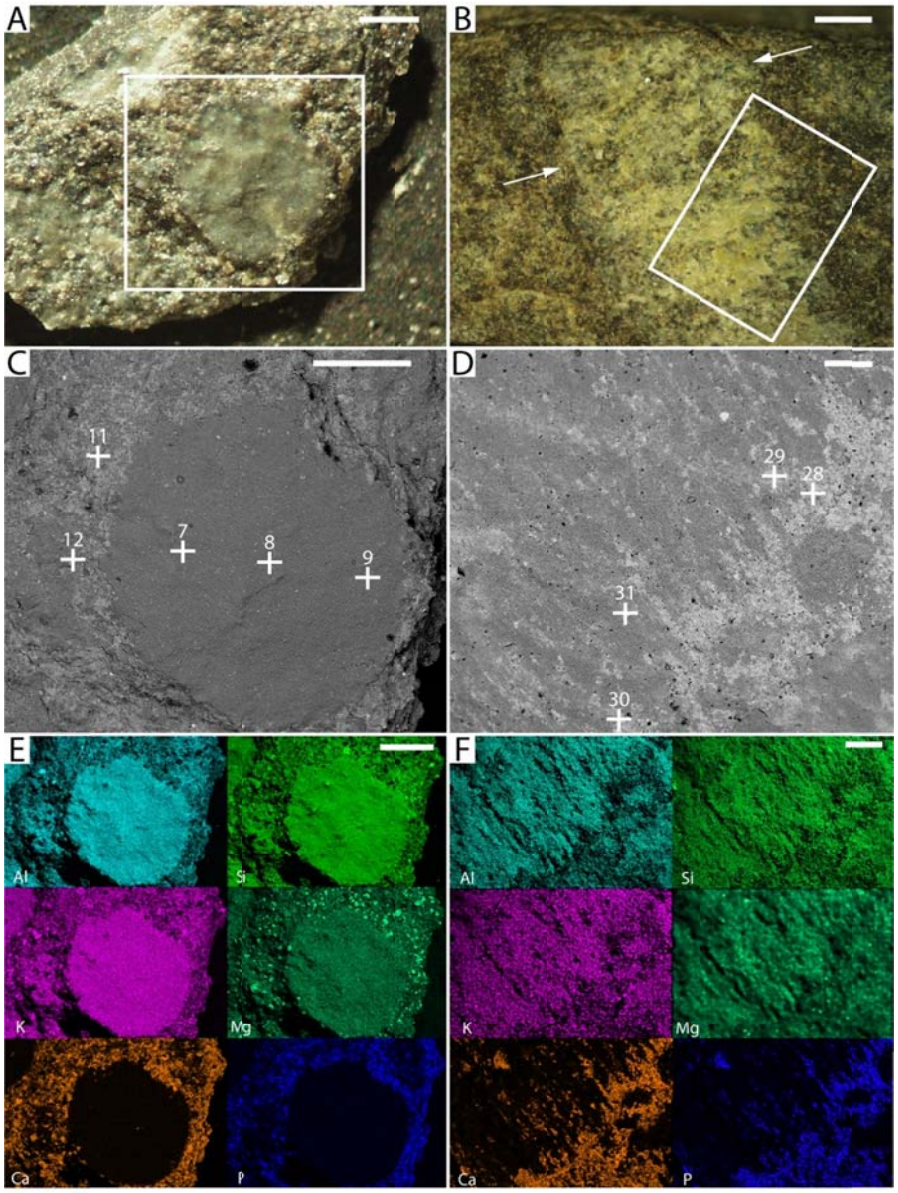

Figure 3.3. Reflected light photomicrographs, BSE images, and EDS elemental maps of discoidal structure and *Shaanxilithes* ribbon on bedding surface. (A, C, E) Light photomicrographs (A), BSE image (C), and EDS elemental maps (E) of a discoidal structure. VPIGM-4633. (B, D, F) Light photomicrograph (B), BSE image (D), and EDS elemental maps (F) of a *Shaanxilithes* ribbon (bracketed by arrows in B). VPIGM-4634. Rectangles outline areas analyzed by BSE and EDS. Crosses denote EDS point analysis locations (results shown in Table 1). Scale bar is 1 mm for (B) and (D), 500 μm for (A) and (C), and 400 μm for (E) and (F).

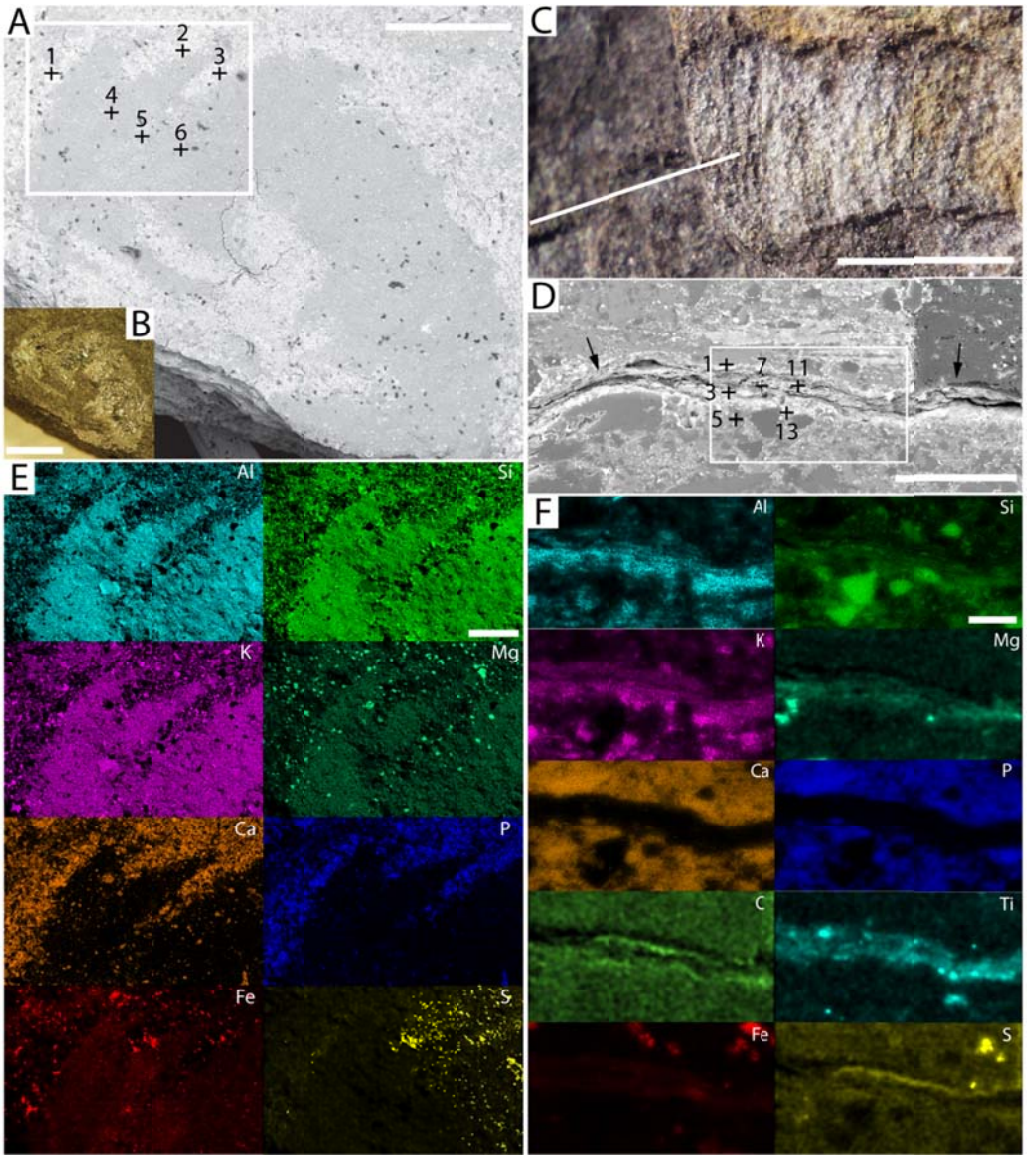

Figure 3.4. Reflected light photomicrographs (B–C), BSE images (A, D), and EDS elemental maps (E–F) of *Shaanxilithes* ribbons on unpolished bedding surface (A–B, E) and on polished slab perpendicular to bedding plane (C–D, F). (A–B, E) Slightly disarticulated ribbon with meniscate segments. Rectangle in (A) corresponds to mapped area in (E). VPIGM-4635. (C–D, F) Partially exposed ribbon cut in cross section perpendicular to bedding surface. Line in (C) denotes approximate location of cross section. Arrows in (D) denote the location of the unexposed part of fossil ribbon. Rectangle in (D) corresponds to mapped area in (F). VPIGM-4636-A. Crosses denote EDS point analysis locations (results shown in Table 3.1). Scale bar is 500 µm for (A), 1 mm for (B) and (C), 50 µm for (D), 400 µm for (E), and 20 µm for (F).

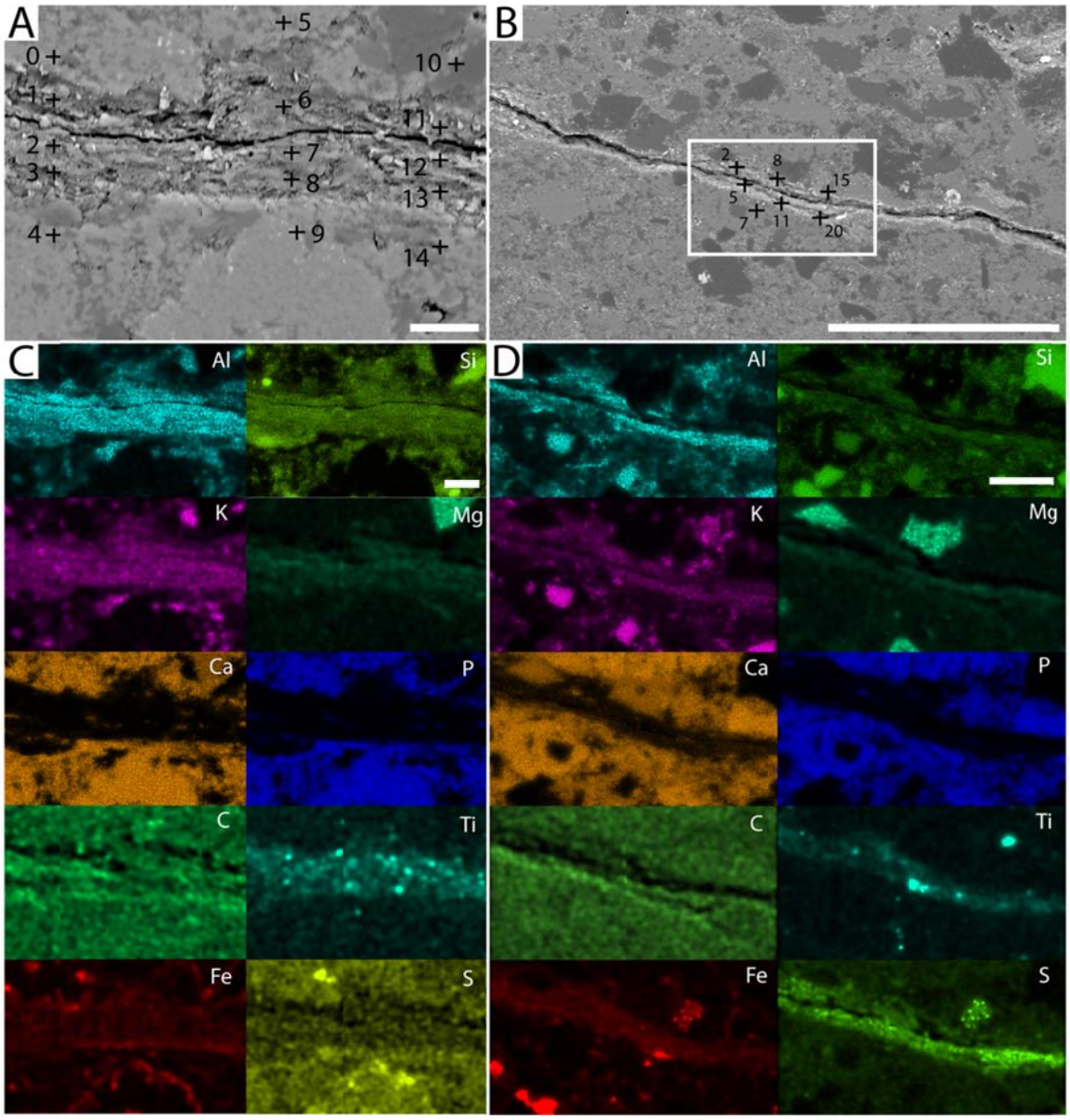

Figure 3.5. BSE images (A, VPIGM-4636-B; B, VPIGM-4636-C) and EDS elemental maps (C–D) of partially exposed *Shaanxilithes* ribbon on polished slab perpendicular to bedding plane. Both views (A and B) are on the same slab shown in Fig. 3.4C–D, and can be traced to the partially exposed ribbon shown in Fig. 3.4C. Box in (B) corresponds to area shown in (D). Crosses denote EDS point analysis locations (results shown in Table 1). Scale bar is 20 μm for (A), 200 μm for (B), 20 μm for (C), and 40 μm for (D).

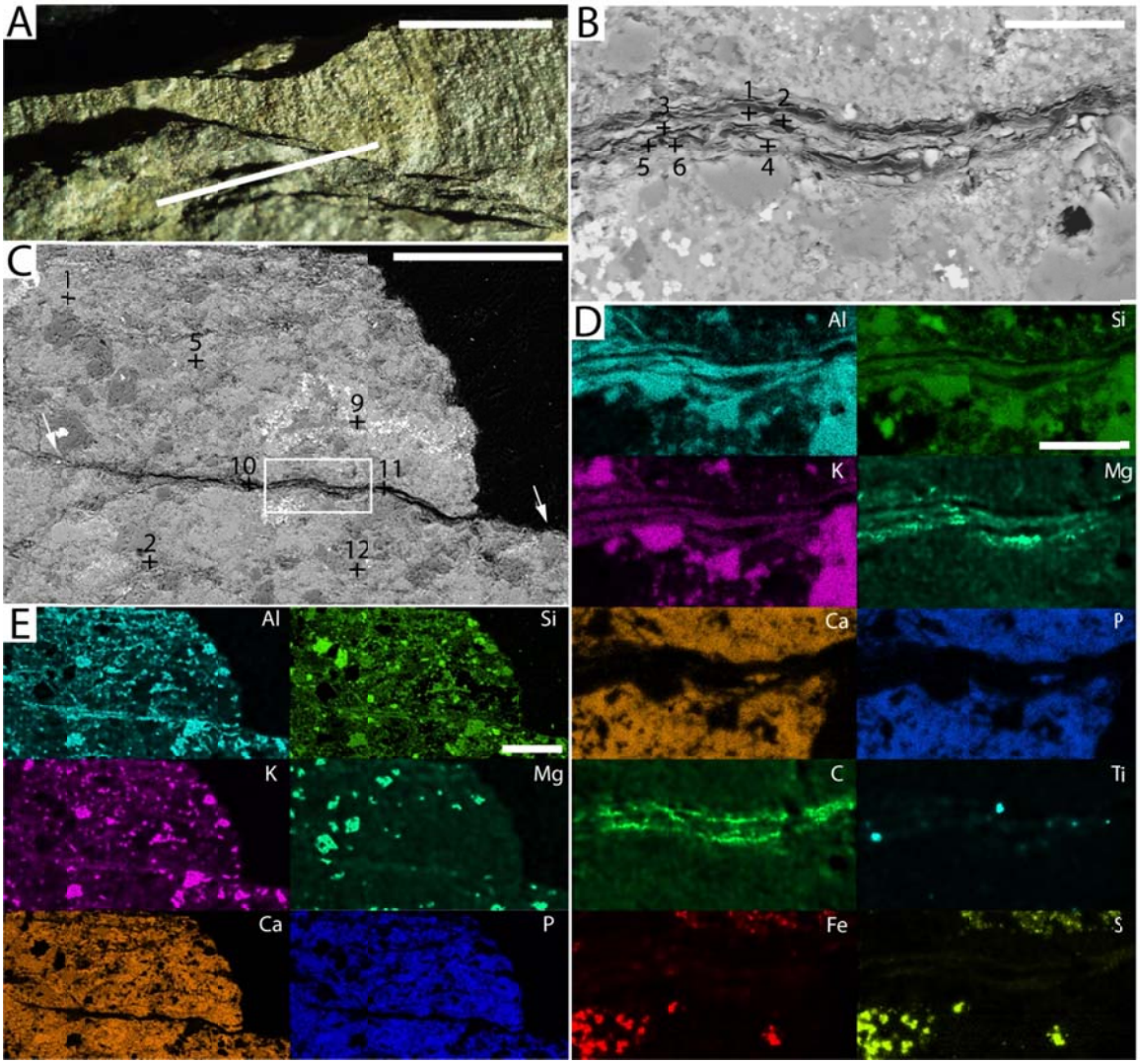

Figure 3.6. Reflected light photomicrograph (A, lighting from lower right), BSE images (B–C), and EDS elemental maps (D–E) of a partially exposed *Shaanxilithes* ribbon on polished slab perpendicular to bedding plane. Line in (A) denotes approximate location of cross section cut perpendicular to bedding surface, arrows in (C) denote the location of the fossil ribbon, and box corresponds to area shown in (B) and (D). VPIGM-4631. Crosses denote EDS point analysis locations [results for (C) shown in Table 1 and results for (B) are shown in Table 3.2]. Scale bar is 1 mm for (A), 20 µm for (B), 500 µm for (C), 20 µm for (D), and 400 µm for (E).

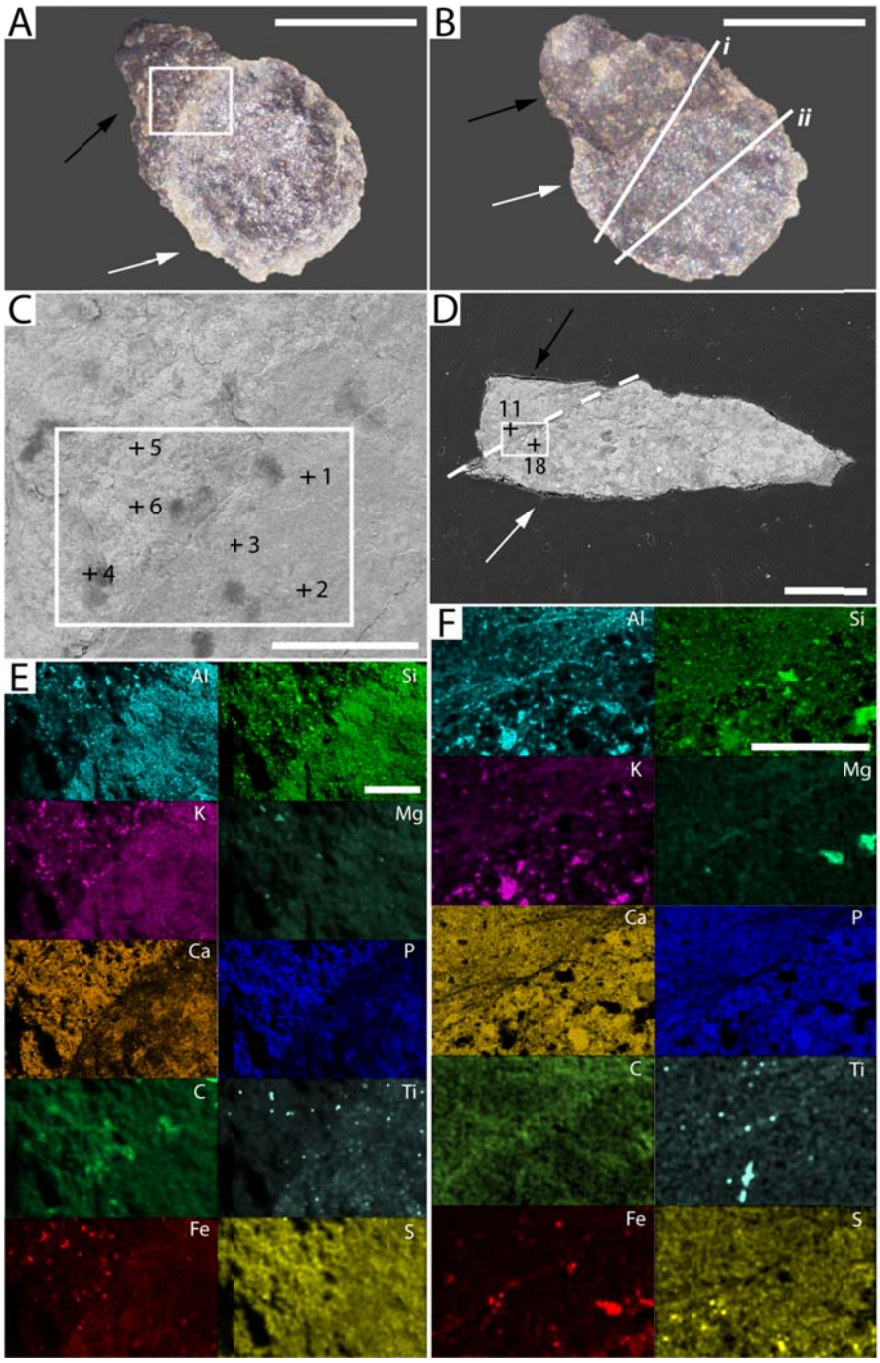

Figure 3.7. Reflected light photomicrographs (A–B, obverse and reverse views of the same specimen VPIGM-4637), BSE images (C–D), and EDS elemental maps (E–F) of a three dimensionally preserved lensoidal structure. In photomicrographs (A–B), white arrows point to fossil, black arrows point to attached matrix, line *i* denotes the approximate location of cross section shown in (D), and line *ii* denotes the approximate location of cross section shown in Fig. 3.8A, C, E. White boxes in (C) and (D) correspond to areas shown in (E) and (F), respectively. Crosses denote EDS point analysis locations (results shown in Table 1). Scale bar is 1 mm for (A–B), and 200 μm for (C–F).

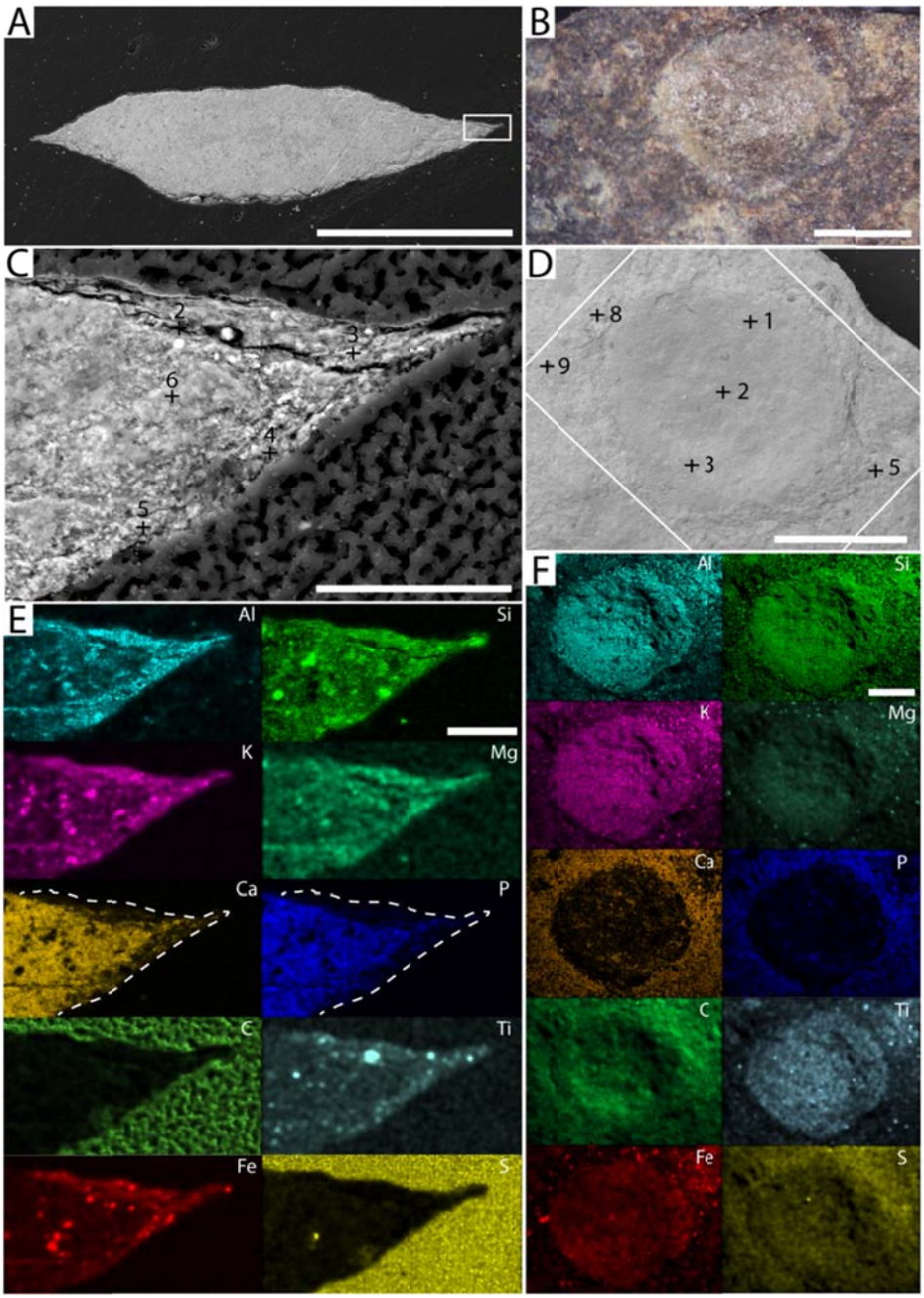

Figure 3.8. Reflected light photomicrograph (A, VPIGM-4637; B, VPIGM-4638), BSE images (C–D), and EDS elemental maps (E–F) of a three-dimensionally preserved lensoidal structure (A) and its mold (B). White box in (A) corresponds to area shown in (C) and (E), while white box in (D) corresponds to area shown in (F). Note in (E) an aluminosilicate envelope wraps around the discoidal structure on both sides. Dashed lines in (E) mark margin of lensoidal structure to highlight low Ca and P concentrations in aluminosilicate envelope. Crosses denote EDS point analysis locations (results shown in Table 1). Scale bar is 500 μm for (A), 1 mm for (B), 1mm for (C), and 50 μm for (D–F).

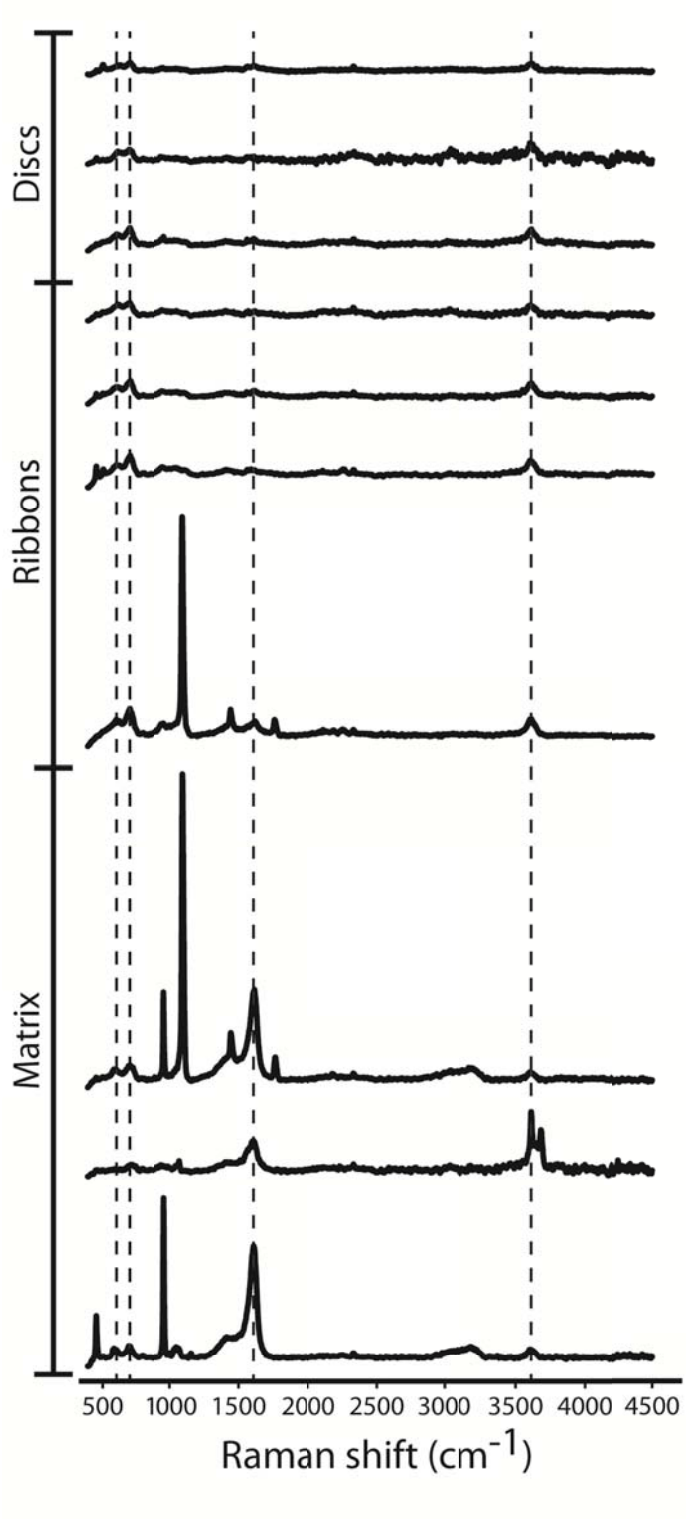

Figure 3.9. Raman spectra for disc, ribbon, and matrix samples. Dashed lines located at ~600, ~700, ~1600, and ~3600 cm^{-1}.

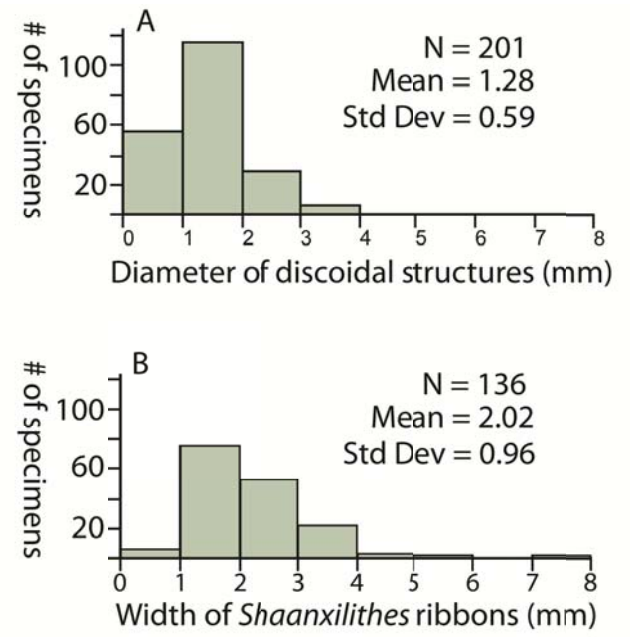

Figure 3.10. Histograms showing measurements of diameter of discoidal structures (A) and width of *Shaanxilithes* ribbons (B).

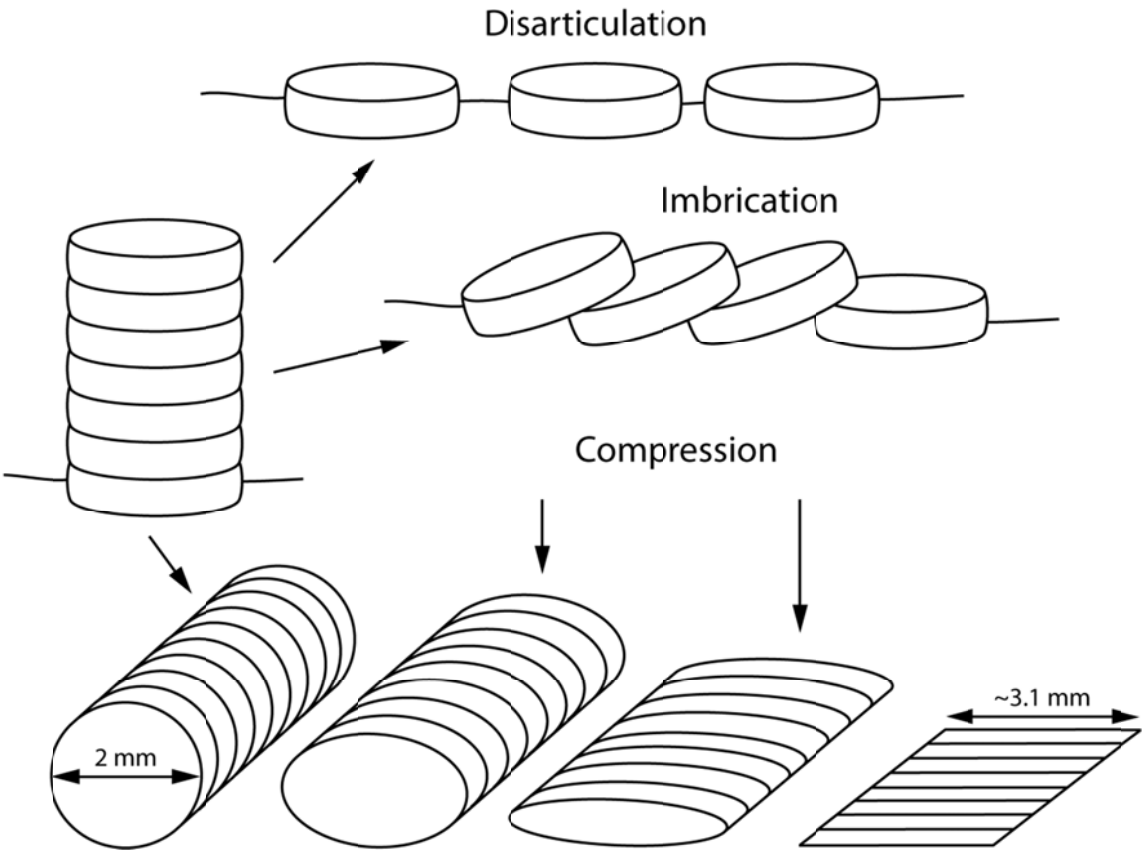

Figure 3.11. Possible taphonomic interpretations of the different morphologies of *Shaanxilithes* ribbons and discoidal structures. The *Shaanxilithes* organism is interpreted as consisting of discoidal modules that could be imbricated or disarticulated. *Shaanxilithes* ribbons could represent compressed specimens. The discoidal structures could be lens-shaped or meniscate in morphology, but are shown here as thin cylinders for simplicity.

3.14 References

ANDERSON, E., SCHIFFBAUER, J.D., and XIAO, S., 2011, Taphonomic study of organic-walled microfossils confirms the importance of clay minerals and pyrite in Burgess Shale-type preservation: Geology, v. 39, p. 643-646.

AWONUSI, A., MORRIS, M.D., and TECKLENBURG, M.M.J., 2007, Carbonate Assignment and calibration in the Raman Spectrum of Apatite: Calcified Tissue International, v. 81, p. 46-52.

BALACHANDRAN, U., and EROR, N.G., 1982, Raman Spectra of Titanium Dioxide: Journal of Solid State Chemistry, v. 42, p. 276-282.

BRIGGS, D.E.G., 2003, The role of decay and mineralization in the preservation of soft-bodied fossils: Annual Review of Earth and Planetary Sciences, v. 31, p. 275-301.

BUTTERFIELD, N.J., 1990, Organic preservation of non-mineralizing organisms and the taphonomy of the Burgess Shale: Paleobiology, v. 16, p. 272-286.

BUTTERFIELD, N.J., 1995, Secular distribution of Burgess Shale-type preservation: Lethaia, v. 28, p. 1-13.

BUTTERFIELD, N.J., 2003, Exceptional fossil preservation and the Cambrian Explosion: Integrative and Comparative Biology, v. 43, p. 166-177.

BUTTERFIELD, N.J., BALTHASAR, U., and WILSON, L.A., 2007, Fossil diagenesis in the Burgess Shale: Palaeontology, v. 50, p. 537–543.

CAI, Y., and HUA, H., 2011, Discussion of 'First finds of problematic Ediacaran fossil *Gaojiashania* in Siberia and its origin': Geology Magazine, v. 148, p. 329-333.

CAI, Y., HUA, H., XIAO, S., SCHIFFBAUER, J.D., and LI, P., 2010, Biostratinomy of the late Ediacaran pyritized Gaojiashan Lagerstätte from southern Shaanxi, south China: Importance of event deposits: Palaios, v. 25, p. 487-506.

CAI, Y., SCHIFFBAUER, J.D., HUA, H., and XIAO, S., 2011, Morphology and paleoecology of the late Ediacaran tubular fossil *Conotubus hemiannulatus* from the Gaojiashan Lagerstätte of southern Shaanxi Province, South China: Precambrian Research, v. 191, p. 46-57.

CAI, Y., SCHIFFBAUER, J.D., HUA, H., and XIAO, S., 2012, Preservational modes in the Ediacaran Gaojiashan Lagerstätte: Pyritization, aluminosilicification, and carbonaceous compression: Palaeogeography Palaeoclimatology Palaeoecology, v. 326-328, p. 109-117, doi: 10.1016/j.palaeo.2012.02.009.

DARROCH, S.A.F., LAFLAMME, M., SCHIFFBAUER, J.D., and BRIGGS, D.E.G., 2012, Experimental formation of a microbial death mask: Palaios, v. 27, p. 293-303, doi: 10.2110/palo.2011.p11-059r.

DONG, L., XIAO, S., SHEN, B., and ZHOU, C., 2008, Silicified *Horodyskia* and *Palaeopascichnus* from upper Ediacaran cherts in South China: tentative phylogenetic interpretation and implications for evolutionary stasis: Journal of the Geological Society of London, v. 165, p. 367-378.

DONG, L., XIAO, S., SHEN, B., ZHOU, C., LI, G., and YAO, J., 2009, Basal Cambrian microfossils from the Yangtze Gorges area (South China) and the Aksu area (Tarim Block, northwestern China): Journal of Paleontology, v. 83, p. 30-44.

DROSER, M.L., and GEHLING, J.G., 2008, Synchronous aggregate growth in an abundant new Ediacaran tubular organism: Science, v. 319, p. 1660-1662.

DROSER, M.L., GEHLING, J.G., and JENSEN, S., 2005, Ediacaran trace fossils: true and false, *in* Briggs, D.E.G., ed., Evolving Form and Function: Fossils and Development: Yale Peabody Museum Publications, New Haven, CT, p. 125-138.

GABBOTT, S.E., HOU, X.G., NORRY, M.J., and SIVETER, D.J., 2004, Preservation of Early Cambrian animals of the Chengjiang biota: Geology, v. 32, p. 901-904.

GAINES, R.R., BRIGGS, D.E.G., and ZHAO, Y.L., 2008, Cambrian Burgess Shale-type deposits share a common mode of fossilization: Geology, v. 36, p. 755-758, doi: Doi 10.1130/G24961a.1.

GAINES, R.R., KENNEDY, M.J., and DROSER, M.L., 2005, A new hypothesis for organic preservation of Burgess Shale taxa in the middle Cambrian Wheeler Formation, House Range, Utah: Palaeogeography, Palaeoclimatology, Palaeoecology, v. 220, p. 193-205.

GEHLING, J.G., 1999, Microbial mats in terminal Proterozoic siliciclastics: Ediacaran death masks: Palaios, v. 14, p. 40-57.

HUA, H., CHEN, Z., and ZHANG, L., 2004, *Shaanxilithes* from lower Taozichong Formation, Guizhou Province and its geological and paleobiological significance: Journal of Stratigraphy, v. 28, p. 265-269.

JENSEN, S., 2003, The Proterozoic and earliest Cambrian trace fossil record: patterns, problems and perspectives: Integrative and Comparative Biology, v. 43, p. 219-228.

JENSEN, S., DROSER, M.L., and GEHLING, J.G., 2006, A critical look at the Ediacaran trace fossil record, *in* Xiao, S., and Kaufman, A.J., eds., Neoproterozoic Geobiology: Springer, Dordrecht, the Netherlands, p. 115-157.

LAFLAMME, M., SCHIFFBAUER, J.D., NARBONNE, G.M., and BRIGGS, D.G., 2011, Microbial biofilms and the preservation of the Ediacara biota: Lethaia, v. 44, p. 203-213.

LAFLAMME, M., XIAO, S., and KOWALEWSKI, M., 2009, Osmotrophy in modular Ediacara organisms: Proceedings of the National Academy of Sciences, USA, v. 106, p. 14438–14443.

LIN, J.-P., and BRIGGS, D.E.G., 2010, Burgess Shale-type preservation: a comparison of naraoiids (Arthropoda) from three Cambrian localities: Palaios, v. 25, p. 463-467.

LIN, S., ZHANG, Y., ZHANG, L., TAO, X., and WANG, M., 1986, Body and trace fossils of metazoa and algal macrofossils from the upper Sinian Gaojiashan Formation in southern Shaanxi: Geology of Shaanxi, v. 4, p. 9-17.

LIU, A.G., MCILROY, D., ANTCLIFFE, J.B., and BRASIER, M.D., 2011, Effaced preservation in the Ediacara biota and its implications for the early macofossil record: Palaeontology, v. 54, p. 607-630.

MARTIN, D., BRIGGS, D.E.G., and PARKES, R.J., 2004, Experimental attachment of sediment particles to invertebrate eggs and the preservation of soft-bodied fossils: Journal of the Geological Society London, v. 161, p. 735–738.

MAZZA, T., BARBORINI, E., PISERI, P., MILANI, P., CATTANEO, D., BASSI, A.L., BOTTANI, C.E., and DUCATI, C., 2007, Raman spectroscopy characterization of TiO_2 rutile nanocrystals: Physical Review B, v. 75, p. 0454161-5.

MCKEOWN, D.A., BELL, M.I., and ETZ, E.S., 1999, Vibrational analysis of the dioctahedral mica: $2M_1$ muscovite: American Mineralogist, v. 84, p. 1041-1048.

NARBONNE, G.M., 2004, Modular construction of early Ediacaran complex life forms: Science, v. 305, p. 1141-1144.
NARBONNE, G.M., 2005, The Ediacara Biota: Neoproterozoic origin of animals and their ecosystems: Annual Review of Earth and Planetary Sciences, v. 33, p. 421-442.
NICOLA, J.H., SCOTT, J.F., COUTO, R.M., and CORREA, M.M., 1976, Raman spectra of Dolomite [$CaMg(CO_3)_2$]: Physical Review B, v. 14, p. 4676-4678.
ORR, P., KEARNS, S.L., and BRIGGS, D.E.G., 2002, Backscattered electron imaging of fossils exceptionally-preserved as organic compressions: Palaios, v. 17, p. 110-117.
ORR, P.J., BRIGGS, D.E.G., and KEARNS, S.L., 1998, Cambrian Burgess Shale animals replicated in clay minerals: Science, v. 281, p. 1173-1175.
PAGE, A., GABBOTT, S.E., WILBY, P.R., and ZALASIEWICZ, J.A., 2008, Ubiquitous Burgess Shale-style "clay templates" in low-grade metamorphic mudrocks: Geology, v. 36, p. 855-858.
PARKER, J.C., and SIEGEL, R.W., 1990, Calibration of the Raman spectrum to the oxygen stoichiometry of nanophase TiO2: Applied Physics Letters, v. 57, p. 943-945.
SAPPENFIELD, A., DROSER, M.L., and GEHLING, J.G., 2011, Problematica, trace fossils, and tubes within the Ediacara Member (South Australia): redefining the Ediacaran trace fossil record one tube at a time: Journal of Paleontology, v. 85, p. 256-265.
SCHOPF, J.W., KUDRYAVTSEV, A.B., AGRESTI, D.G., CZAJA, A.D., and WDOWIAK, T.J., 2005, Raman imagery: a new approach to assess the geochemical maturity and biogenicity of permineralized Precambrian fossils: Astrobiology, v. 5, p. 333–371.
SEILACHER, A., 1992, Vendobionta and Psammocorallia: lost constructions of Precambrian evolution: Journal of the Geological Society of London, v. 149, p. 607-613.
SHEN, B., XIAO, S., DONG, L., ZHOU, C., and LIU, J., 2007, Problematic macrofossils from Ediacaran successions in the North China and Chaidam blocks: Implications for their evolutionary roots and biostratigraphic significance: Journal of Paleontology, v. 81, p. 1396-1411.
SPERLING, E.A., PETERSON, K.J., and LAFLAMME, M., 2011, Rangeomorphs, *Thectardis* (Porifera?) and dissolved organic carbon in the Ediacaran oceans: Geobiology, v. 9, p. 24-33.
VAN ROY, P., ORR, P.J., BOTTING, J.P., MUIR, L.A., VINTHER, J., LEFEBVRE, B., HARIRI, K., and BRIGGS, D.G., 2010, Ordovician faunas of Burgess Shale type: Nature, v. 465, p. 215-218.
WADA, N., and KAMITAKAHARA, W.A., 1991, Inelastic neutron- and Raman-scattering studies of muscovite and vermiculite layered silicates: Physical Review B, v. 45, p. 2391-2397.
WANG, A., FREEMAN, J., and KUEBLER, K.E., 2002, Raman Spectroscopic Characterization of Phyllosilicates: Lunar and Planetary Science, v. XXXIII, p. 1374-1375.
WEBER, B., STEINER, M., and ZHU, M.Y., 2007, Precambrian Cambrian trace fossils from the Yangtze Platform (South China) and the early evolution of bilaterian lifestyles: Palaeogeography Palaeoclimatology Palaeoecology, v. 254, p. 328-349.

WOPENKA, B., and PASTERIS, J.D., 1993, Structural characterization of kerogens to granulite-facies graphite: Applicability of Raman microprobe spectroscopy: American Mineralogists, v. 78, p. 533-557.
XIAO, S., and KNOLL, A.H., 2000, Phosphatized animal embryos from the Neoproterozoic Doushantuo Formation at Weng'an, Guizhou, South China: Journal of Paleontology, v. 74, p. 767-788.
XIAO, S., and LAFLAMME, M., 2009, On the eve of animal radiation: Phylogeny, ecology and evolution of the Ediacara biota: Trends in Ecology & Evolution, v. 24, p. 31-40.
XIAO, S., SCHIFFBAUER, J.D., MCFADDEN, K.A., and HUNTER, J., 2010, Petrographic and SIMS pyrite sulfur isotope analyses of Ediacaran chert nodules: Implications for microbial processes in pyrite rim formation, silicification, and exceptional fossil preservation: Earth and Planetary Science Letters, v. 297, p. 481-495.
XIAO, S., YUAN, X., STEINER, M., and KNOLL, A.H., 2002, Macroscopic carbonaceous compressions in a terminal Proterozoic shale: A systematic reassessment of the Miaohe biota, South China: Journal of Paleontology, v. 76, p. 347-376.
XING, Y., DING, Q., LUO, H., HE, T., and WANG, Y., 1984, The Sinian–Cambrian Boundary of China: Bulletin of the Institute of Geology, Chinese Academy of Geological Sciences, v. 10, p. 1-262.
YANG, S., and ZHENG, Z., 1985, The Sinian trace fossils from Zhengmuguan Formation of Helanshan Mountain, Ningxia: Earth Science - Journal of Wuhan College of Geology, v. 10, p. 9-10.
YUAN, X., CHEN, Z., XIAO, S., ZHOU, C., and HUA, H., 2011, An early Ediacaran assemblage of macroscopic and morphologically differentiated eukaryotes: Nature, v. 470, p. 390-393.
ZHANG, L., 1986, A discovery and preliminary study of the late stage of late Gaojiashan biota from Sinian in Ningqiang County, Shaanxi: Bulletin of the Xi'an Institute of Geology and Mineral Resources, Chinese Academy of Geological Sciences, v. 13, p. 67-88.
ZHOU, C., and XIAO, S., 2007, Ediacaran $\delta^{13}C$ chemostratigraphy of South China: Chemical Geology, v. 237, p. 89-108.
ZHU, M., BABCOCK, L.E., and STEINER, M., 2005, Fossilization modes in the Chengjiang Lagerstätte (Cambrian of China): testing the roles of organic preservation and diagenetic alteration in exceptional preservation: Palaeogeography, Palaeoclimatology, Palaeoecology, v. 220, p. 31-46.
ZHURAVLEV, A., GAMEZ VINTANED, J.A., and IVANTSOV, A.Y., 2009, First finds of problematic Ediacaran fossil *Gaojiashania* in Siberia and its origin: GEOLOGICAL MAGAZINE, v. 146, p. 775–780.

CHAPTER 4

TAPHONOMY OF THE EDIACARAN FOSSIL *PTERIDINIUM SIMPLEX* PRESERVED THREE-DIMENSIONALLY IN MASS FLOW DEPOSITS, NAMA GROUP, NAMIBIA

MIKE MEYER[1], DAVID ELLIOTT[2], JAMES D. SCHIFFBAUER[3], MICHAEL HALL[2], KARL H. HOFFMAN[4], GABI SCHNEIDER[4], PATRICIA VICKERS-RICH[2], SHUHAI XIAO[1]

[1] *Department of Geosciences, Virginia Tech, Blacksburg, Virginia, 24061, USA*

[2] *School of Geosciences, Monash University, Clayton, Victoria, 3800, Australia*

[3] *Department of Geological Sciences, University of Missouri, Columbia, Missouri, 65211, USA*

[4]*Geological Survey of Namibia, Windhoek, Namibia*

4.1 Abstract

Ediacara-type fossils are found in a diverse array of preservational styles, implyng that multiple taphonomic mechanisms might have been responsible for their preservational expression. For many Ediacara fossils, the "death mask" model has been invoked as the primary taphonomic pathway. The key to this preservational regime is the replication or sealing of sediments around the degrading organisms by microbially-induced precipitation of authigenic pyrite, leading toward fossil preservation *along* bedding planes. Nama-style preservation, on the other hand, captures Ediacaran organisms as molds and three-dimensional casts *within* coarse-grained mass flow beds, and has been previously regarded as showing little or no evidence of a microbial preservational influence. To further understand these two seemingly distinct taphonomic pathways, we set out to investigate the three-dimensionally preserved Ediacara fossil *Pteridinium simplex* from mass flow deposits of the upper Kliphoek Member (recently renamed as the Aar Member, Hall et al., submitted), Kuibis Subgroup, southern Namibia. Our analysis, using a combination of petrographic and micro-analytical methods, shows that *Pteridinium simplex* vanes are replicated with minor pyrite, but are most often represented by open voids that can be filled with secondary carbonate material; clay minerals are also found in association with the vanes, but their origin remains unresolved. The scarcity of pyrite and the development of voids are likely related to oxidative weathering, and it possible that microbial activities and authigenic pyrite may have contributed to the preservation of *Pteridinium simplex*; however, any microbes growing on *P. simplex* vanes *within* mass flow deposits were unlikely to have formed thick mats as envisioned in the death mask model. Differential weathering of replicating minerals

and precipitation of secondary minerals greatly facilitate fossil collection and morphological characterization by allowing *Pteridinium simplex* vanes to be parted from hosting massive sandstone.

4.2 Introduction

Ediacara fossils (580–542 Ma) are some of the earliest known complex multicellular life forms but have enigmatic taphonomic histories and phylogenies. Four preservational types, falling under the Ediacara-type preservation umbrella, have been described as the classic taphonomic modes of the Ediacaran Period. Flinders-style death-mask preservation, characteristic of most fossiliferous beds in the Flinders Ranges of South Australia and some facies in the White Sea Region of Russia, captured epibenthic organisms that lived in shallow, photic zone environments between normal and storm wave-base. This preservational regime was dependent on event deposition of storm beds and lithification aided by microbial communities (Gehling, 1999; Narbonne, 2005). Three-dimensional Nama-style preservation, characterisitic of the Kuibis and Schwarzrand subgroups of Namibia, entombed organisms *within* mass-flows or storm event sediments as opposed to preservation *under* event sediments at the base of the event bed (Jenkins, 1992; Narbonne, 2005; Vickers-Rich, 2007; Vickers-Rich et al., 2013b). Fermeuse-style preservation represents deeper water assemblages found in outer shelf, slope, or basinal paleoenvironments, and is known from the Fermeuse Formation of Newfoundland, the Windermere Supergroup of northwestern Canada, and the Innerelv Member of northern Norway (Narbonne and Hofmann, 1987; Farmer et al., 1992; Gehling et al., 2000). While Fermeuse-style preservation was previously suggested to

have less influence from microbial mats due to its deeper water paleoenvironmental setting (i.e., Narbonne, 2005), recent investigation shows the three-dimensional preservation of *Aspidella* by shrouds of fine-grained clays in a coarser-grained sandy matrix, interpreted as indicative of biofilm envelopes (Laflamme et al., 2011b). Finally, Conception-style preservation ("Ediacaran Pompeii") results from the burial of benthic organisms under volcanic ashes, as is observed in the Conception Group of Newfoundland and the Charnwood succession of England (Seilacher, 1992; Narbonne, 2005).

In addition to these "classic" styles, other preservational modes have also added important details to Ediacaran taphonomic descriptions. These include the three-dimensional pyritization of the Gaojiashan biota (Cai et al., 2010; Cai et al., 2012), aluminosilicification and kerogenization of the Gaojiashan, Dengying, and Doushantuo formations (Anderson et al., 2011; Cai et al., 2012; Meyer et al., 2012), three-dimensional phosphatization of cellularly preserved microfossils in the Doushantuo Formation (Xiao and Knoll, 2000; Xiao et al., 2002; Yuan et al., 2011a; Schiffbauer et al., 2012), as well as silicification of microfossils in Doushantuo chert nodules (Xiao et al., 2010a) of South China. While this diversity of preservational modes has greatly increased our understanding of Ediacaran biodiversity and ecology, the taphonomic processes of many Ediacaran fossil localities remain enigmatic.

One of the most important recent findings was the association of clay minerals in Ediacaran fossil preservation (Anderson et al., 2011; Laflamme et al., 2011b; Cai et al., 2012; Meyer et al., 2012), an association that has also been known from younger Phanerozoic Burgess Shale-type (BST) preservational windows although its origins are

much debated. For example, the association of clays with exceptionally preserved Ediacaran fossils have been previously documented in carbonaceous compressions in the Ediacaran successions of South China (Anderson et al., 2011; Cai et al., 2012; Meyer et al., 2012) and in *Aspidella* from the Fermeuse Formation in Newfoundland (Laflamme et al., 2011b). Debates, however, surround the origin of the clays and their possible constructive roles in exceptional preservation, particularly the preservation of BST fossils (Butterfield, 1990; 1995; Orr et al., 1998; Petrovich, 2001; Gaines et al., 2005; Butterfield et al., 2007; Gaines et al., 2008; Page et al., 2008). Because BST fossils are consistently found in fine-grained sediments and deeper water settings, it is important to know whether a clay association is also present in other taphonomic facies, for example in coarser-grained sediments deposited in shallow-water environments where Ediacara fossils are preserved three-dimensionally, and whether such clays are of detrital, authigenic, metamorphic, or weathering origin.

For many Ediacara fossils found in coarse- and fine-grained siliciclastic rocks, some variation of the death mask hypothesis (Gehling, 1999; Narbonne, 2005) has been invoked as the primary taphonomic pathway. This hypothesis proposes that authigenic pyrite precipitation just beneath microbial mats that colonized bedding surfaces can preserve both microbial mat texture (Gehling and Droser, 2009; Laflamme et al., 2011a) and organisms associated with the mat (Gehling, 1999). The death mask taphonomic process relies on storm events to smother and seal mat-associated benthos along a bedding surface, where bacterial sulfate reduction and reactive iron drive pyrite precipitation and hence fossil preservation. However, this model does not address how some Ediacara fossils, such as those in the Nama Group, are preserved in full three–

dimensionality *within* mass flow sediments (Crimes and Fedonkin, 1996; Grazhdankin and Seilacher, 2002; Elliott et al., 2011) and how they can be easily separated from the matrix to facilitate fossil collection.

To further explore how Ediacara fossils are preserved *within* mass flow sediments and how these three dimensionally preserved fossils can be removed from their matrix, we investigated the enigmatic Nama fossil *Pteridinium simplex* (Gürich, 1930) from the upper Kliphoek Member of the Kuibis Subgroup at Farm Aar of southern Namibia (Fig. 4.1.1). The genus *Pteridinium* has been found globally from numerous late Ediacaran sites (Glaessner, 1966; St. Jean, 1973; Keller et al., 1974; Gibson et al., 1984; Xiao and Laflamme, 2009; Laflamme et al., 2013b). It is characterized by three vanes that are joined along a seam, with the medial vane surrounded by two lateral vanes. In *P. simplex* these lateral vanes are often bent to form a boat-like structure (Fig. 4.1.2). Each of the three vanes consists of numerous segments ('quilts' and 'furrows' in Grazhdankin and Seilacher, 2002) that are interpreted as tubular structures (Seilacher, 1992). At Farm Aar, *P. simplex* fossils are preserved as three dimensional casts or molds within coarse-grained sandstone beds, interpreted as storm-induced density flow deposits that fill gutters and channels (Vickers-Rich et al., 2013b; Hall et al., *submitted*). There is very little organic matter associated with *P. simplex* fossils, possibly due to chemical weathering (Grazhdankin and Seilacher, 2002; Elliott et al., 2011). While *P. simplex* fossils are sometimes preserved on bedding surfaces and presumably as death masks (Fedonkin et al., 2007a), they are primarily preserved within massive sandstone beds (Jenkins et al., 1983; Hall et al., *submitted*). The unusual preservation of *P. simplex* and other Nama

fossils establishes their suitability as candidates to investigate mass flow taphonomy in comparison with other prevailing Ediacaran preservational modes.

4.3 Geological and Stratigraphic Background

The Kuibis Subgroup was deposited in a foreland basin on the northern side of the Kalahari Craton (Fig. 4.1.1) (Germs, 1973). Available radiometric dates constrain the Kuibis Subgroup to be older than 548.8±1 Ma (revised as 547.32 ± 0.65 Ma) (Grotzinger et al., 1995; Schmitz, 2012b). This foreland basin includes two subbasins, the northern Zaris and the southern Witputs subbasins, separated by the Osis arch (Gresse and Germs, 1993; Saylor et al., 1995). Our specimens were collected from the Witputs subbasin where the Kuibis Subgroup contains two formations: the Dabis and Zaris Formations. Here, the Kuibis Subgroup is characterized by feldspathic sandstone-orthoquartzite-limestone cycles, with limestones becoming more common up-section.

Our specimens come from the Kliphoek Member of the Dabis Formation. The lower Kliphoek Member is the last major sandstone unit of the afore-mentioned sandstone-limestone cycles before the beginning of the Schwarzrand Subgroup (Gresse and Germs, 1993; Saylor et al., 1995). The lower Kliphoek Member (or the Kliphoek sandstone; Fig. 4.1.1) consists of fine to coarse grained orthoquartzite, with coarser material found within mass flow deposits (Elliott et al., 2011), whereas the upper Kliphoek (Aar) Member (Hall et al., *submitted*) consists mainly of interbedded sandstones (1–2 m thick) and shales with a few limestone beds. The base of many Kliphoek Member sandstone beds are often characterized with scouring and tool marks, representing channel and gutter fills in shallow-water high-energy environments (Saylor

et al., 1995; Hall et al., *submitted*). The Kliphoek Member is directly overlain by bedded limestones of the Mooifontein Member, indicating a major marine transgression (Gresse and Germs, 1993).

The focus of this paper is on the upper Kliphoek Member, which was likely deposited in an extensive, sandy, braided fluvial to shallow marine system (Elliott et al., 2011; Hall et al., *submitted*), partly reworked into vast inter-tidal sand flats along a low gradient coastal plain. The upper Kliphoek (Aar) Member consists mainly of cross-bedded sandstones (1–2 m thick) interbedded with shale units. Shale interbeds found between the sandstones are interpreted as intertidal to shallow subtidal muds deposited during regional transgression. Individual sandstone beds range up to 35 cm in thickness, commonly showing thin laminations, occasionally with symmetric ripples, and sometimes containing pelloidal structures resembling rip-up clasts (Elliott et al., 2011). Sandstone beds in the upper Kliphoek Member typically have sharp bases and tops, and sometimes exhibit very low angle scouring of the underlying shale (Elliott et al., 2011; Hall et al., *submitted*). *Pteridinium simplex* fossils are found in these sandstone beds, particularly in the Aarhauser sandstone in the lower Aar Member (Hall et al., *submitted*).

4.4 Materials and Methods

Specimens examined here were collected from the upper Kliphoek Member of the Kuibis Subgroup, at Farm Aar of the Aus region of southern Namibia (Fig. 4.1.1). Rock specimens were analyzed using standard petrographic techniques (Fig. 4.2). Fossil specimens are reposited the Namibian Geological Survey, Windhoek. Our paleontological analysis focused on a hand sample (V-8-2009) that contains numerous

Pteridinium simplex specimens. This sample was cut into three slabs (labeled A–C in Fig. 4.3.1) perpendicular to the main axis/seam of the largest *P. simplex* specimen, which constitutes the main focus of this investigation. The lateral vanes and seam of the main specimen are exposed, but the medial vane is not exposed and visible only on cut surfaces (Fig. 4.3.3–3.4). As such, the medial vane provides an opportunity to analyze minimally weathered anatomical structures of *P. simplex*.

The cut slabs were polished and then analyzed using light microscopy (Fig. 4.4), scanning electron microscopy (SEM; Figs. 4.5–6), and laser Raman microspectroscopy (Fig. 4.7). SEM was conducted on an FEI Quanta 600 field emission environmental scanning electron microscope (ESEM) in both high- and low-vacuum modes. The choice of vacuum mode was directly related to specimen size, i.e., larger specimens were analyzed in low-vacuum mode as their profuse void space would have outgassed excessively in high-vacuum mode. Both secondary (topographic; SE) and backscattered (atomic number, or Z, contrast; BSE-Z) electron detectors were used in SEM analysis. Specimens analyzed in high-vacuum mode were sputter-coated with Au-Pd (approximately 5–7.5 nm thickness) using a Cressington 208HR high-resolution sputter-coater. Energy dispersive X-ray spectroscopic (EDS) point spectra (Table 4.1, Fig. 4.8) and elemental maps (Figs. 4.5–6) of fossils in polished cross-section were collected using an integrated Bruker AXS QUANTAX 400 with a high-speed silicon drift detector. Regardless of vacuum mode, identical operating conditions were maintained for all EDS analyses: 20 keV accelerating voltage, 5.0 spot size (unitless categorization of beam current and probe diameter), 11.5 mm working distance, and X-ray signal count-rates of 25–35 kilo-counts per second (the upper end of the range was captured in high-vacuum

mode and the lower end in low-vacuum mode). All elemental maps were acquired for 600 seconds live-time, and individual point spectra were collected for 100 seconds live-time. Elemental peaks from point spectra were identified and quantified (with zaf and Au-Pd coating corrections applied if applicable) using the Bruker Esprit 1.9.2 software.

Initial X-ray point spectra were collected from the vanes of *P. simplex* and surrounding matrix (both within and outside the space defined by the two lateral vanes). Elemental maps were subsequently generated for all elements found at >1% (normalized weight percentage; nwp) in point analyses (Table 4.1). While the topography of unpolished specimens can significantly affect EDS analysis and particularly elemental mapping, all of the analyzed slabs were finely polished, with the only topography resulting from interstitial pore spaces between quartz grains of the host rock.

To assist in mineral identification, fossil and matrix material were also analyzed using Raman microspectroscopy (Fig. 4.7), using a JY Horiba HR 800 UV spectrometer with a 244 nm laser (15 mW), a 2400 gr/mm grating, and a Symphony CCD detection system (LN_2 cooled, 2048 x 512 pixel). Spectra were collected at 300 seconds/scan using a 40× UV objective (4 μm laser spot size), and were baseline corrected using Labspec software.

4.5 Results

Examination of petrographic thin sections reveals a high degree of syntaxial quartz overgrowth on rounded quartz grains, forming primary cement (Fig. 4.2.1–2.4), as well as the presence of flaky micas which may cut through quartz crystals (Fig. 4.2.3–2.4). In thin section, the vanes of *P. simplex* are stylolitic in nature and do not cut across

grain boundaries (Fig. 4.2.1–2.2). The stylolitic vanes are opaque in transmitted light and appear to consist of a mixture of pyrite and organic matter.

Pteridinium simplex fossils in sample V-8-2009 are preserved as casts or molds in massive sandstone with vanes consisting of segments (represented by parallel lines or ridges) emanating perpendicularly from the central seam (Figs. 4.1.2, 3). These ridges become less prominent and eventually grade into a distinctive smooth surface farther away from the central seam (Fig. 4.3.1–3.2) (Jenkins, 1992; Crimes and Fedonkin, 1996; Grazhdankin and Seilacher, 2002; Elliott et al., 2011). *P. simplex* fossils are often found jumbled and twisted over each other, yet there is no evidence of torn, broken, or split specimens from visual inspection of the specimens.

Cross sections of the main specimen (Figs. 4.3.3–3.4, 4) reveal that both the lateral and medial vanes are easily visible in light and BSE-Z electron microscopy. While only separated by a few centimeters and part of the same specimen, the cross section seen in Fig. 4.4 shows a dramatically different vane morphology than that seen in Fig. 4.3.3–3.4. For example, the medial vane in Fig. 4.4 is much shorter than that in Fig. 4.3.3–3.4 and it splits into a Y-shape structure ~1 mm from the central seam.

The vanes are represented by voids, although sometimes rusty staining is present along the vanes (Fig. 4.4.2), presumably resulting from oxidative weathering of pyrite (Vickers-Rich et al., 2013b). Elemental mapping shows that these voids are often at least partially filled with carbonates (Figs. 4.5, 6.1, 6.3) and minor amount of flaky clay minerals (Fig. 6.2, 6.4). The carbonate precipitates can range from ~3 mm thick on exposed lateral vanes (Fig. 4.5.1, 5.3) to barely visible on unexposed medial vanes (Figs. 4.5.2, 5.4). Although they predominately follow the vanes, they can also be found in

cracks and pore spaces within the host-rock matrix (Fig. 4.6.4). Our examination of other specimens from the upper Kliphoek Member also shows the presence of carbonate precipitates on exposed surfaces (not necessarily vane surfaces) and in cracks.

EDS point spectral data indicate that the major elemental constituents of the host lithology and fossil material are silicon, carbon, oxygen, calcium, sulfur, and common aluminosilicate cations, including aluminum and potassium (Table 4.1). Minor constituents, accounting for a combined total of less than 2% (mean normalized weight percent), include iron, magnesium, and titanium. As expected for siliciclastic sediments, Si and O are the most abundant components of the rock matrix. EDS analysis of the secondary carbonate material reveals higher amounts of C, Ca, and Ti than any of the clay material. EDS data also show that material associated with vanes have a compositional departure from the micas in the matrix. Specifically, vane material exhibits higher levels of Fe and S, but lower levels of Al, Si, and K, than mica minerals in the matrix. The EDS data are consistent with evidence indicative of oxidative weathering of pyrite (Fig. 4.4.2) and the presence of carbonate and clay minerals associated with the vanes.

Raman spectral analysis shows differences between *P. simplex* vane material and surrounding matrix (Fig. 4.7). Both the matrix and vane material show a strong peak at ~465 cm^{-1}, reiterating the obvious presence of quartz, and minor peaks at ~700 cm^{-1} and 3620 cm^{-1}, which match the signals of many phyllosilicate minerals and related hydroxyl groups (Wada and Kamitakahara, 1991; McKeown et al., 1999; Wang et al., 2002). Some spectra of vane material also show strong peaks at ~1085 cm^{-1} and ~1580 cm^{-1},

characteristic of calcite and carbonaceous material, respectively (Nicola et al., 1976; Wopenka and Pasteris, 1993; Awonusi et al., 2007).

4.6 Discussion

A unique feature of the Nama fossils is their preservation as casts and molds *within* massive sandstone beds, which are interpreted as mass flow deposits. As such, their extraction from the rock matrix depends on subtle differences between the matrix and material replicating the fossils. Our analysis of *Pteridinium simplex* shows that its vanes are often represented by voids, which greatly facilitate the separation of *P. simplex* fossils from the matrix. Such voids are results of differential chemical weathering which lead to the preferential dissolution of primary minerals that replicated the vanes and the precipitation of secondary minerals following the vanes.

We interpret that the vanes of *Pteridinium simplex* were originally replicated by pyrite minerals. This inference is based on the presence of opaque material (possibly pyrite and/or organic matter) following the stylolitic vanes in thin sections (Fig. 4.2.1), as well as the presence of iron staining in some vanes (Fig. 4.4.2). The former presence of pyrite is also supported by the discovery of its oxidative weathering product, jarosite, in association with other Nama fossils such as *Rangea* (Vickers-Rich et al., 2013b; Hall et al., *submitted*). Thus, the death mask model of Gehling (1999) can be applied to explain the three-dimensional preservation of *P. simplex*, to the extent that bacterial sulfate reduction likely drove the precipitation of pyrite along degrading vanes. On the other hand, given the rapidity of mass flow deposition and the preservation *within* sediments, it is unlikely that thick microbial mats could have developed along *P. simplex* vanes, as

implied by the death mask model. As such, organic substrates for bacterial sulfate reduction (and hence pyrite precipitation on *P. simplex* vanes) mostly came from the vanes themselves, rather than thick microbial mats. A prediction of this interpretation is that the amount of pyrite produced would be limited, leading to only a thin pyrite coating on degrading *P. simplex* vanes. This prediction, along with the weathered nature of Nama fossils, can explain the rare occurrence of pyrite in association with *P. simplex*.

Calcite minerals found along *P. simplex* vanes are interpreted as secondary precipitates in voids which likely represent products from chemical weathering in an arid environment, similar to caliches. This interpretation is based on several observations. First, the Kliphoek sandstone is not primarily cemented by calcite; instead, it is cemented by syntaxial growth of quartz (Fig. 4.2.1–2.4). Therefore, void-filling calcite cements are most likely secondary. Second, the prominent presence of calcite on exposed lateral vanes and exposed rock surfaces is also consistent with secondary precipitation driven by evaporation in an arid environment. Ground water penetration through cracks and voids is probably responsible for the precipitation of thin carbonate layers associated with unexposed medial vanes and along cracks in the matrix.

Given the evidence for oxidative weathering of pyrite and secondary precipitation of calcite, it is possible the minor clay minerals found in association with *P. simplex* vanes (Fig. 4.6.2, 6.4) may also be secondary precipitates formed during chemical weathering. Certainly, such clays are different from diagenetic mica minerals (Fig. 4.2.3–2.4; Table 1), indicating different origins. Although detrital or authigenic clays may have played a constructive role in the preservation of Ediacaran fossils such as *Aspidella* (Laflamme et al., 2011b), *Conotubus* (Cai et al., 2012), and *Shaanxilithes* (Meyer et al.,

2012), the origin of clays in association with *P. simplex* vanes cannot be resolved with available data. Although we tentatively interpret them as weathering products, their preferential occurrence in association with minimally weathered medial vanes (Fig. 4.6.2, 6.4) also suggest that they could have been detrital or authigenic in origin and thus may have formed a physical template of the vanes. Regardless, although authigenic pyrite may have been important in the three-dimensional *preservation* of *Pteridinium simplex* in mass flow deposits, it is the differential weathering and precipitation of secondary minerals that facilitate fossil *recovery* and separation from massive sandstones.

4.7 Conclusions

The taphonomic style of *Pteridinium simplex*, three-dimensionally preserved *within* mass flow deposits of the upper Kliphoek Member in Farm Aar of southern Namibia, represents a departure from the classic 'death mask' preservation on bedding surfaces. However, there is evidence for minor pyrite in association with *P. simplex* vanes, indicating bacterial sulfate reduction and authigenic pyrite precipitation may have played a constructive role in fossil preservation. On the other hand, it is unlikely that thick microbial mats developed on *P. simplex* vanes preserved *within* mass flow sediments. Limited precipitation of authigenic pyrite and subsequent destruction by chemical weathering explain the dearth of pyrite in association with *P. simplex* vanes. Chemical weathering and differential oxidation of pyrite result in voids delineating *P. simplex* vanes and the precipitation of secondary minerals such as calcite. Thus, chemical weathering also plays a constructive role in facilitating fossil recovery and separation from massive hosting rocks. There are also minor clay minerals in association with *P.*

simplex vanes, particularly unexposed medial vanes; however, the origin of such clays is uncertain, and we tentatively interpret them as weathering products. Understanding the taphonomy of *P. simplex* will allow more detailed morphologic analyses using X-ray microCT techniques which can take advantage of the secondarily formed voids that define *P. simplex* vanes.

4.8 Acknowledgments

Financial support for this study was provided by National Science Foundation, NASA Exobiology and Evolutionary Biology Program, Virginia Tech Institute for Critical Technology and Applied Science Nanoscale Characterization and Fabrication Laboratory, the Paleontological Society, and the Society for Sedimentary Geology (SEPM), UNESCO's International Geosciences Program Projects 493 and 587, the National Geographic Society, and from both the international and national committees of the International Geoscience Programme (IGCP). We would like to thank the owners of Farm Aar, B. Boehm-Erni and the late B. Boehm, for granting access to fossil site. We would like to thank Charles Farley for technical assistance and our reviewers for constructive comments.

4.9 Table and Table Captions

Table 4.1. Elemental concentrations (in normalized weight percentages) from EDS point analyses of clays within *Pteridinium simplex* vanes, matrix micas, and infilling carbonate material. Spot # denotes location in sub-figure (e.g., *1.2* is spot 2 in subfigure *1* in the Supplemental Data Figure *1*).

Spot #	Spot Type	C	O	Mg	Al	Si	S	K	Ca	Ti	Fe	Total
1.1	Fossil Clay	3.9	56.6	0.0	3.0	34.4	0.0	1.3	0.3	0.1	0.4	100
1.2	Fossil Clay	8.9	54.5	0.0	0.8	34.7	0.0	0.7	0.0	0.1	0.2	100
1.3	Fossil Clay	8.4	55.0	0.0	0.7	35.2	0.0	0.6	0.0	0.1	0.0	100
1.4	Fossil Clay	11.7	51.9	0.0	0.6	35.0	0.0	0.7	0.0	0.1	0.0	100
2.2	Fossil Clay	0.0	59.7	0.0	16.4	1.2	1.2	0.0	0.0	0.0	21.6	100
3.2	Fossil Clay	0.0	56.8	0.3	0.1	1.4	39.6	0.0	0.0	0.4	1.4	100
3.3	Fossil Clay	0.0	58.6	0.0	0.3	2.2	37.9	0.0	0.0	1.0	0.0	100
4.2	Fossil Clay	0.0	50.4	0.9	0.0	9.8	27.2	0.0	0.0	11.8	0.0	100
5.2	Fossil Clay	8.3	50.7	0.4	7.3	25.2	0.0	3.1	3.7	0.4	0.8	100
5.3	Fossil Clay	8.7	47.7	0.4	7.2	29.7	0.0	3.9	1.5	0.0	1.0	100
5.4	Fossil Clay	5.8	51.8	0.2	5.7	21.3	3.5	1.4	9.7	0.0	0.6	100
5.6	Fossil Clay	6.9	53.1	0.2	8.8	23.2	5.8	1.3	0.7	0.0	0.0	100
7.3	Fossil Clay	0.0	48.6	0.9	13.6	24.6	0.2	7.6	0.8	0.8	3.0	100
7.4	Fossil Clay	0.0	45.6	0.6	12.2	28.5	0.1	8.3	0.8	0.6	3.5	100
Average ± standard error (1σ)		4.5 ± 1.2	52.8 ± 1.1	0.3 ± 0.1	5.5 ± 1.5	21.9 ± 3.5	8.2 ± 4	2.1 ± 0.7	1.2 ± 0.7	1.1 ± 0.8	2.3 ± 1.5	100 ± 0
2.1	Matrix Mica	0.2	60.9	0.0	13.8	22.7	0.0	1.8	0.7	0.0	0.0	100
2.3	Matrix Mica	0.1	59.8	0.0	0.8	38.5	0.0	0.7	0.2	0.0	0.0	100
4.1	Matrix Mica	6.7	50.2	0.4	10.5	24.4	0.0	4.8	1.9	0.6	0.7	100
6.1	Matrix Mica	0.0	47.9	0.2	10.5	33.2	0.0	5.4	0.5	0.0	2.4	100
6.2	Matrix Mica	0.0	51.7	0.5	14.8	23.0	0.1	7.2	0.5	0.0	2.3	100
8.5	Matrix Mica	0.0	44.7	0.0	14.8	30.3	0.0	8.1	0.9	0.4	0.8	100
Average ± standard error (1σ)		1.2 ± 1.1	52.5 ± 2.6	0.2 ± 0.1	10.9 ± 2.2	28.7 ± 2.6	0 ± 0	4.7 ± 1.2	0.8 ± 0.2	0.2 ± 0.1	1 ± 0.4	100 ± 0
3.1	Carbonate Material	6.4	51.9	0.0	0.8	21.3	0.0	0.3	1.3	18.0	0.0	100
3.4	Carbonate Material	5.8	51.8	0.2	5.7	21.3	3.5	1.4	9.7	0.0	0.6	100
3.5	Carbonate Material	10.6	51.6	0.3	3.1	20.2	0.0	0.7	13.5	0.0	0.0	100
3.6	Carbonate Material	6.9	53.1	0.2	8.8	23.2	5.8	1.3	0.7	0.0	0.0	100
3.7	Carbonate Material	8.6	49.2	0.3	9.6	23.5	6.1	1.6	1.1	0.0	0.0	100
4.3	Carbonate Material	10.2	50.5	0.3	2.8	17.8	0.0	0.8	17.4	0.0	0.0	100
5.5	Carbonate material	10.6	51.6	0.3	3.1	20.2	0.0	0.7	13.5	0.0	0.0	100
5.7	Carbonate material	8.6	49.2	0.3	9.6	23.5	6.1	1.6	1.1	0.0	0.0	100
Average ± standard error (1σ)		8.4 ± 0.7	51.1 ± 0.5	0.2 ± 0	5.4 ± 1.2	21.4 ± 0.7	2.7 ± 1.1	1.1 ± 0.2	7.3 ± 2.5	2.2 ± 2.2	0.1 ± 0.1	100 ± 0
		C	O	Mg	Al	Si	S	K	Ca	Ti	Fe	Total
Total average ± standard error (1σ) of all samples		4.9 ± 0.8	52.3 ± 0.8	0.2 ± 0	6.6 ± 1	23.2 ± 1.9	4.9 ± 2.1	2.3 ± 0.5	2.9 ± 0.9	1.2 ± 0.7	1.4 ± 0.8	100 ± 0

4.10 Figures and Figure Captions

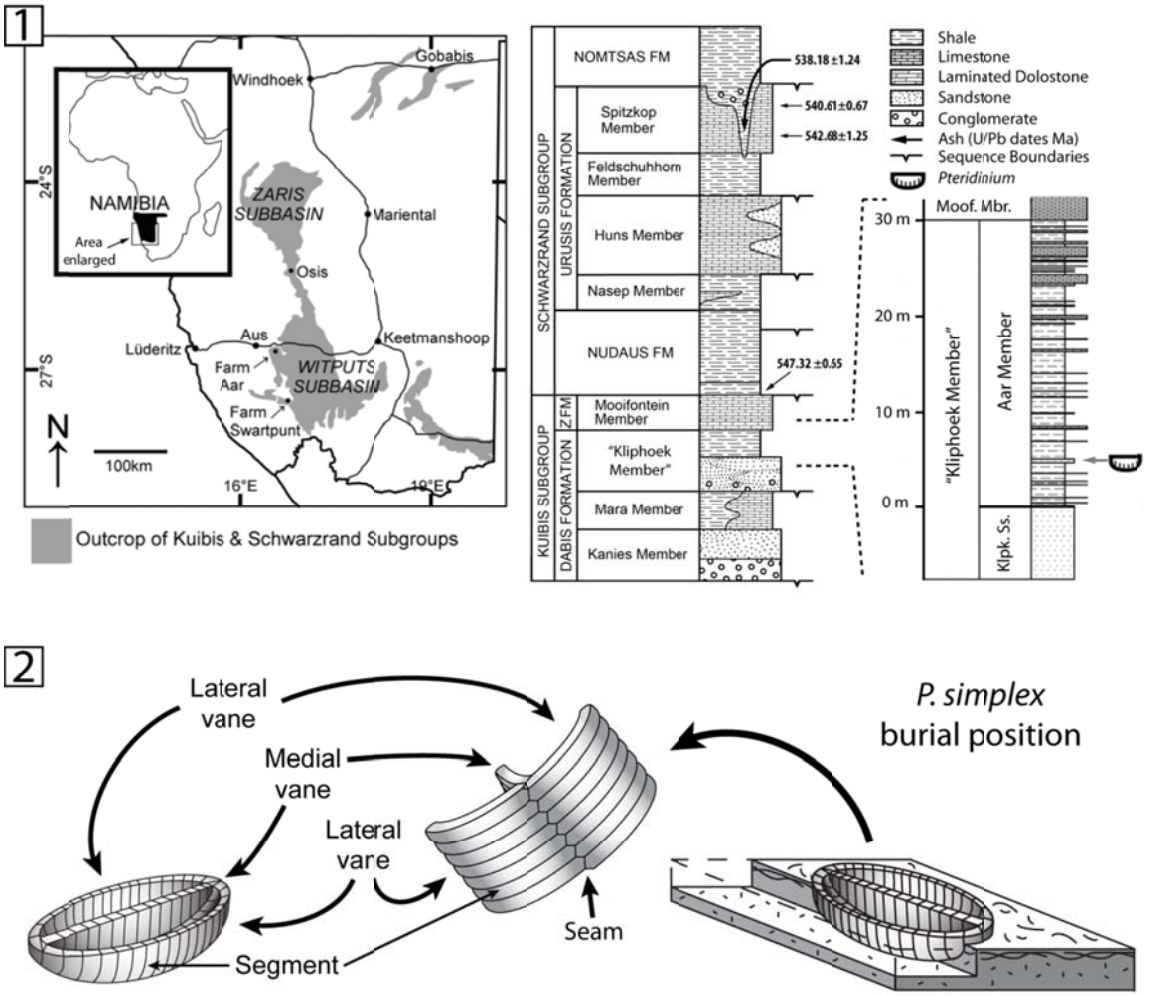

Figure 4.1. 1, Geological map of southern Namibia and stratigraphic column of the Nama Group, showing the fossil locality at Farm Aar and the fossil horizon in the upper Kliphoek (Aar) Member; modified from Elliot et al, 2011 and Vickers-Rich et al, 2013. *2*, *Pteridinium simplex* body construction and burial position.

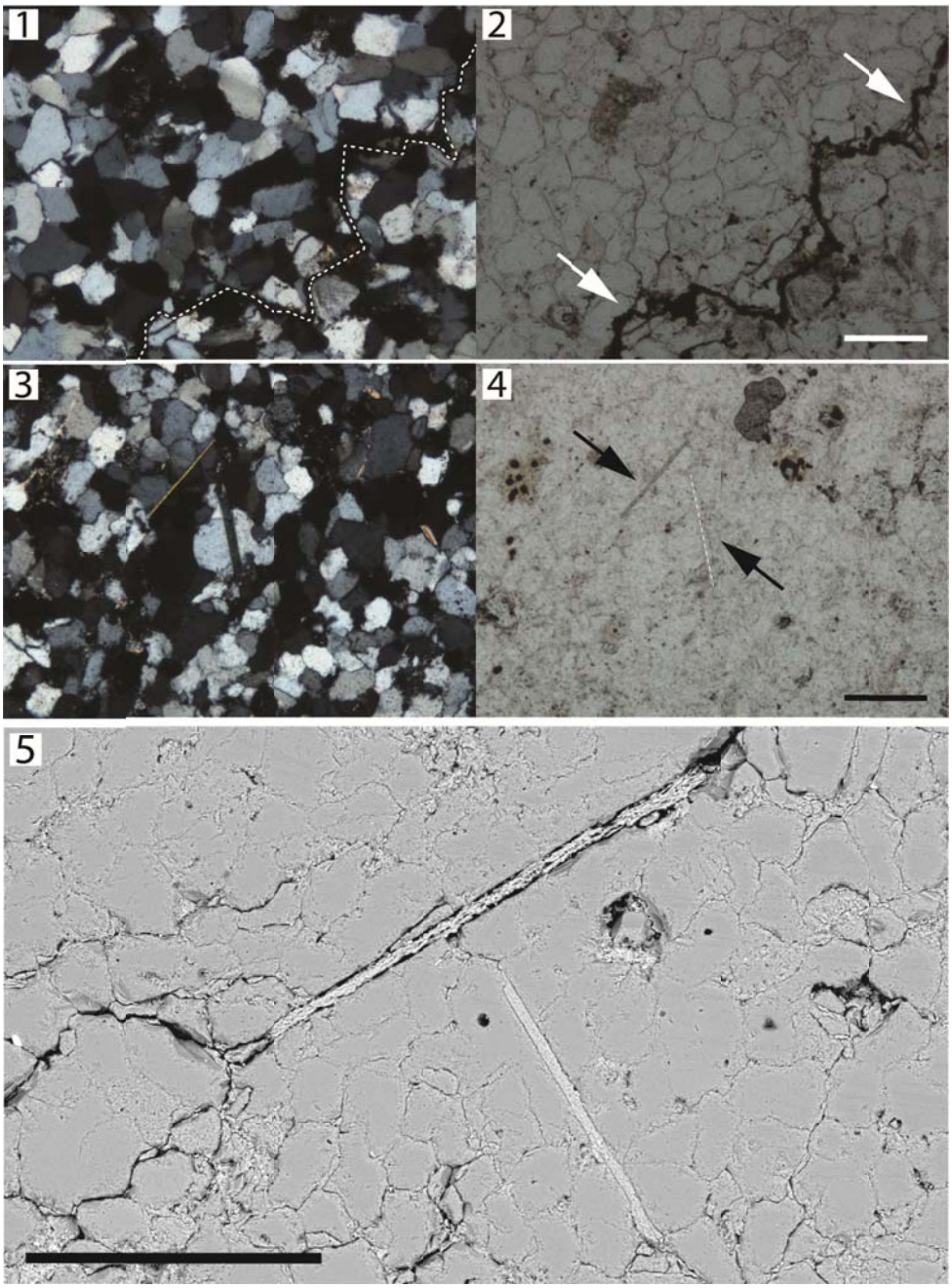

Figure 4.2. Thin section photomicrographs of *Pteridinium simplex* fossil and matrix. *1–2*, Cross-polarized and plane-polarized light photomicrographs of fossil and matrix, with dashed line and arrows denoting the vane of a fossil. *3–4*, Cross-polarized and plan-polarized light photomicrographs of matrix, with dashed line and arrows pointing to mica grains. *5*, BSE-Z image of two mica grains found in quartz sandstone matrix. Scale bar in *2* = 300 μm for *1–4*, and scale bar in *5* = 400 μm.

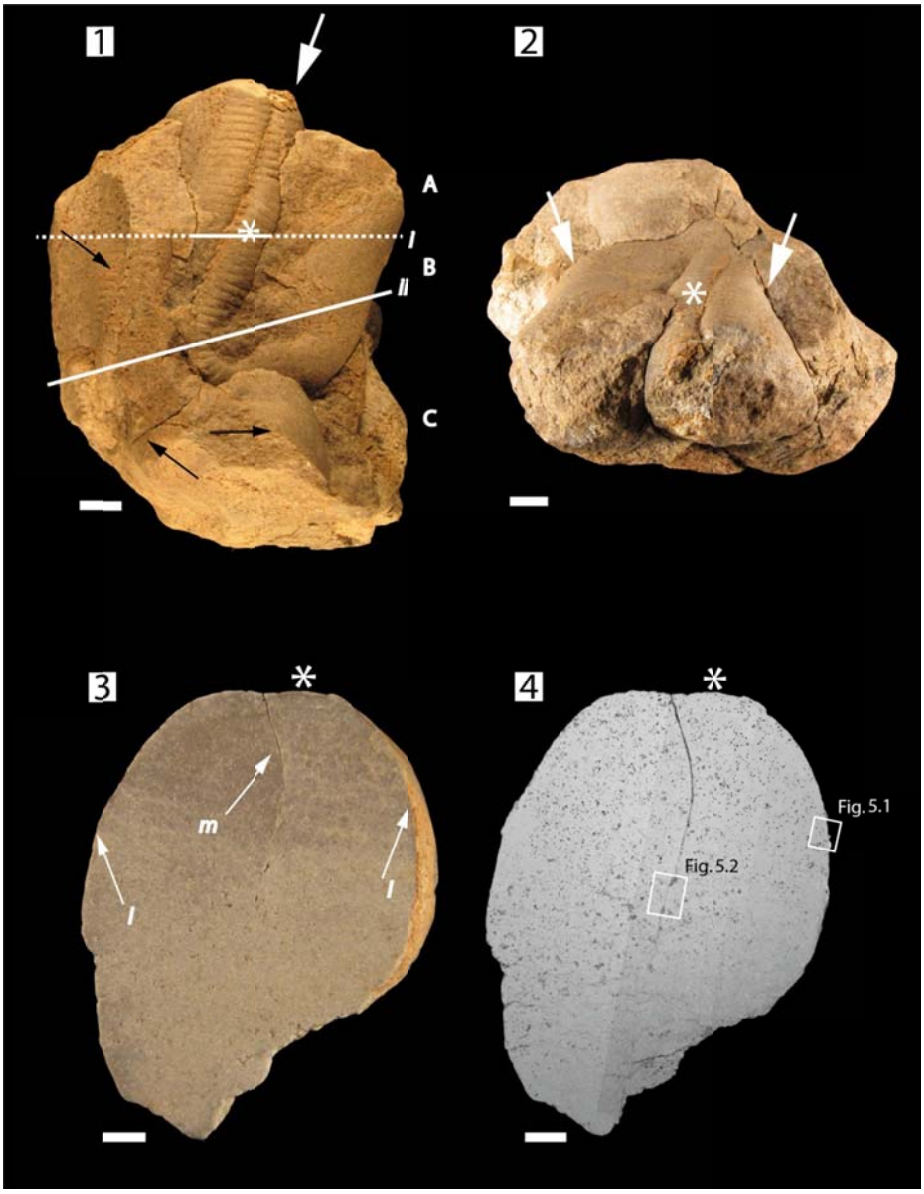

Figure 4.3. Light photographs (*1*–*3*) and BSE-Z image (*4*) of specimen V-8-2009 containing numerous *Pteridinium simplex* specimens. *1*, Hand sample with *P*. *simplex* specimens. White arrow points to main specimen in this study, while black arrows denote additional specimens. Letters A–C represent blocks between cuts represented by lines *i* and *ii*. Line *i* is solid where main specimen was cut, and this cut surface on Block B can be seen in *3* and *4*. *2*, Side view of block showing main specimen folded over (white arrows). Perspective is from white arrow in *1* looking toward the hand specimen. *3–4*, Light photography and BSE-Z image mosaics of cut surface *i* Block A. Arrows in *3* mark the medial vane (*m*) and lateral vanes (*l*). Labeled boxes in *4* represent mapped areas shown in Fig. *5*. Asterisks in *1–4* mark the same location to assist orientation. Scale bar = 1 cm for (*1–4*).

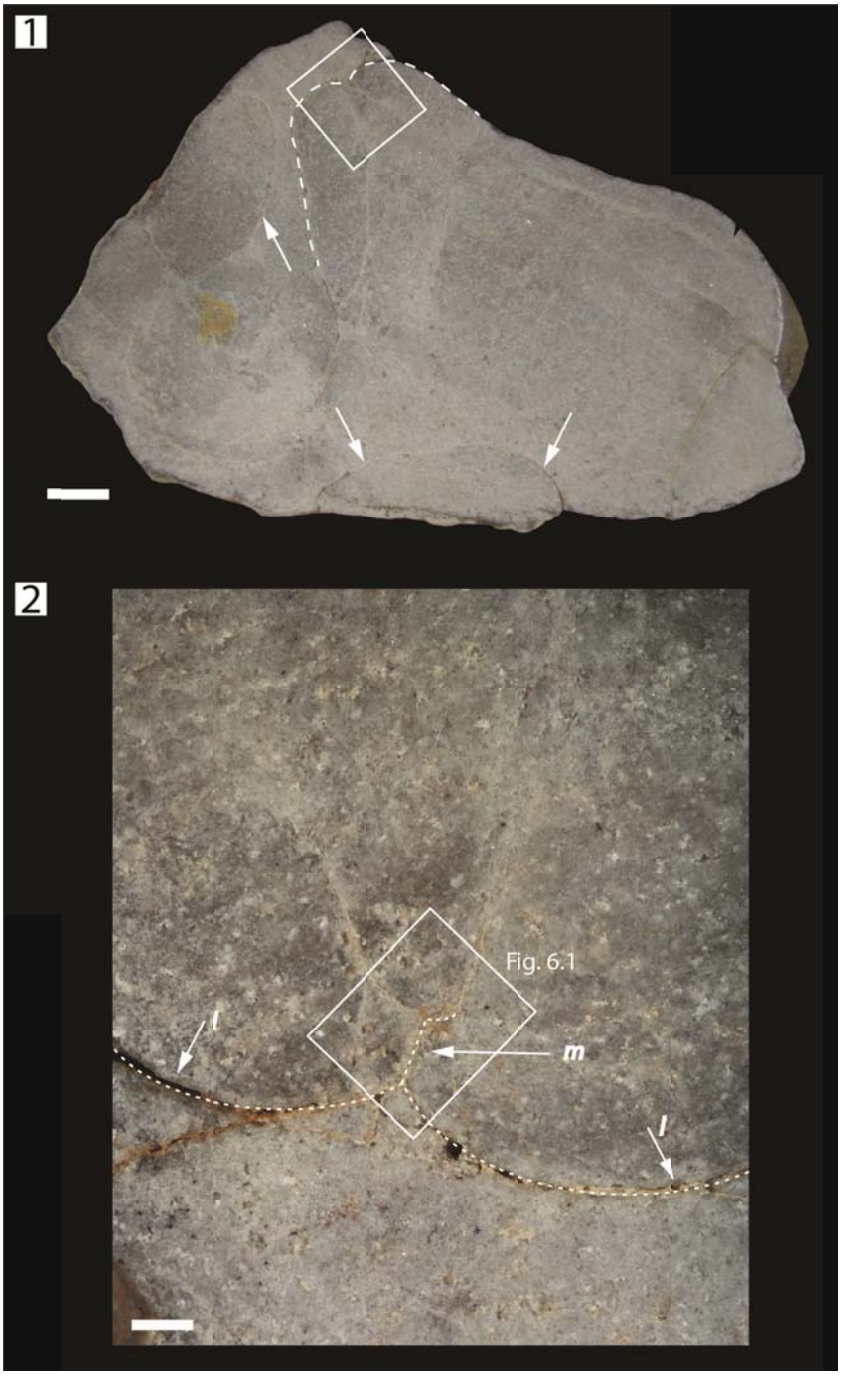

Figure 4.4. Light photograph (*1*) and photomicrograph (*2*) of cut surface *ii* on Block B (see Fig. *3.1*). Arrows in *1* denote other *P. simplex* specimens. Boxed area in *1* is magnified in *2*, with 135° counter-clockwise rotation. Dashed lines in *2* mark the medial vane (*m*) and lateral vanes (*l*) of the main specimen. Labeled box in *2* represents mapped area shown in Fig. *6.1*. Scale bar in *1* = 1 cm, in *2* = 500 µm.

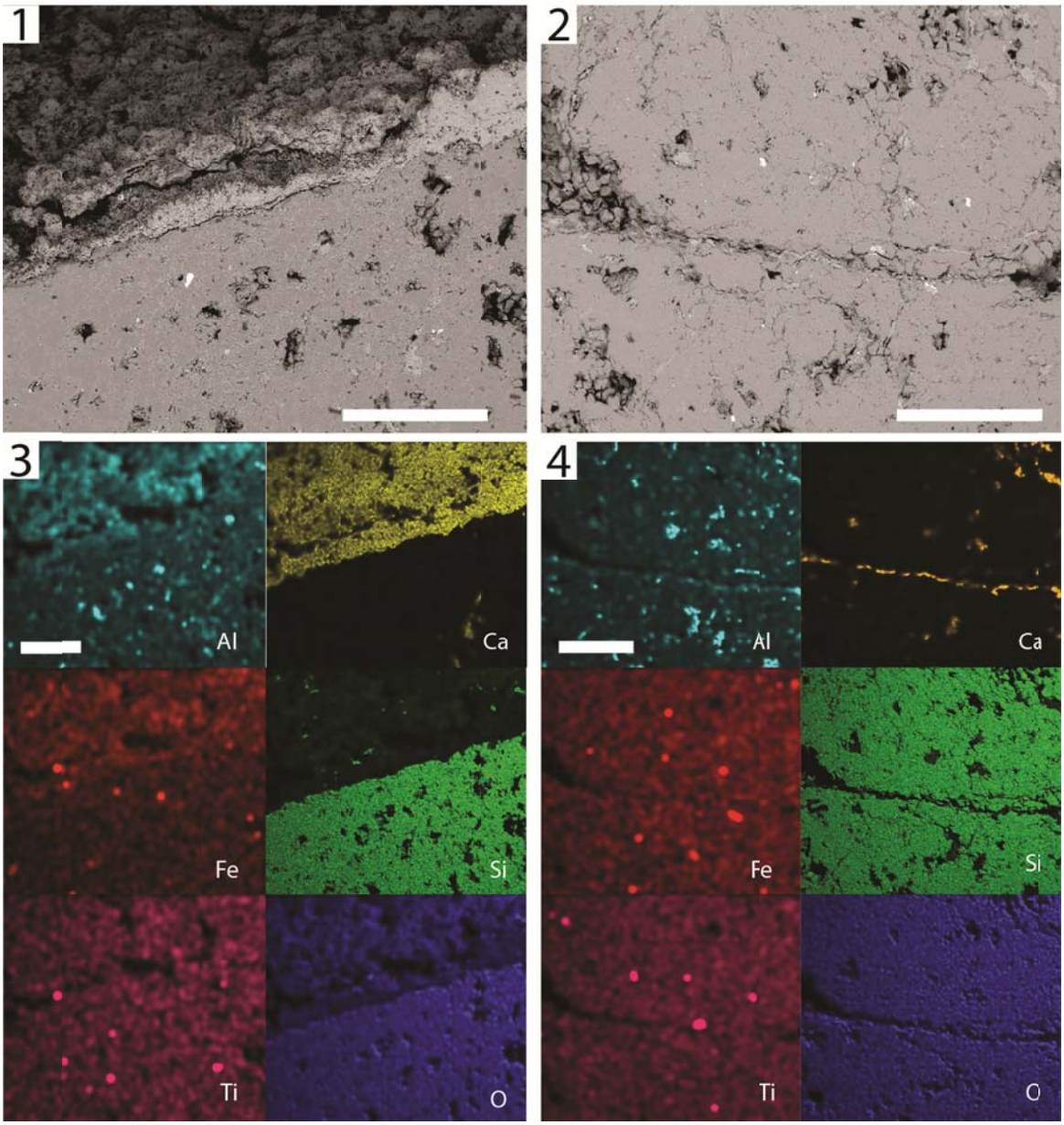

Figure 4.5. BSE-Z images and EDS elemental maps of *P. simplex* vanes. *1*, *3*, BSE-Z image and EDS elemental maps of labeled box in Fig. *3.4*, rotated 95° counter-clockwise. *2*, *4*, BSE-Z image and EDS elemental maps of labeled box in Fig. *3.4*, rotated 95° counter-clockwise. All scale bars = 1 mm.

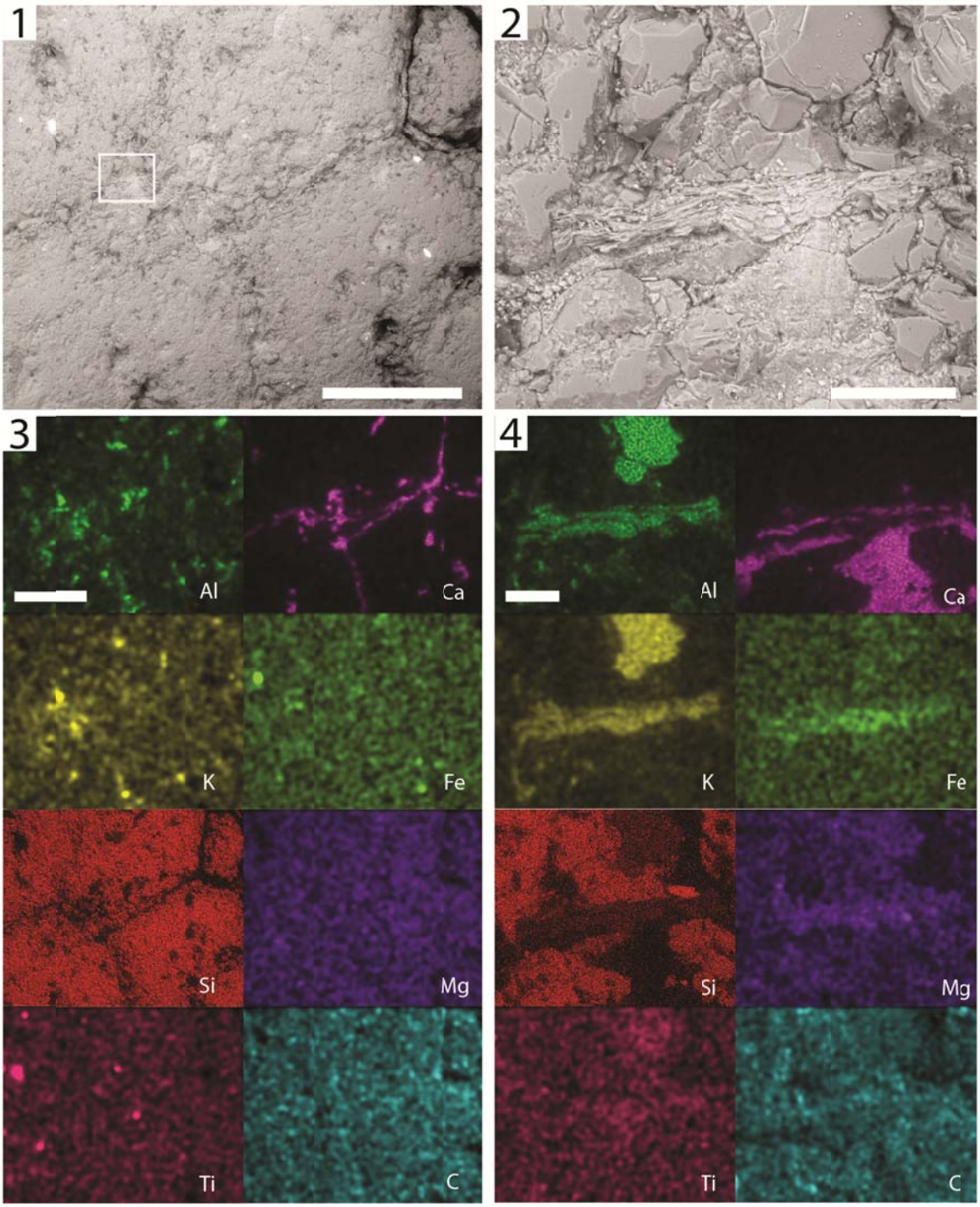

Figure 4.6. BSE-Z images and EDS elemental maps of *P. simplex* vanes. *1*, *3*, BSE-Z image and EDS elemental maps of boxed area in Fig. *4.2*), rotated 135° degrees counter-clockwise. *2*, *4*, BSE-Z image and EDS elemental maps of boxed area in *1*. Scale bars in *1–2* = 1 mm, scale bars in *3–4* = 100 µm.

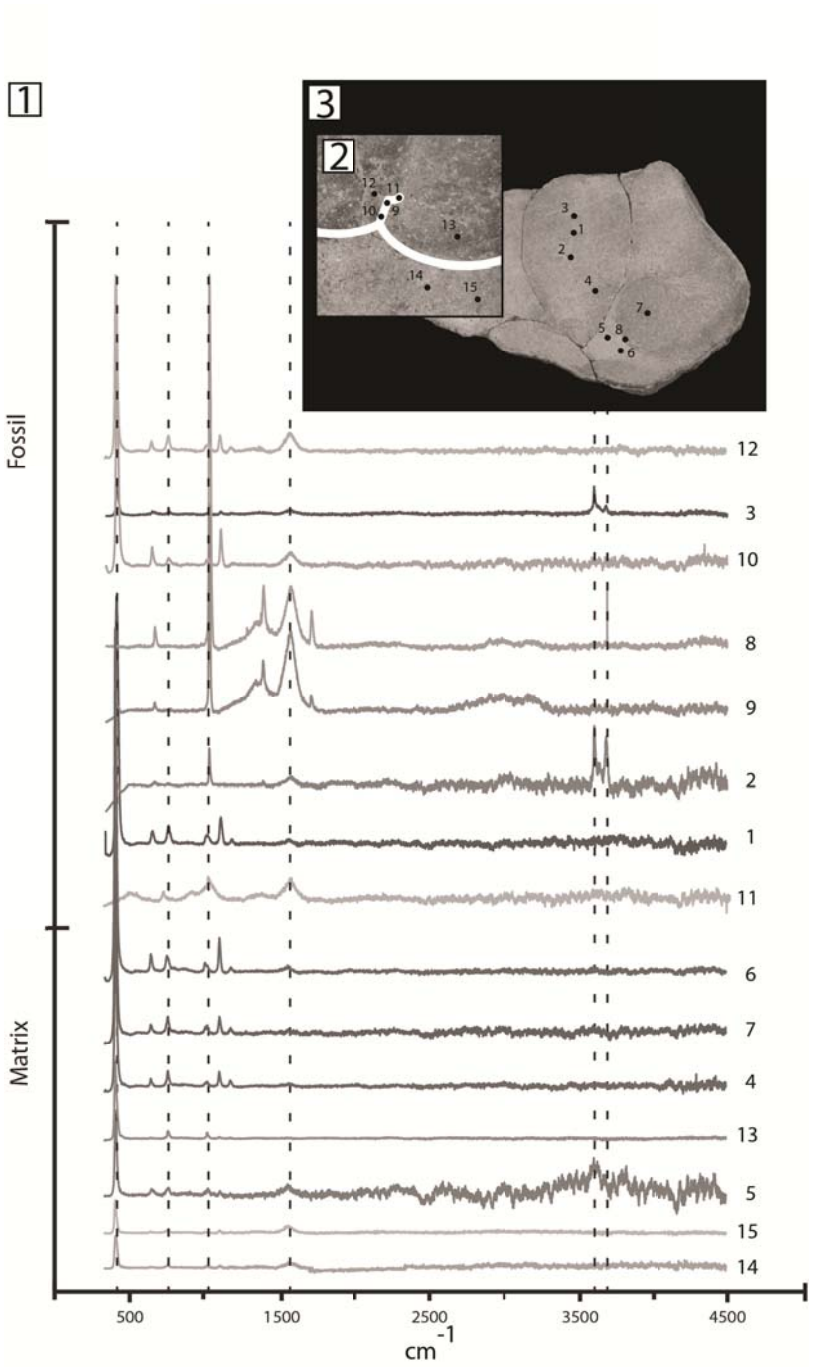

Figure 4.7. Raman spectra for fossil and matrix samples. *1*, Dashed lines are located approximately at 465, 700, 1085, 1580, 3620, and 3690 cm^{-1}. Analytical spots are marked on inset photographs (*2*–*3*). *2*, Magnified area from *2*, with white line marking fossil vanes. *3*, Block B, cut *i*.

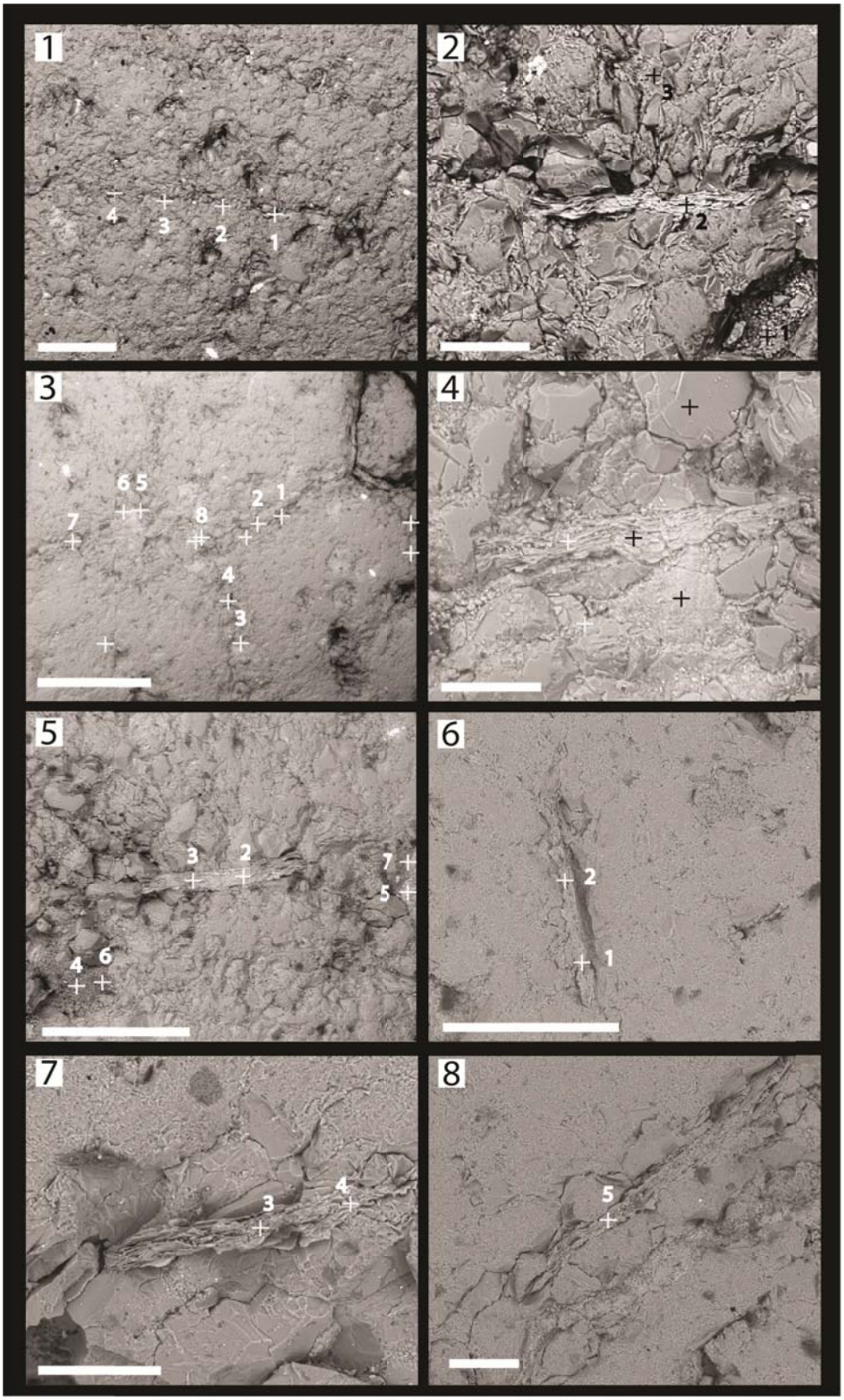

Figure 4.8. BSE-Z images showing locations of EDS point analyses on *P. simplex* vanes and matrix. Data are shown in Table 1. Scale bar in *1* = 500 µm, scale bar in *2* = 100 µm, scale bars in *3–4* = 1 mm, scale bars in *5–6* = 400 µm, and scales bars for *7–8* = 100 µm.

4.11 References

ANDERSON, E., J. D. SCHIFFBAUER, and S. XIAO. 2011. Taphonomic study of organic-walled microfossils confirms the importance of clay minerals and pyrite in Burgess Shale-type preservation. Geology, 39:643-646.

AWONUSI, A., M. D. MORRIS, and M. M. J. TECKLENBURG. 2007. Carbonate Assignment and calibration in the Raman Spectrum of Apatite. Calcified Tissue International, 81:46-52.

BUTTERFIELD, N. J. 1990. Organic preservation of non-mineralizing organisms and the taphonomy of the Burgess Shale. Paleobiology, 16:272-286.

BUTTERFIELD, N. J. 1995. Secular distribution of Burgess Shale-type preservation. Lethaia, 28:1-13.

BUTTERFIELD, N. J., U. BALTHASAR, and L. A. WILSON. 2007. Fossil diagenesis in the Burgess Shale. Palaeontology, 50:537–543.

CAI, Y., H. HUA, S. XIAO, J. D. SCHIFFBAUER, and P. LI. 2010. Biostratinomy of the late Ediacaran pyritized Gaojiashan Lagerstätte from southern Shaanxi, south China: Importance of event deposits. Palaios, 25:487-506.

CAI, Y., J. D. SCHIFFBAUER, H. HUA, and S. XIAO. 2012. Preservational modes in the Ediacaran Gaojiashan Lagerstätte: Pyritization, aluminosilicification, and carbonaceous compression. Palaeogeography Palaeoclimatology Palaeoecology, 326-328:109-117.

CRIMES, T. P. and M. A. FEDONKIN. 1996. Biotic changes in platform communities across the Precambrian-Phanerozoic boundary. Rivista Italiana di Paleontologia e Stratigrafia, 102:317-332.

ELLIOTT, D. A., P. VICKERS-RICH, P. TRUSLER, and M. HALL. 2011. New evidence on the taphonomic context of the Ediacaran *Pteridinium*. Acta Palaeontologica Polonica, 56:641-650.

FARMER, J., G. VIDAL, M. MOCZYDLOWSKA, H. STRAUSS, P. AHLBERG, and A. SIEDLECKA. 1992. Ediacaran fossils from the Innerelv Member (late Proterozoic) of the Tanafjorden area, northeastern Finnmark. Geological Magazine, 129:181-195.

FEDONKIN, M. A., J. G. GEHLING, K. GREY, G. M. NARBONNE, and P. VICKERS-RICH. 2007. The Rise of Animals: Evolution and Diversification of the Kingdom Animalia. Johns Hopkins University Press, Baltimore, 326 p.

GAINES, R. R., D. E. G. BRIGGS, and Y. L. ZHAO. 2008. Cambrian Burgess Shale-type deposits share a common mode of fossilization. Geology, 36:755-758.

GAINES, R. R., M. J. KENNEDY, and M. L. DROSER. 2005. A new hypothesis for organic preservation of Burgess Shale taxa in the middle Cambrian Wheeler Formation, House Range, Utah. Palaeogeography, Palaeoclimatology, Palaeoecology, 220:193-205.

GEHLING, J. G. 1999. Microbial mats in terminal Proterozoic siliciclastics: Ediacaran death masks. Palaios, 14:40-57.

GEHLING, J. G. and M. L. DROSER. 2009. Textured organic surfaces associated with the Ediacara biota in South Australia. Earth Science Reviews, 96:196-206.

GEHLING, J. G., G. M. NARBONNE, and M. M. ANDERSON. 2000. The first named Ediacaran body fossil, *Aspidella terranovica*. Palaeontology, 43:427-456.

GERMS, G. J. B. 1973. The Nama Group in South-West Africa and its relationship to the pan-African geosyncline. The Journal of Geology, 82:301-317.
GIBSON, G. G., S. A. TEETER, and M. A. FEDONKIN. 1984. Ediacarian fossils from the Carolina slate belt, Stanly County, North Carolina. Geology, 12:387-390.
GLAESSNER, M. F. W., MARY. 1966. The late Precambrian fossils from Ediacara, South Australia. Palaeontology, 9:599-628.
GRAZHDANKIN, D. and A. SEILACHER. 2002. Underground Vendobionta from Namibia. Palaeontology, 45:57-78.
GRESSE, P. G. and G. J. B. GERMS. 1993. The Nama foreland basin: sedimentation, major unconformity bounded sequences and multisided active margin advance. Precambrian Research, 63:247-272.
GROTZINGER, J. P., S. A. BOWRING, B. Z. SAYLOR, and A. J. KAUFMAN. 1995. Biostratigraphic and geochronologic constraints on early animal evolution. Science, 270:598-604.
GÜRICH, G. 1930. Die bislang ältesten Spuren von Organismen in Südafrika. International Geological Congress. South Africa, 1929 (XV), 2:670-680.
HALL, M., A. J. KAUFMAN, P. VICKERS-RICH, N. GUY, A. Y. IVANSTOV, P. TRUSLER, U. LINNEMANN, M. HOFMANN, D. A. ELLIOTT, H. CUI, M. A. FEDONKIN, K. HOFFMAN, S. A. WILSON, G. SCHNEIDER, and J. SMITH. *submitted*. Changing environments and their impact on metazoan evolution and preservation during the terminal Proterozoic in african Gondwana. Precambrian Research, xxx:xxx.
JENKINS, R. J. F. 1992. Functional and ecological aspects of Ediacaran assemblages, p. 131-176. *In* J. H. Lipps and P. W. Signor (eds.), Origin and Early Evolution of Metazoa. Plenum Press, New York.
JENKINS, R. J. F., C. H. FORD, and J. G. GEHLING. 1983. The Ediacara member of the Rawnsley quartzite: the context of the Ediacara assemblage (late Precambrian, Flinders Ranges). Journal of the Geological Society of Australia 30.
KELLER, B. M., V. V. MENNER, V. A. STEPANOV, and N. M. CHUMAKOV. 1974. New findings of Metazoan in the Vendian of the Russian Platform. Izvestiya Akademii Nauk SSSR, Seriya Geologicheskaya, 12:130-134.
LAFLAMME, M., S. A. F. DARROCH, S. M. TWEEDT, K. J. PETERSON, and D. H. ERWIN. 2013. The end of the Ediacara biota: Extinction, biotic replacement, or Cheshire Cat? Gondwana Research, 23:558-573.
LAFLAMME, M., J. D. SCHIFFBAUER, and G. M. NARBONNE. 2011a. Deep-water microbially induced sedimentary structures (MISS) in deep time: The Ediacaran fossil *Ivesheadia*, p. 111-123. *In* N. Noffke and H. S. Chafetz (eds.), Microbial mats in siliciclastic depositional systems through time.Volume 101. SEPM Special Publications.
LAFLAMME, M., J. D. SCHIFFBAUER, G. M. NARBONNE, and D. G. BRIGGS. 2011b. Microbial biofilms and the preservation of the Ediacara biota. Lethaia, 44:203-213.
MCKEOWN, D. A., M. I. BELL, and E. S. ETZ. 1999. Vibrational analysis of the dioctahedral mica: $2M_1$ muscovite. American Mineralogist, 84:1041-1048.
MEYER, M., J. D. SCHIFFBAUER, S. XIAO, Y. CAI, and H. HUA. 2012. Taphonomy of the upper Ediacaran enigmatic ribbonlike fossil *Shaanxilithes*. Palaios, 27:354-372.

NARBONNE, G. M. 2005. The Ediacara Biota: Neoproterozoic origin of animals and their ecosystems. Annual Review of Earth and Planetary Sciences, 33:421-442.
NARBONNE, G. M. and H. J. HOFMANN. 1987. Ediacaran biota of the Wernecke Mountains, Yukon, Canada. Palaeontology, 30:647-676.
NICOLA, J. H., J. F. SCOTT, R. M. COUTO, and M. M. CORREA. 1976. Raman spectra of Dolomite [$CaMg(CO_3)_2$]. Physical Review B, 14:4676-4678.
ORR, P. J., D. E. G. BRIGGS, and S. L. KEARNS. 1998. Cambrian Burgess Shale animals replicated in clay minerals. Science, 281:1173-1175.
PAGE, A., S. E. GABBOTT, P. R. WILBY, and J. A. ZALASIEWICZ. 2008. Ubiquitous Burgess Shale-style "clay templates" in low-grade metamorphic mudrocks. Geology, 36:855-858.
PETROVICH, R. 2001. Mechanisms of fossilization of the soft-bodied and lightly armored faunas of the Burgess Shale and of some other classical localities. American Journal of Science, 301:683-726.
SAYLOR, B. Z., A. J. KAUFMAN, J. P. GROTZINGER, and F. URBAN. 1995. Sequence stratigraphy and sedimentology of the Neoproterozoic Kuibis and Schwarzrand Subgroups (Nama Group), southwestern Namibia. Precambrian Research, 73:153-171.
SCHIFFBAUER, J. D., S. XIAO, K. SEN SHARMA, and G. WANG. 2012. The Origin of intracellular structures in Ediacaran metazoan embryos. Geology, 40:223-226.
SCHMITZ, M. D. 2012. Appendix 2—Radiometric ages used in GTS2012, p. 1045–1082. *In* F. Gradstein, J. Ogg, M. D. Schmitz, and G. Ogg (eds.), The Geologic Time Scale 2012. Elsevier, Boston.
SEILACHER, A. 1992. Vendobionta and Psammocorallia: lost constructions of Precambrian evolution. Journal of the Geological Society of London, 149:607-613.
ST. JEAN, J. 1973. A new Cambrian trilobite from the Piedmont of North Carolina. American Journal of Science, 273-A:196-216.
VICKERS-RICH, P. 2007. The Nama fauna of southern Africa, p. 69-88, The Rise of Animals: Evolution and Diversification of the Kingdom Animalia. Johns Hopkins University Press.
VICKERS-RICH, P., A. Y. IVANTSOV, P. W. TRUSLER, G. M. NARBONNE, M. HALL, S. A. WILSON, C. GREENTREE, M. A. FEDONKIN, D. A. ELLIOTT, K. H. HOFFMANN, and G. I. C. SCHNEIDER. 2013. Reconstructing *Rangea*: new discoveries from the Ediacaran of southern Namibia. Journal of Paleontology, 87:1-15.
WADA, N. and W. A. KAMITAKAHARA. 1991. Inelastic neutron- and Raman-scattering studies of muscovite and vermiculite layered silicates. Physical Review B, 45:2391-2397.
WANG, A., J. FREEMAN, and K. E. KUEBLER. 2002. Raman Spectroscopic Characterization of Phyllosilicates. Lunar and Planetary Science, XXXIII:1374-1375.
WOPENKA, B. and J. D. PASTERIS. 1993. Structural characterization of kerogens to granulite-facies graphite: Applicability of Raman microprobe spectroscopy. American Mineralogists, 78:533-557.

XIAO, S. and A. H. KNOLL. 2000. Phosphatized animal embryos from the Neoproterozoic Doushantuo Formation at Weng'an, Guizhou, South China. Journal of Paleontology, 74:767-788.

XIAO, S. and M. LAFLAMME. 2009. On the eve of animal radiation: Phylogeny, ecology and evolution of the Ediacara biota. Trends in Ecology & Evolution, 24:31-40.

XIAO, S., J. D. SCHIFFBAUER, K. A. MCFADDEN, and J. HUNTER. 2010. Petrographic and SIMS pyrite sulfur isotope analyses of Ediacaran chert nodules: Implications for microbial processes in pyrite rim formation, silicification, and exceptional fossil preservation. Earth and Planetary Science Letters, 297:481–495.

XIAO, S., X. YUAN, M. STEINER, and A. H. KNOLL. 2002. Macroscopic carbonaceous compressions in a terminal Proterozoic shale: A systematic reassessment of the Miaohe biota, South China. Journal of Paleontology, 76:347-376.

YUAN, X., Z. CHEN, S. XIAO, C. ZHOU, and H. HUA. 2011. An early Ediacaran assemblage of macroscopic and morphologically differentiated eukaryotes. Nature, 470:390-393.

CHAPTER 5

THREE DIMENSIONAL MICROCT ANALYSIS OF THE EDIACARA FOSSIL *PTERIDINIUM SIMPLEX* SHEDS NEW LIGHT ON ITS ECOLOGY AND PHYLOGENETIC AFFINITY

MIKE MEYER[A], DAVID ELLIOTT[B], ANDREW D. WOOD[C], NICHOLAS F. POLYS[C], MATTHEW COLBERT[D], JESSICA A. MAISANO[D], MICHAEL HALL[B], KARL H. HOFFMAN[E], GABI SCHNEIDER[E], PATRICIA VICKERS-RICH[B], SHUHAI XIAO[A]

[A]*Department of Geosciences, Virginia Tech, Blacksburg, Virginia, 24061, USA*

[B]*School of Geosciences, Monash University, Clayton, Victoria, 3800, Australia*

[C]*Advanced Research Computing, Virginia Tech, Blacksburg, VA, USA*

[D]*Jackson School of Geosciences, The University of Texas Austin, Texas 78712, USA*

[E]*Geological Survey of Namibia, Windhoek, Namibia,*

5.1 Abstract

Ediacara fossils often exhibit enigmatic taphonomy that complicates morphological characterization and ecological and phylogenetic interpretation; such is the case with *Pteridinium simplex* from the late Ediacaran Kliphoek Member in southern Namibia. *P. simplex* is often preserved as three-dimensional (3D) casts and molds in coarse-grained quartzites, making detailed morphological characterization difficult. In addition, *P. simplex* is often transported, distorted, and embedded in gutter fills or channel deposits, further obscuring its morphologies. By utilizing microfocus X-ray computed tomography (microCT) techniques, we are able to trace individual specimens and their vanes in order to digitally restore the 3D morphology of this enigmatic fossil. Our analysis shows that *P. simplex* has a very flexible integument that can be bent, folded, twisted, stretched, and torn, indicating a certain degree of elasticity. We find no evidence for vane identity change or penetrative growth that were previously used as evidence to support a fully endobenthic lifestyle of *P. simplex*; instead, the traditional interpretation of a semi-endobenthic or epibenthic lifestyle is favored. The elastic integument of *P. simplex* is inconsistent with a phylogenetic affinity with xenophyophore protists; instead, its physical property is consistent with the presence of collagen and cellulose, an inference that would provide constraints on the phylogenetic affinity of *P. simplex*.

5.2 Introduction

Ediacara-type fossils (580–542 Ma) represent the earliest-known complex multicellular organisms in the fossil record (Narbonne, 2005; Xiao and Laflamme, 2009), but

understanding their phylogenic placement has been impeded by their unusual taphonomy (Gehling, 1999; Laflamme et al., 2011b; Cai et al., 2012; Schiffbauer and Laflamme, 2012) and the lack of morphological analogs among extant taxa (Seilacher et al., 2003; Laflamme et al., 2013a). Among all Ediacara fossils, the genus *Pteridinium* (Gürich, 1930), first described from the Nama Group in southern Namibia (Fig. 5.1*A*), best encapsulates these two confounding factors (Fedonkin et al., 2007a). *Pteridinium* has a unique body plan (Fig. 5.1*B*), consisting of three vanes which are connected along an axis known as the 'seam'. Each vane is made of a single row (or possibly two overlapping rows) of segments that are attached to the seam (Jenkins, 1992). *Pteridinium* can be preserved in 2D on bedding surfaces or in 3D within massive quartzite, resulting in multiple taphomorphs. When preserved in 3D, *Pteridinium* specimens are often jumbled within mass flow deposits, with their morphology strongly modified and difficult to interpret (Grazhdankin and Seilacher, 2002; Elliott et al., 2011).

The unusual morphology and non-actualistic taphonomy of *Pteridinium* have led to various ecological and phylogenetic interpretations. It has been interpreted as a frondose epibenthic organism similar to *Charniodiscus* (Glaessner and Daily, 1959), a semi-endobenthic organism similar to *Ernietta (Fedonkin et al., 2007a)*, or a fully endobenthic organism that lived entirely within sediments (Grazhdankin and Seilacher, 2002). The phylogenetic affinity of *Pteridinium* has also been a matter of intense debate; it has been interpreted as a colonial organism (Pflug, 1994), a giant single-celled protist similar to modern xenophyophores (Seilacher et al., 2003), a lichen (Retallack, 1994), or an animal (Glaessner, 1984).

Central to the current debate on the ecology and phylogenetic affinity of *Pteridinium* is a better understanding of its taphonomy and morphology. For example, the fully endobenthic interpretation rests on convoluted *P. simplex* specimens with their vanes growing in sediments, penetrating each other, and switching identities (e.g., lateral vane changing to medial vane when organism is twisted) (Grazhdankin and Seilacher, 2002). However, these features are difficult to resolve without a 3D understanding of the fossils, and it is thus difficult to rule out the possibility that some of these features may result from taphonomic alteration. Thus, to better characterize the 3D morphology of *P. simplex* and to shed light on its taphonomy, ecology, and phylogenic affinity, we examined a single hand sample using microfocus X-ray computed tomography (microCT).

5.3 Ecological and Stratigraphic Background

The analyzed hand sample was collected from the upper Kliphoek Member of the Dabis Formation, Kuibis Subgroup, located at Aar Farm in the Aus region of southern Namibia (Fig. 5.1*A*) (Vickers-Rich et al., 2013a; Hall et al., *submitted*). Available radiometric and chemostratigraphic data constrain the Kuibis Subgroup to be older than 547.32 ± 0.65 Ma but likely younger than 551.09 ± 1.02 Ma (Grotzinger et al., 1995; Condon et al., 2005; Narbonne et al., 2012; Schmitz, 2012a). The upper Kliphoek Member consists mainly of interbedded sandstones (1–2 m thick) and shales with a few limestone beds. The upper Kliphoek Member was likely deposited in an extensive, sandy, braided fluvial to shallow marine system, partly reworked into vast inter-tidal sand flats along a low gradient coastal plain (Saylor et al., 1995; Elliott et al., 2011; Hall et al., *submitted*). Individual

sandstone beds were likely deposited during sheet flood events which brought sandy sediments over mud-dominated inter-tidal to sub-tidal sediments. *P. simplex* fossils are found in these sandstone beds, particularly in the lower part of the upper Kliphoek Member (Hall et al., *submitted*). The upper Kliphoek Member is directly overlain by bedded limestones of the Mooifontein Member, suggesting a major marine transgression in the area (Gresse and Germs, 1993).

5.4 Materials and Methods

The analyzed hand sample (V-8-2009; Figs. 5.2,7) contains multiple *Pteridinium simplex* specimens. The fossils are preserved as casts or molds in massive quartzite, with their vanes probably replicated by pyrite but represented by stylolitic surfaces, void spaces, or secondary calcite formed during diagenesis or weathering (Meyer et al., *submitted*). The segments in each vane are seen as parallel lines or ridges emanating perpendicularly from the seam. These ridges may grade into a smooth surface farther away from the seam (Jenkins, 1992; Crimes and Fedonkin, 1996; Grazhdankin and Seilacher, 2002; Elliott et al., 2011). The hand sample was cut into three slabs perpendicular to the main axis/seam of the largest and most prominent *P. simplex* specimen. The slabs are labeled 1–3 and cut lines are marked by *i–ii* in Fig. 2*A*. Sl5.ab 1 was used for petrographic analyses (Meyer et al., *submitted*) while slabs 2 and 3 were used in this study. Slabs 2 and 3 were cut so that they can fit in the microCT scanner.

The two slabs were scanned separately using the ultra-high-resolution subsystem of the ACTIS scanner at the University of Texas High-Resolution X-ray CT Facility. A FeinFocus microfocal X-ray source operating at 200 kV and 0.24mA with no X-ray

prefilter was employed. An empty container wedge was used. Slice thickness corresponded to one line in a CCD image intensifier imaging system, with a source-to-object distance of 275 mm for slab 2 and 330 mm for slab 3, resulting in 0.096 mm and 0.115 mm interslice spacing, respectively. For each 1024x1024 pixel slice, 1400 views were acquired with three samples per view over 360 degrees of rotation. The field of reconstruction was 91 mm for slab 2 and 107 mm for slab 3, resulting in 0.089 mm and 0.104 mm in-plane resolution, respectively.

The scan data were processed to reduce ring and beam-hardening artifacts, and 16bit TIFF image stacks were reconstructed (1312 and 1083 slices for slabs 2 and 3, respectively). While useful on their own, these image stacks did not allow for easy 3D visualization of the fossils within the slabs. Thus, these data were further processed using open-source image processing, segmentation, and volume rendering tools to create 3D reconstructions of the features of interest. Because of the large size of the original data volumes (2.6 and 2.2 Gb for slabs 2 and 3, respectively), the image resolution and bit depth were reduced by half using ImageJ(Schneider et al., 2012) to 512 × 512 and 8bit depth to facilitate rendering. The resulting stack was saved as a RAW file and then converted to NRRD format using the command line utility UNU (2013) for initial rendering and import into segmentation software

The volumes were then segmented into individuals and vanes using a combination of manual mask painting and semi-automated tools available in Seg3D (CIBC, 2013), an image processing and segmentation application built on ITK (Yoo et al., 2002). The segment masks of interest (individual specimens, vanes) were then exported as image stacks, resized using ImageJ to a useable (i.e., interactively renderable or an amount of

voxels that will not strain the computer's CPU and memory capacities) 258 × 258 × 258 voxels, and converted to NRRD using UNU. Finally, the NRRD segments were composited and rendered using H3D (Sensegraphics, 2013), and X3D browser with strong support for NRRD and the volume rendering styles provided by the X3D 3.3 standard (Brutzman and Daly, 2007; Consortium, 2012). Each segment was represented as an isosurface and uniquely false-colored for easy visualization. Using H3D, the two slabs were then scaled and "stitched" to restore their original pre-cut configuration. The original microCT data, reslicings, and derivative animations are available at www.digimorph.org/specimens/Pteridinium_simplex.

5.5 Results

A comparison of light photographs and corresponding microCT renderings, shown at two different perspectives is presented in Fig. 5.2. MicroCT reveals five *Pteridinium simplex* specimens embedded in the scanned blocks (labeled 1–5 in Fig. 5.3). These specimens do not have a consistent orientation; for example, specimens 1 and 3 are oriented at 90° from each other. Four of the five specimens are partially exposed, with the exposed vanes marked by colored arrows matching the color of segmented specimens in Fig. 5.2. Three specimens (1, 2 and 4) have some part of all three vanes present while the other two specimens have at least one preserved vane (Figs. 5.2–4).

Specimen 1 is bent tightly and twisted slightly, but its three vanes are easily identifiable (colored individually in Fig. 5.4). It can be seen in Fig. 5.4*D* that the blue medial vane is incompletely preserved where the specimen is bent. As the fossil is bent over itself, the outer lateral vane is stretched (yellow vane in Fig. 4) and the inner lateral

vane is compressed (green vane in Fig. 5.4). The green lateral vane is also ruptured or torn along segment boundaries, although the proximal part of the vane (the part closer to the central seam) is still intact (Fig. 5.4*A*). The two torn pieces are oriented at ~90º to each other; because of this, they could be easily mistaken for two different vanes, with the dangling piece in Fig. 5.4*B* and 5.4*D* misidentified as a medial vane, particularly when the real medial vane (blue color in Fig. 5.4*C* and 5.4*D*) is not well preserved. Thus, taphonomic alteration could lead to false interpretation of vane identity change.

Specimen 3 abuts against specimen 1, with their exposed vanes oriented at a right angle (Figs. 5.2*A*–*B*, 3*A*. 5*A*), giving an impression of possible penetrative growth. However, rock material at the exposed contact between the two specimens has been removed by weathering, making it impossible to determine the exact nature of the contact based on visual examination of the hand sample. MicroCT allows a closer look at the nature of the contact inside the hand sample, and the slice images shows that (1) the vanes of these two specimens do not crosscut each other; and (2) a vane of specimen 3 is bent slightly at the distal edge when it comes in close contact with one of the lateral vane of specimen 1. The latter relationship is best seen in unexposed vanes where the effect of weathering is minimal (e.g., compare the exposed and unexposed parts of the same vane marked by green arrows in Fig. 5.5*B* and 5.5*C*, respectively). Thus, we have found no evidence for penetrative growth, even though the jumbled specimens seem to give the impression of a penetrative relationship.

The other three specimens also interact with Specimen 1. One lateral vane of specimen 2 is also in contact with the distal ends of the two lateral vanes of Specimen 1 (Figs. 5.2*D*, 3*B*). Again, there is no evidence for penetrative growth. Specimen 4 can be

clearly seen as a curved space on the surface of the hand sample (Fig. 5.7*B*). However, only a small part of this specimen is preserved and one of its vanes is in contact with the seam of Specimen 1 (Fig. 5.3*B*). Specimen 5 sits against one of the lateral vanes of specimen 1 (Fig. 5.2*D*, 3*B*), but this specimen has the least preservational fidelity and is difficult to reconstruct. Despite the interactions among the five specimens in the analyzed sample, there is no evidence for penetrative growth.

5.6 Taphonomic and Ecological Interpretations

Our microCT analysis confirms the basic morphological architecture of *Pteridinium simplex*, with three vanes attached to a single central seam. The nature of vane preservation as void space or secondary calcite, however, does not allow us to resolve whether each vane is composed of a single row or two overlapping rows of segments (Jenkins, 1992). Nonetheless, the microCT data do reveal several important aspects of *P. simplex* morphology, taphonomy, and paleoecology.

First, the folding, bending, and twisting of *P. simplex* specimens, as well as the stretching, warping, and breakage of *P. simplex* vanes, are interpreted as taphonomic in origin. Such taphonomic alteration is expected given the sedimentological inference that these specimens were entrained and transported in mass flow deposits (Elliott et al., 2011). Entrainment in high-density mass flow deposits also better explains the lack of preferred orientation among tightly packed specimens. Indeed, different parts of a single specimen can assume different orientation; for example, the bending and twisting of specimen 1 result in different orientations of the two ends of this fossil (Figs. 5.4*B*, *D*, 6).

Second, although *P. simplex* vanes are very stretchable, they can be torn, apparently along segment boundaries which may represent mechanical weakness. That the distal part of the vane is torn whereas the proximal part is intact suggests that the former may have been mechanically weaker than the latter. This inference is consistent with previous interpretations that the seam of *P. simplex* seems to be the most rigid part of the organism, with the vanes and segments quickly losing definition farther away from the seam and grading into a smooth surface (Jenkins, 1992; Grazhdankin and Seilacher, 2002; Elliott et al., 2011). The taphonomic re-orientation of broken vanes would also make it difficult to determine vane identity, particularly when the medial vane is poorly preserved (as commonly is the case) and when 3D morphological reconstructions are not available and thus the determination of vane identity has to be based on vane orientation.

Third, detailed microCT imaging of the interrelationship between tightly packed *P. simplex* specimens with sharply abutting vanes shows no evidence for penetrative growth; instead, the distal edges of vanes are bent when compressed against other vanes. Previous interpretation of penetrative growth in *P. simplex* was based on hand sample observation of specimens with vanes abruptly abutting against each other (Grazhdankin and Seilacher, 2002). Such a relationship can be alternatively interpreted as taphonomically broken vanes jammed against other specimens. A positive identification of penetrative growth requires microCT data to confirm that vanes do crosscut each other rather than just abut against each other.

Thus, some of the evidence previously used to infer a fully endobenthic lifestyle of *P. simplex*—convoluted specimens with penetrative growth and vane identity change (Grazhdankin and Seilacher, 2002)—needs to be reconsidered in light of the new data

presented here. Nonetheless, we do think it is possible that *P. simplex* could have been semi-endobenthic (Fig. 5.1*B*), with its central seam buried in the sediments but the distal part of the vanes remaining free in the water column (Grazhdankin and Seilacher, 2002; Elliott et al., 2011; Meyer et al., *submitted*). This ecological interpretation can also account for *Pteridinium* specimens that are preserved more or less two-dimensionally on the bedding surface (Narbonne et al., 1997).

5.7 Phylogenic Constraints

Previous authors have pointed out that the integument of *Pteridinium. simplex* (and other Ediacara fossils) needs to be rigid enough to survive transport, but also pliable enough to account for bent and twisted specimens (Dzik, 1999; Gehling, 1999; Dzik, 2003; Fedonkin et al., 2007a). Collagen and cellulose have been the most commonly hypothesized biomaterials that may have made up the *P. simplex* integument (Seilacher, 1992; Buss and Seilacher, 1994; Dzik, 1999; Elliott et al., 2011), with others also suggesting agglutinate sediments similar to extant xenophyophoran tests (Seilacher et al., 2003) or fungal hyphae similar to mycobionts in modern lichens (Retallack, 1994; 2007) as possible constructional biomaterials. However, the strongly elastic behavior of *P. simplex* vanes rules out the agglutinate nature of its integument and thus a phylogenetic affinity with xenophyophores.

The strongly elastic behavior of *P. simplex* vanes is indicative of collagen in the integument of *P. simplex*. Collagen is most commonly found in integuments, muscles, and connective tissues of animals (Vogel, 2003), and it is also present in the mesoglea of diploblastic animals such as cnidarians and ctenophores (Hernandez-Nicaise and

Amsellem, 1982; Tucker et al., 2011). Mesoglea is a tough viscoelastic collagenous material (Alexander, 1964; 1971; Vogel, 2003) that displays both viscous and elastic characteristics and can be elastically deformed when deformation occurs slowly, but would be broken or torn when stress is applied rapidly (Vogel, 2003). Thus, the viscoelastic property of collagenous biomaterial may explain how *P. simplex* integument can be bent, twisted, elastically stretched, and occasionally torn. Indeed, a collagenous mesoglea is also implicitly present in other Ediacara fossils such as *Eoandromeda octobrachiata*, which has been interpreted as a benthic diploblastic grade animal (Zhu et al., 2008) or a pelagic stem-group ctenophore (Tang et al., 2011).

However, the presence of collagen does not preclude the presence of cellulose in *P. simplex*. Cellulose fibers are very flexible, as can be observed in some algal fronds (Koehl, 1999; Martone, 2007; Martone and Denny, 2008) and, while cellulose is present primarily in plants, some animals such as tunicates have both cellulose and collagen in their tissues (Endean, 1961; Vogel, 2003). Indeed, the Ediacara fossils *Ausia* and *Burykhia* have been interpreted as tunicate animals (Fedonkin et al., 2012). Because cellulose fibers are stiffer than collagen, breaks or tears are usually very sharp, potentially explaining the sharp torn edge of *P. simplex* vanes (Fig. 4). Thus, the stiff yet very flexible nature of *P. simplex* vanes suggests the presence of both collagen and cellulose in its integument.

If our biomaterial interpretation is correct, then *P. simplex* would be more closely related to living animals than any other living clade, because collagen is exclusively present in the animal kingdom and cellulose is also present in some living animals. It is true that *P. simplex* does not share its body plan with any other living animal clades, but

it does not preclude it to be placed as a stem-group animal. Because the animal kingdom and its living sister group—the choanoflagellates—are separated by significant morphological gaps, it is expected that stem-group animals share one or a few features (collagen in the case of *P. simplex*) collectively defining the living animal clade, and it is also expected that these extinct stem-group animals may have evolved their own autapomorphies (three-vaned body architecture in the case of *P. simplex*) that make them drastically different from living animals.

5.8 Conclusions

MicroCT offers an effective approach to study *Pteridinium simplex* specimens preserved in 3D within mass flow deposits. Our investigation confirms the basic morphology of *P. simplex*: three vanes attached at the seam. The vanes can be bent, folded, twisted, stretched, and torn, through taphonomic processes. Such taphonomic alterations complicate morphological reconstruction of *P. simplex*, and can potentially lead to false interpretation of vane identity change and penetrative growth, particularly when observation is limited to the external surface of fossiliferous blocks. Our microCT analysis reveals no evidence for vane identity change or penetrative growth. Thus, the important basis for an entirely endobenthic *P. simplex* should be treated with caution, and we favor the traditional ecological interpretation of *P. simplex* as a semi-endobenthic or epibenthic organism because this life style also accounts for specimens preserved two dimensionally on bedding surfaces. The taphonomic deformation of *P. simplex* indicates that it had an elastic integument, which is inconsistent with a phylogenetic affinity with xenophyophores. We propose that its integument was made of a collagenous and

cellulose biomaterial. Because collagen synthesis appears to be a synapomorphy of the animal kingdom, *P. simplex* may be phylogenetically related to animals, likely representing a stem-group animal considering its unique body plan.

5.9 Acknowledgments

Financial support for this study was provided by National Science Foundation, NASA Exobiology and Evolutionary Biology Program, Paleontological Society, Society for Sedimentary Geology, Virginia Tech Institute for Critical Technology and Applied Science Nanoscale Characterization and Fabrication Laboratory, Virginia Tech Visionarium, UNESCO's International Geosciences Program Projects 493 and 587, the National Geographic Society, and from both the international and national committees of the International Geoscience Programme (IGCP). We would like to thank the owners of Farm Aar, B. Boehm-Erni and the late B. Boehm, for granting access to fossil site. We would like to thank Charles Farley for technical assistance and our reviewers for constructive comments.

5.10 Figure and Figure Captions

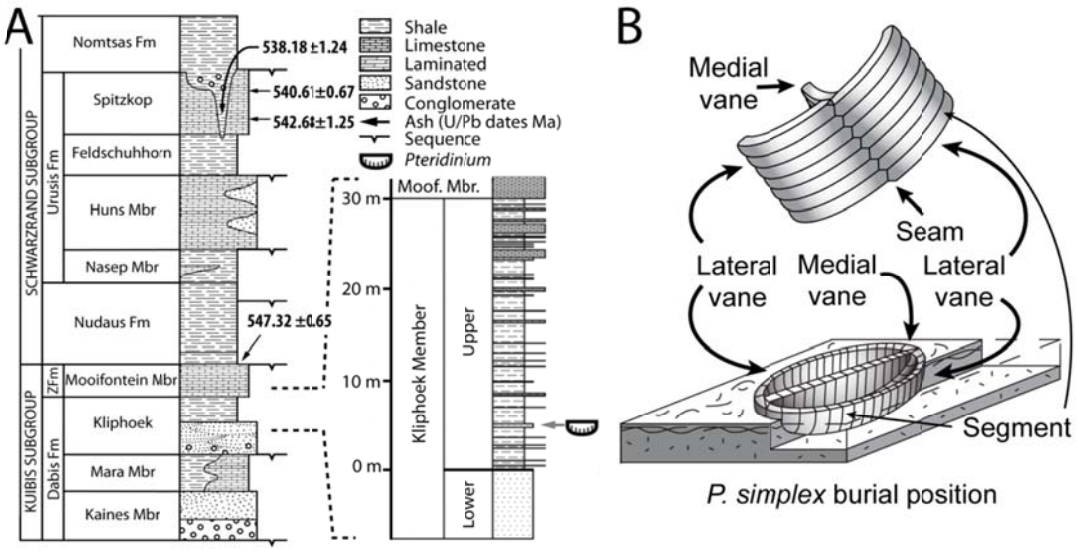

Figure 5.1. Stratigraphic column and construction of *Pteridinium simplex*. (*A*) Stratigraphic column showing the location of the fossil horizon the hand sample in this study was collected from (in the upper Kliphoek Member, Dabis Formation, Kuibis subgroup) and radiometric dates. (*B*) Morphological and ecological reconstruction and descriptive terms of *P. simplex*.

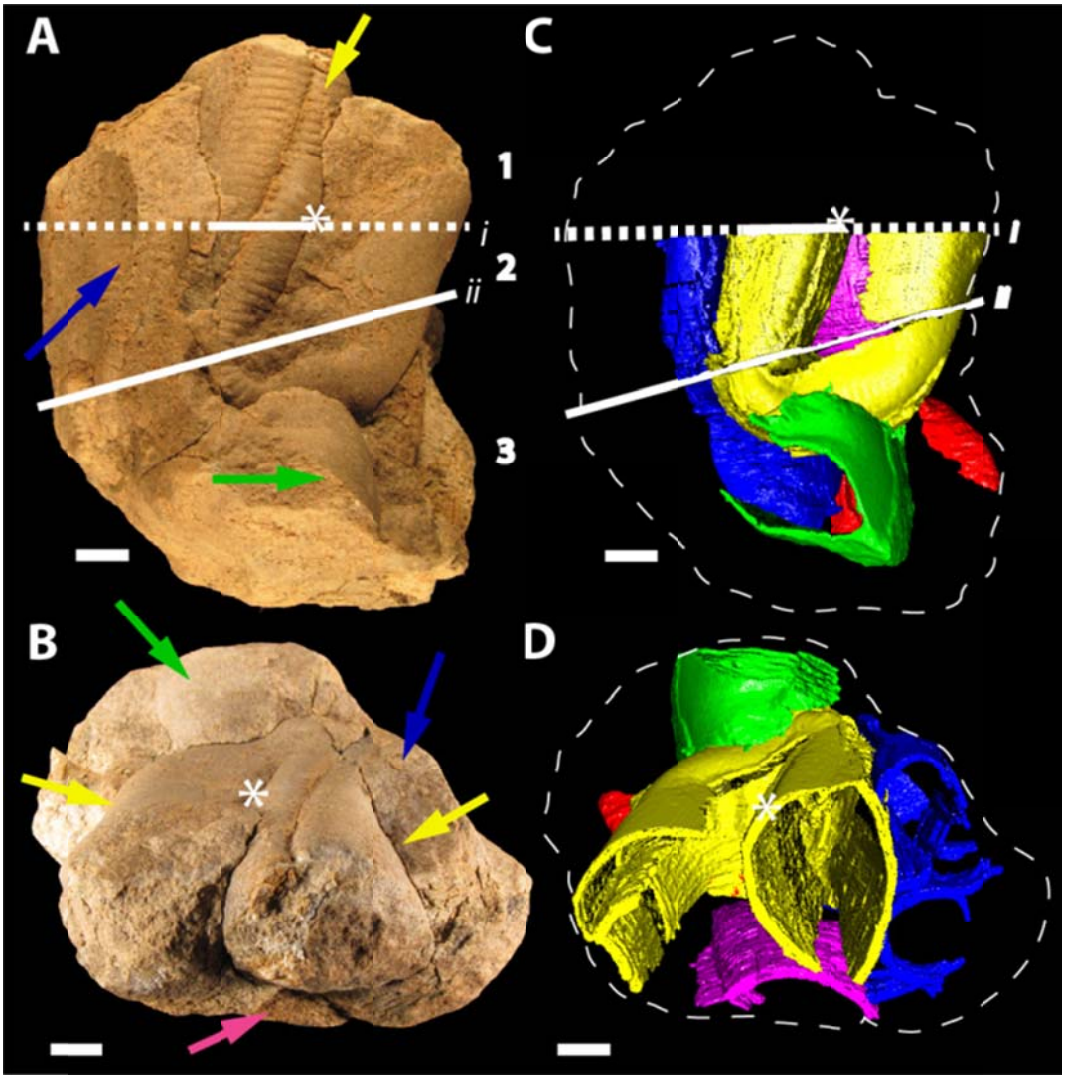

Figure 5.2. Light photography and 3-D reconstruction of *P. simplex* specimens within hand sample block V-8-2009. (*A*–*B*) Light photographs from two different perspectives, with *B* showing a view from the yellow arrow in *A*. (*C*– *D*) MicroCT segmentations of *P. simplex* specimens, oriented at the same perspectives as *A* and *B*, respectively, with dashed lines representing the outline of the hand sample. Colored arrows point to specimens segmented in corresponding colors. Yellow arrow points to main specimen (specimen 1) in this study. Numbers 1–3 denote the three slabs resulting from cuts represented by lines *i* and *ii*, slabs 2 and 3 were microCT scanned. Asterisks mark the same location and can be used for orientation. Scale bar = 1 cm.

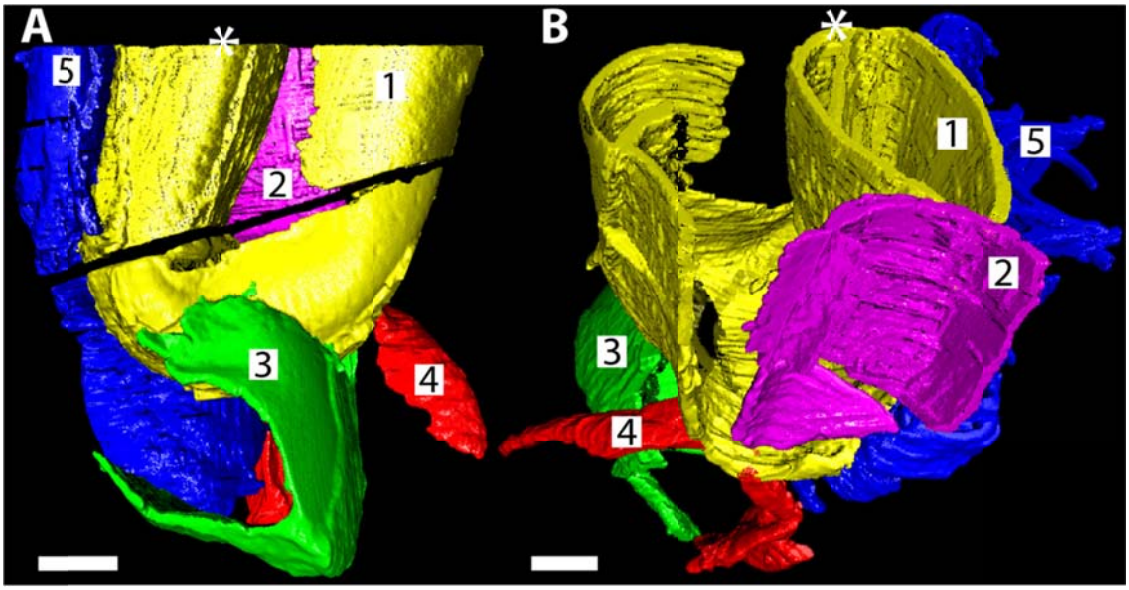

Figure 5.3. Two different views of the five segmented specimens of *Pteridinium simplex*. Specimens are colored and numbered. Asterisks mark the same location. Scale bar = 1 cm.

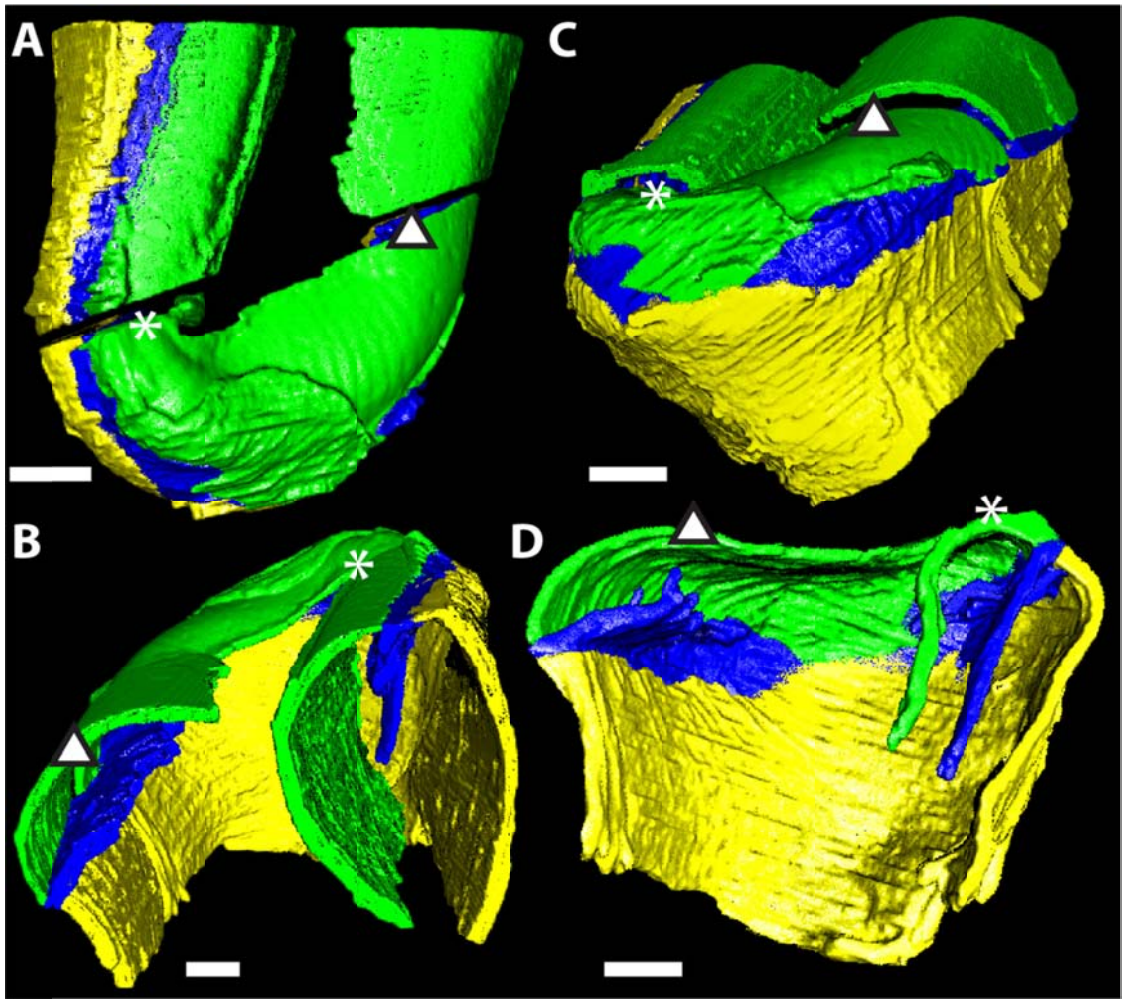

Figure 5.4. Four different views of *Pteridinium simplex* specimen 1. Lateral vanes are yellow and green, and medial vane is blue. Asterisks and triangles mark two landmark locations in all views. Scale bar = 1 cm.

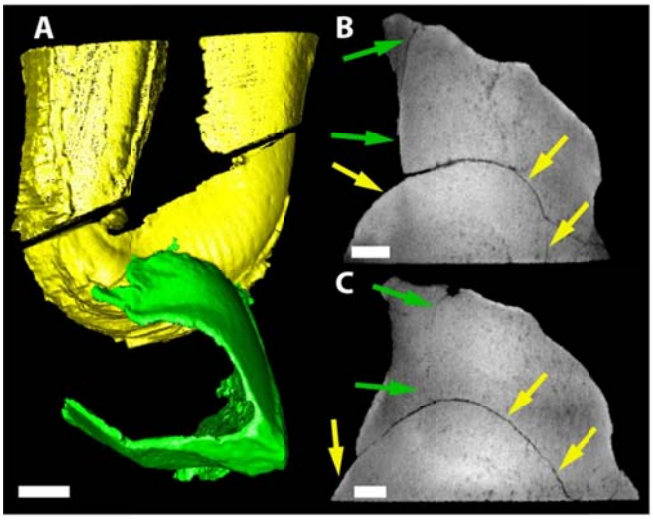

Figure 5.5. Three-dimensional reconstruction and microCT slice images of *Pteridinium simplex* specimens 1 and 3. (*A*) View showing that the vanes of the two specimens abruptly abut against each other. (*B*–*C*) MicroCT slice images, showing the relationship between the two specimens. Colored arrows point to vanes of specimens segmented in corresponding colors. Note that the apparent vane termination of specimen 3 at specimen 1 is due to weathering on exposed surface (green arrows and green dotted line in *B*) and that, when unexposed, the same vane is distally bent where it is compressed against specimen 1 as seen (green arrows and green dotted line in *C*). Scale bar = 1 cm.

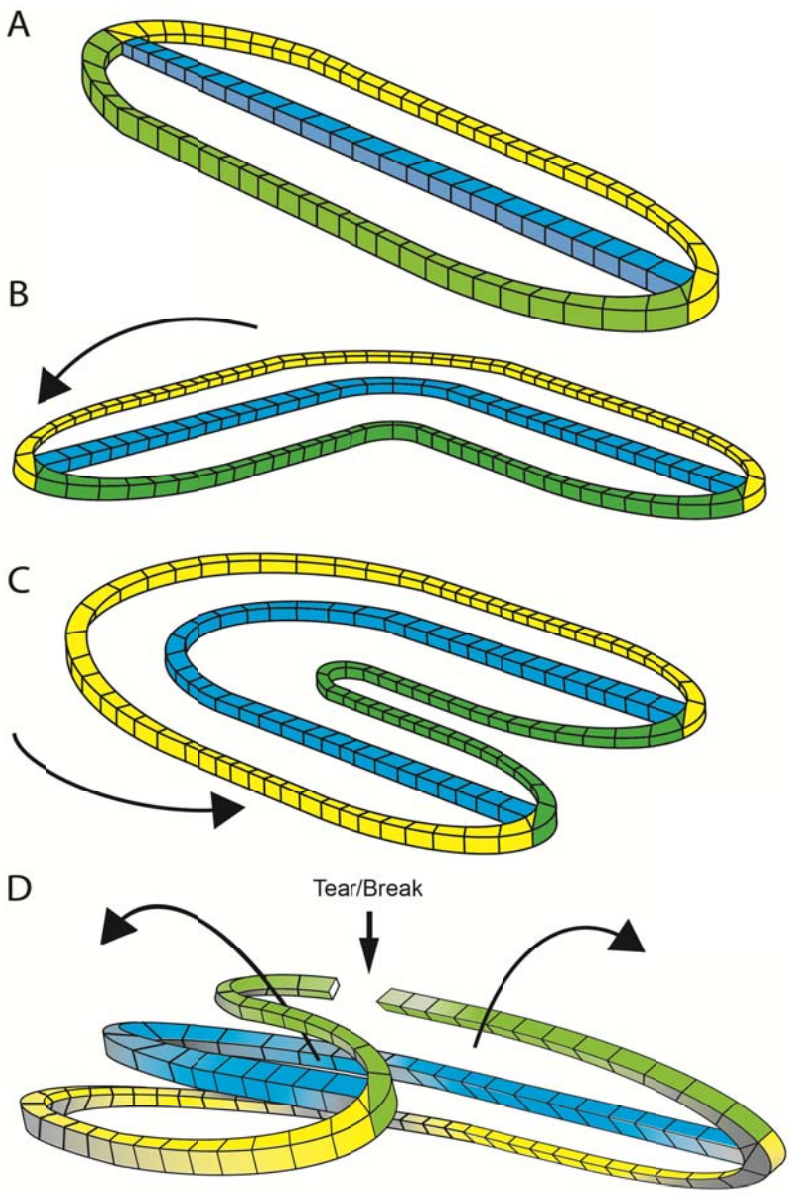

Figure 5.6. Simplified diagram showing bending, twisting, and tearing in Specimen 1 (vane colors correspond to those in Figure 4). A, Pre-deformation morphology. *B–C*, Bending. D, Twisting and tearing along segment boundaries.

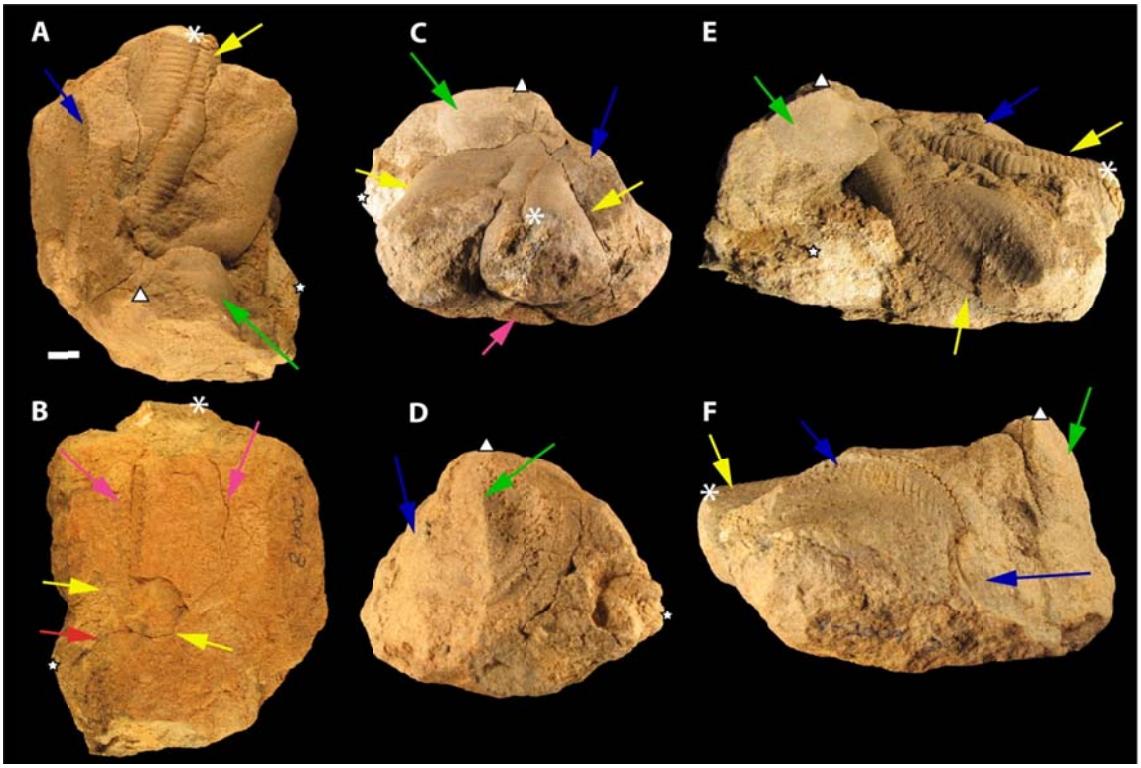

Figure 5.7. Light photographs of hand sample V-8-2009, shown in different views. Colored arrows point to correspondingly colored *P. simplex* specimens in Fig. 5.3. Asterisks, triangles, and stars mark landmark locations in all views.

5.11 References

ALEXANDER, R.M., 1964, Visco-elastic properties of the mesogloea of jellyfish: Journal of Experimental Biology, v. 41, p. 6.

ALEXANDER, R.M., 1971, Connective tissue mechanics of *Metridium senile*: Journal of Experimental Biology, v. 55, p. 11.

BRUTZMAN, D., and DALY, L., 2007, X3D: Extensible 3D Graphics for Web Authors: Morgan Kaufmann Publishers Inc., San Francisco, CA.

BUSS, L.W., and SEILACHER, A., 1994, The Phylum Vendobionta: A sister group of the Eumetazoa?: Paleobiology, v. 20, p. 1-4.

CAI, Y., SCHIFFBAUER, J.D., HUA, H., and XIAO, S., 2012, Preservational modes in the Ediacaran Gaojiashan Lagerstätte: Pyritization, aluminosilicification, and carbonaceous compression: Palaeogeography Palaeoclimatology Palaeoecology, v. 326-328, p. 109-117, doi: 10.1016/j.palaeo.2012.02.009.

Seg3D: volumetric image segmentation and visualization, 2013,http://www.seg3d.org Checked 2013 2013.

CONDON, D., ZHU, M., BOWRING, S., WANG, W., YANG, A., and JIN, Y., 2005, U-Pb ages from the Neoproterozoic Doushantuo Formation, China: Science, v. 308, p. 95-98.

Extensible 3D (X3D) specifications: ISO/IEC 19775-1 (Abstract Spec), ISO/IEC 19775-2 (SAI), ISO/IEC 19776-1 (XML Encoding), ISO/IEC 19776-2 (utf-8 Encoding, ISO/IEC), 19776-3 (Binary Encoding), 2012,http://www.web3d.org Checked 2013 2013.

CRIMES, T.P., and FEDONKIN, M.A., 1996, Biotic changes in platform communities across the Precambrian-Phanerozoic boundary: Rivista Italiana di Paleontologia e Stratigrafia, v. 102, p. 317-332.

DZIK, J., 1999, Organic membranous skeleton of the Precambrian metazoans from Namibia: Geology, v. 27, p. 519-522.

DZIK, J., 2003, Anatomical information content in the Ediacaran fossils and their possible zoological affinities: Integrative and Comparative Biology, v. 43, p. 114-126.

ELLIOTT, D.A., VICKERS-RICH, P., TRUSLER, P., and HALL, M., 2011, New evidence on the taphonomic context of the Ediacaran *Pteridinium*: Acta Palaeontologica Polonica, v. 56, p. 641-650.

ENDEAN, R., 1961, The Test of the Ascidian, *Phallusia mammillata*: Quarterly Journal of Microscopical Science, v. 102, p. 107-117.

FEDONKIN, M.A., GEHLING, J.G., GREY, K., NARBONNE, G.M., and VICKERS-RICH, P., 2007, The Rise of Animals: Evolution and Diversification of the Kingdom Animalia: Johns Hopkins University Press, Baltimore, 326 p.

FEDONKIN, M.A., VICKERS-RICH, P., SWALLA, B.J., TRUSLER, P., and HALL, M., 2012, A New Metazoan from the Vendian of the White Sea, Russia, with Possible Affinities to the Ascidians: Paleontological Journal, v. 46, p. 1-11.

GEHLING, J.G., 1999, Microbial mats in terminal Proterozoic siliciclastics: Ediacaran death masks: Palaios, v. 14, p. 40-57.

GLAESSNER, M.F., 1984, The Dawn of Animal Life: A Biohistorical Study: Cambridge Univ. Press, Cambridge, UK, 244 p.

GLAESSNER, M.F., and DAILY, B., 1959, The geology and Late Precambrian fauna of the Ediacaran fossil reserve: Record of South Australia Museum, v. 13, p. 369-401.

GRAZHDANKIN, D., and SEILACHER, A., 2002, Underground Vendobionta from Namibia: Palaeontology, v. 45, p. 57-78.
GRESSE, P.G., and GERMS, G.J.B., 1993, The Nama foreland basin: sedimentation, major unconformity bounded sequences and multisided active margin advance: Precambrian Research, v. 63, p. 247-272.
GROTZINGER, J.P., BOWRING, S.A., SAYLOR, B.Z., and KAUFMAN, A.J., 1995, Biostratigraphic and geochronologic constraints on early animal evolution: Science, v. 270, p. 598-604.
GÜRICH, G., 1930, Die bislang ältesten Spuren von Organismen in Südafrika: International Geological Congress. South Africa, 1929 (XV), v. 2, p. 670-680.
HALL, M., KAUFMAN, A.J., VICKERS-RICH, P., GUY, N., IVANSTOV, A.Y., TRUSLER, P., LINNEMANN, U., HOFMANN, M., ELLIOTT, D.A., CUI, H., FEDONKIN, M.A., HOFFMAN, K., WILSON, S.A., SCHNEIDER, G., and SMITH, J., *submitted*, Changing environments and their impact on metazoan evolution and preservation during the terminal Proterozoic in african Gondwana: Precambrian Research, v. xxx, p. xxx.
HERNANDEZ-NICAISE, M.L., and AMSELLEM, J., 1982, Ultrastructure of the giant smooth muscle fiber of the ctenophore *Beroe ovata*: Journal of Ultrastructure Research, v. 72, p. 151-168.
JENKINS, R.J.F., 1992, Functional and ecological aspects of Ediacaran assemblages, *in* Lipps, J.H., and Signor, P.W., eds., Origin and Early Evolution of Metazoa: Plenum Press, New York, p. 131-176.
KOEHL, M.A.R., 1999, Ecological biomechanics of benthic organisms: Life history, echanical design and temporal patterns of mechanical stress: Journal of Experimental Biology, v. 202, p. 7.
LAFLAMME, M., DARROCH, S.A.F., TWEEDT, S.M., PETERSON, K.J., and ERWIN, D., 2013, The end of the Ediacara biota: Extinction, biotic replacement, or Cheshire Cat?: Gondwana Research, v. 23, p. 558-573.
LAFLAMME, M., SCHIFFBAUER, J.D., NARBONNE, G.M., and BRIGGS, D.G., 2011, Microbial biofilms and the preservation of the Ediacara biota: Lethaia, v. 44, p. 203-213.
MARTONE, P.T., 2007, Kelp versus Coralline: Cellular basis for mechanical strength in the wave-swept seaweed calliarthron (Corallinaceae, Rhodophyta): Journal of Phycology, v. 43, p. 9.
MARTONE, P.T., and DENNY, M.W., 2008, To bend a coralline: effect of joint morphology on flexibility and stress amplification in an articulated calcified seaweed: The Journal of Experimental Biology, v. 211, p. 11.
MEYER, M., ELLIOTT, D.A., SCHIFFBAUER, J.D., VICKERS-RICH, P., XIAO, S., HOFFMANN, K.H., HALL, M., and SCHIENDER, G., *submitted*, Taphonomy of the Ediacaran fossil Pteridinium simplex preserved three-dimensionally in mass flow deposits in the Nama group of Namibia: Journal of Paleontology, v. xxx, p. xxx-xxx.
NARBONNE, G.M., 2005, The Ediacara Biota: Neoproterozoic origin of animals and their ecosystems: Annual Review of Earth and Planetary Sciences, v. 33, p. 421-442.
NARBONNE, G.M., SAYLOR, B.Z., and GROTZINGER, J.P., 1997, The youngest Ediacaran fossils from southern Africa: Journal of Paleontology, v. 71, p. 953-967.

NARBONNE, G.M., XIAO, S., and SHIELDS, G.A., 2012, The Ediacaran Period, *in* Gradstein, F.M., Ogg, J.G., Schmitz, M.D., and Ogg, G., eds., Geological Time Scale 2012: Elsevier, Oxford, p. 413-435.

PFLUG, H.D., 1994, Role of size increase in Precambrian organismic evolution: Neues Jahrbuch für Geologie und Palaeontologie Abhandlungen, v. 193, p. 245-286.

RETALLACK, G.J., 1994, Were the Ediacaran fossils lichens?: Paleobiology, v. 20, p. 523-544.

RETALLACK, G.J., 2007, Growth, decay and burial compaction of *Dickinsonia*, an iconic Ediacaran fossil: Alcheringa, v. 31, p. 215-240.

SAYLOR, B.Z., KAUFMAN, A.J., GROTZINGER, J.P., and URBAN, F., 1995, Sequence stratigraphy and sedimentology of the Neoproterozoic Kuibis and Schwarzrand Subgroups (Nama Group), southwestern Namibia: Precambrian Research, v. 73, p. 153-171.

SCHIFFBAUER, J.D., and LAFLAMME, M., 2012, Lagerstätten through time: a collection of exceptional preservational pathways from the terminal Neoproterozoic through today: Palaios, v. 27, p. 3.

SCHMITZ, M.D., 2012, Appendix 2-Radiometric ages used in GTS2012, *in* Gradstein, F.M., Ogg, J.G., Schmitz, M.D., and Ogg, G., eds., The Geologic Time Scale 2012: Elsevier, Boston, p. 1045-1082.

SCHNEIDER, C.A., RASBAND, W.S., and ELICEIRI, K.W., 2012, NIH Image to ImageJ: 25 years of image analysis: Nature Methods, v. 9, p. 4.

SEILACHER, A., 1992, Vendobionta and Psammocorallia: lost constructions of Precambrian evolution: Journal of the Geological Society of London, v. 149, p. 607-613.

SEILACHER, A., GRAZHDANKIN, D., and LEGOUTA, A., 2003, Ediacaran biota: The dawn of animal life in the shadow of giant protists: Paleontological Research, v. 7, p. 43-54.

Open source haptics - H3D.org, 2013,h3dapi.org.

TANG, F., BENGTSON, S., WANG, Y., WANG, X., and YIN, C., 2011, *Eoandromeda* and the origin of Ctenophora: Evolution and Development, v. 13, p. 6.

TUCKER, R.P., SHIBATA, B., and BLANKENSHIP, T.N., 2011, Ultrastructure of the mesoglea of the sea anemone *Nematostella vectensis* (Edwardsiidae): Invertebrate Biology, v. 130, p. 11-24.

Teem: tools to process and visualize scientific data and images, 2013, updated 2013,teem.sourceforge.net Checked 2013 2013.

VICKERS-RICH, P., IVANOV, A.V., TRUSLER, P., NARBONNE, G.M., HALL, M., WILSON, S.I., GREENTREE, C., FEDONKIN, M.A., ELLIOTT, D.A., HOFFMANN, K.H., and SCHNEIDER, G.I.C., 2013, Reconstructing Rangea: New discoveries from the Ediacaran of southern Namibia: Journal of Paleontology, v. 87, p. 15, doi: http://dx.doi.org/10.1666/12-074R.1.

VOGEL, S., 2003, Comparative Biomechanics: lifes physical world: Princetion University Press, New Jersey, USA, 580 p.

XIAO, S., and LAFLAMME, M., 2009, On the eve of animal radiation: Phylogeny, ecology and evolution of the Ediacara biota: Trends in Ecology & Evolution, v. 24, p. 31-40.

YOO, T.S., ACKERMAN, M.J., LORENSEN, W.E., SCHROEDER, W., CHALANA, V., AYLWARD, S., METAXAS, D., and WHITAKER., R., 2002, Engineering and Algorithm Design for an Image Processing API: A Technical Report on ITK - The Insight Toolkit, in Westwood, J. ed., Proceedings of Medicine Meets Virtual Reality: IOS Press, Amsterdam, p. 586-592.

ZHU, M., GEHLING, J.G., XIAO, S., ZHAO, Y.-L., and DROSER, M., 2008, Eight-armed Ediacara fossil preserved in contrasting taphonomic windows from China and Australia: Geology, v. 36, p. 867-870.

Chapter 6

Midnight in the garden of Ediacara

MIKE MEYER

[1]*Department of Geosciences, Virginia Polytechnic Institute and State University, Blacksburg, VA 24061, USA*

6.1 Conclusions

Ediacaran fossils include many organisms that are unlike anything found in the Phanerozoic, some with no comparable modern analog, and are phylogenetically problematic. The biosphere during this time was undergoing a major transition with large perturbations to the atmosphere, ocean systems, and a fundamental change in the relationship that life had with the sediment (the Agronomic revolution). Thus, Ediacaran paleontological exploration requires scientists to take multidisciplinary approaches, by analyzing and integrating sedimentological, geochemical, paleobiological, and geobiological data. All of these factors were examined through taphonomic investigations and this can be seen in the analytical path through my chapters. In chapter two I examined the preservation of trace fossils in the late Ediacaran. In chapter three I analyzed the taphonomy of an exceptionally preserved Ediacaran fossil to solve its affinity, tubular trace or tubular soft-bodied fossil. In chapter four, understanding the nature of exceptional preservation, I investigated the taphonomy of an Ediacara fossil in coarse grained sediments. In chapter five, I combined the findings of the previous chapters and applied that knowledge to analyze the *in situ* three dimensional morphology of an Ediacara fossil. To summarize in greater detail:

In chapter two I described a new trace fossil, *Lamonte trevallis*, which, in addition to other recent finds (Chen et al, 2013), adds to the established data and suggests that the benthic community of the late Ediacaran in South China was more complex than previously thought. The emerging picture of this time period is one that has body fossils, both Ediacara-grade and tubular (Sun, 1986; Liu et al., 2009; Shen et al., 2009), in association with simple surface trace makers (Weber et al., 2007) and larger, system

building burrowers (*Lamonte trevallis*), and active bilaterian bioturbators. *Lamonte trevallis* tunnels form complex systems that are associated with microbial laminae. The multi-nodal tunnel networks suggest that the main purpose of the *Lamonte trevallis* burrows was to exploit nutrient and oxygen resources while the complexity of *Lamonte trevallis* burrows indicate that trace makers of this time where becoming more behaviorally complex and better able to utilize the resources around them, opening the doors to the Agronomic revolution.

In chapter three I conducted a taphonomic analysis of *Shaanxilithes ningqiangensis* and related discoidal structures which were associated with clay minerals (and rarely with pyrite). That these fossil were found in a silty, calcareous, and phosphate-rich matrix suggests that they share a style of preservation with some similarities to Fermeuse-type preservation (Laflamme et al., 2011b) and Burgess Shale-type preservation (Butterfield, 1995; Orr et al., 1998; Orr et al., 2002; Zhu et al., 2005). It is unlikely that the clay association was formed *de novo* during metamorphism, rather, clay precursors likely existed in life or during authigenesis. Abruptly bent *S. ningqiangensis* ribbons, overlapping but not cross-cutting ribbons, and a probable relationship with disarticulated discoidal, lensoidal, or meniscate modules suggest that *Shaanxilithes ningqiangensis* likely represents an enigmatic body fossil constructed of serially arranged units.

In chapter four I investigated the taphonomic style of *Pteridinium simplex*. It is three-dimensionally preserved *within* mass flow deposits and represents a dramatic departure from the classic 'death mask' preservation, which only occurs along/on bedding surfaces. While pyrite is not as important as in death mask preservation, there is

evidence for minor pyrite in association with *P. simplex* vanes, indicating bacterial sulfate reduction and authigenic pyrite precipitation may have played a constructive role in fossil preservation. However it is unlikely that thick microbial mats developed on *P. simplex* vanes preserved *within* mass flow sediments. Limited precipitation of authigenic pyrite and subsequent destruction by chemical weathering may explain the dearth of pyrite in association with *P. simplex* vanes. There are also minor clay minerals in association with *P. simplex* vanes, particularly unexposed medial vanes; however, the origin of such clays is uncertain, and we tentatively interpret them as weathering products.

Finally, in chapter five, using microCT I further confirmed previous findings on the basic morphology of *P. simplex*: three vanes consisting of numerous segments attached at the (singular) central seam. When seen *in situ*, *P. simplex* specimens are observed to be stiffer near the seam and more elastic in the vanes (they are able to bend quite sharply), yet which can tear sharply along segments. There is no evidence for vanes switching 'identities' or for *P. simplex* specimens to grow out of, terminate in, or cut through each other. Much of the confusion around *P. simplex* morphology is due to the combination of its modular construction and three-dimensional moldic preservation. Further use of *in situ* three-dimensional imagery is likely the only way to decipher *P. simplex* morphology as weathered specimens are already missing a large amount of important morphological information. Furthermore, the biomechanical properties of the *P. simplex* organism are inferred from the microCT data, which suggests that *P. simplex* was a diploblastic organism with a mesoglea. A viscoelastic mesoglea fulfills the tough-yet-elastic characteristics that would be required to see the bending, twisting, and bowing exhibited by *P. simplex* fossils. A diploblastic body plan may have been shared by other

modular Vendobionts and could explain other instances of fossils with tough-yet-elastic properties in the Ediacaran Period.

New methodologies are allowing researchers to delve further into established, or to completely new, areas of geobiology; finding data that were unresolvable before. Each of the projects presented in the previous chapters pairs new technologic methodologies (SEM, BSE-Z, EDS, Raman, microCT) with traditional paleontological/petrologic investigations (field work, hand sample, and petrographic thin-section analysis). The result of this union of Old and New are findings that expand our understanding of these earliest multicellular organisms, their modes of life, and their biological affinities.

6.2 References

BUTTERFIELD, N.J., 1995, Secular distribution of Burgess Shale-type preservation: Lethaia, v. 28, p. 1-13.

LAFLAMME, M., SCHIFFBAUER, J.D., NARBONNE, G.M., and BRIGGS, D.G., 2011, Microbial biofilms and the preservation of the Ediacara biota: Lethaia, v. 44, p. 203-213.

LIU, P., XIAO, S., YIN, C., TANG, F., and GAO, L., 2009, Silicified tubular microfossils from the upper Doushantuo Formation (Ediacaran) in the Yangtze Gorges area, South China: Journal of Paleontology, v. 83, p. 630-633.

ORR, P., KEARNS, S.L., and BRIGGS, D.E.G., 2002, Backscattered electron imaging of fossils exceptionally-preserved as organic compressions: Palaios, v. 17, p. 110-117.

ORR, P.J., BRIGGS, D.E.G., and KEARNS, S.L., 1998, Cambrian Burgess Shale animals replicated in clay minerals: Science, v. 281, p. 1173-1175.

SHEN, B., XIAO, S., ZHOU, C., and YUAN, X., 2009, *Yangtziramulus zhangi* new genus and species, a carbonate-hosted macrofossil from the Ediacaran Dengying Formation in the Yangtze Gorges area, South China: Journal of Paleontology, v. 83, p. 575-587.

SUN, W., 1986, Late Precambrian pennatulids (sea pens) from the eastern Yangtze Gorge, China: *Paracharnia* gen. nov.: Precambrian Research, v. 31, p. 361-375.

WEBER, B., STEINER, M., and ZHU, M.Y., 2007, Precambrian Cambrian trace fossils from the Yangtze Platform (South China) and the early evolution of bilaterian lifestyles: Palaeogeography Palaeoclimatology Palaeoecology, v. 254, p. 328-349.

ZHU, M., BABCOCK, L.E., and STEINER, M., 2005, Fossilization modes in the Chengjiang Lagerstätte (Cambrian of China): testing the roles of organic preservation and diagenetic alteration in exceptional preservation: Palaeogeography, Palaeoclimatology, Palaeoecology, v. 220, p. 31-46.